

**CHARACTERIZATION, MODELING AND DESIGN OF ULTRA-THIN
VAPOR CHAMBER HEAT SPREADERS UNDER STEADY-STATE AND
TRANSIENT CONDITIONS**

by

Gaurav Patankar

A Dissertation

Submitted to the Faculty of Purdue University

In Partial Fulfillment of the Requirements for the degree of

Doctor of Philosophy



School of Mechanical Engineering

West Lafayette, Indiana

May 2019

**THE PURDUE UNIVERSITY GRADUATE SCHOOL
STATEMENT OF COMMITTEE APPROVAL**

Dr. Suresh V. Garimella, Co-Chair

Department of Mechanical Engineering

Dr. Justin A. Weibel, Co-Chair

Department of Mechanical Engineering

Dr. Jong Hyun Choi

Department of Mechanical Engineering

Dr. Liang Pan

Department of Mechanical Engineering

Dr. Alejandro H. Strachan

Department of Materials Engineering

Approved by:

Dr. Jay P. Gore

Head of the Graduate Program

To my parents Manik and Sunil Patankar

ACKNOWLEDGMENTS

I would like to thank my academic advisors, Dr. Suresh V. Garimella and Dr. Justin A. Weibel, whose guidance and support has been vital for my academic, professional, and personal development. Their teachings will be with me throughout my life.

I would like to thank my PhD committee members, Dr. Jong Hyun Choi, Dr. Liang Pan, and Dr. Alejandro H. Strachan for their guidance through my PhD research. Their comments and suggestions have helped my research reach its completion.

I would also like to thank my lab mates for their constant feedback toward my research work, especially Dr. Carolina Mira-Hernandez, Todd Kingston, and Aakriti Jain.

Finally, I would like to thank my family and friends, including my parents, my girlfriend Ruchita Mandhre, and my friend Saurabh Misra, for their encouragement and support during my PhD.

This research was made possible due to the financial support of Intel corporation (as a part of the Intel Strategic Research Alliance (ISRA) on platform thermal cooling solutions) and the members of the Cooling Technology Research Center, a National Science Foundation Industry/University Cooperative Research Center at Purdue University.

TABLE OF CONTENTS

LIST OF TABLES	9
LIST OF FIGURES	10
ABSTRACT	15
1. INTRODUCTION	19
1.1 Background	19
1.2 Objectives and Major Contributions	22
1.3 Organization of the Document	25
2. LITERATURE REVIEW	27
2.1 Experimental Performance Characterization of Vapor Chambers	27
2.2 Design of Vapor Chambers	27
2.3 Vapor Chambers Transport Models	28
2.4 Transient Analysis of Vapor Chambers	29
3. THERMAL PERFORMANCE CHARACTERIZATION OF ULTRA-THIN VAPOR CHAMBERS COOLED BY NATURAL CONVECTION	30
3.1 Experimental Facility	30
3.1.1 Test Section Design and Instrumentation	31
3.1.2 Test Procedure	32
3.2 Calibration of the Test-Section Heat Loss	33
3.3 Results and Performance Metrics	36
3.3.1 Device Thermal Resistance.	36
3.3.2 Surface Temperature Distribution.	37
3.4 Conclusions	38
4. PATTERNING THE CONDENSER-SIDE WICK IN ULTRA-THIN VAPOR CHAMBER HEAT SPREADERS TO IMPROVE SKIN TEMPERATURE UNIFORMITY OF MOBILE DEVICES	51
4.1 Modeling Approach	51
4.1.1 Numerical Vapor Chamber Transport Model	51
4.1.2 Steady-State-Seeking Solution Algorithm	53
4.2 Design Objective	56

4.3	Results and Discussion	56
4.3.1	Baseline Wick Domain Design.....	57
4.3.2	Grooved Condenser Wick Domain Design	59
4.3.3	Biporous Condenser-Side Wick Domain Design with Radially Discretized Grooves..	
	60
4.4	Conclusions.....	62
5.	WORKING-FLUID SELECTION FOR MINIMIZED THERMAL RESISTANCE IN ULTRA-THIN VAPOR CHAMBERS.....	76
5.1	Model	76
5.1.1	Design for Minimized Wick Thickness	77
5.1.2	Expression for Vapor Core Effective Conductance as a Function of M_v	79
5.2	Results.....	81
5.2.1	Effect of Operating Power and Working Thickness on the Choice of Working Fluid..	
	81
5.2.2	Effect of Operating Temperature on the Choice of Working Fluid.....	84
5.3	Conclusion	84
6.	A VALIDATED TIME-STEPPING ANALYTICAL MODEL FOR 3D TRANSIENT VAPOR CHAMBER TRANSPORT	92
6.1	Model Development.....	92
6.1.1	Geometry, Governing Equations, and Boundary Conditions	92
6.1.2	Scaling Analysis	97
6.1.3	Combined Energy Equation.....	100
6.1.4	Vapor Core Hydrodynamics	102
6.1.5	Coupling Energy Equation with Vapor Hydrodynamics.....	103
6.1.6	Solution to the Combined Energy Equation	104
6.1.7	Wick Hydrodynamics	107
6.1.8	Model Implementation.....	109
6.2	Estimation of Model Accuracy	110
6.3	Results.....	110
6.3.1	Model Validation	110

6.3.2	Time-Stepping Analytical Model Simulation with Multiple Time-Varying Heat Inputs	113
6.4	Conclusions.....	114
7.	ON THE TRANSIENT THERMAL RESPONSE OF THIN VAPOR CHAMBER HEAT SPREADERS: GOVERNING MECHANISMS AND PERFORMANCE RELATIVE TO METAL SPREADERS	129
7.1	Mechanisms Governing Vapor Chamber Transient Behavior.....	129
7.1.1	Numerical Simulation Case Details.....	129
7.1.2	Analysis of The Transient Thermal Response.....	130
7.2	Experimental Demonstration and Comparison with The Model	133
7.2.1	Experimental Facility and Procedure.....	133
7.2.2	Replication of the Experimental Conditions in The Model.....	134
7.2.3	Comparison of Experiments and Simulations	135
7.3	Transient Vapor Chamber Performance Relative to a Copper Spreader	136
7.3.1	Dependence of Relative Transient Performance on Time Scale	136
7.3.2	Effects of Key Parameters on the Transient Performance.....	137
7.4	Conclusions.....	140
8.	ON THE TRANSIENT THERMAL RESPONSE OF THIN VAPOR CHAMBER HEAT SPREADERS: OPTIMIZED DESIGN AND FLUID SELECTION	154
8.1	Simulation Case Details.....	154
8.2	Optimization of the Wall and Vapor-Core Thicknesses.....	154
8.3	Selection of Working Fluid.....	157
8.3.1	Selection Procedure	157
8.3.2	Demonstration of the Procedure	158
8.4	Conclusions.....	160
9.	SUMMARY AND OUTLOOK.....	169
	REFERENCES	170
	APPENDIX A. EFFECTIVE PERMEABILITY FORMULATION.....	175
	APPENDIX B. ESTIMATING THE ACCURACY OF THE TIME-STEPPING ANALYTICAL MODEL.....	176

APPENDIX C. BENCHMARKING THE VAPOR CHAMBER PERFORMANCE RELATIVE TO A COPPER SPREADER	183
VITA.....	184
PUBLICATIONS.....	185

LIST OF TABLES

Table 3.1. Heat-loss calibration data set	41
Table 5.1. Fluid property figures of merit for six fluids at $T_v = 325$ K.	88
Table 6.1. Scales for the model variables.	119
Table 6.2. Properties of the working fluid, copper, and porous wick materials used in the vapor chamber simulations. Vapor properties are shown at a temperature of 300 K.....	120
Table 7.1. Copper and wick properties.	144
Table 8.1. Copper and wick properties.	163
Table 8.2. Fluid property groups for water and methanol.	164

LIST OF FIGURES

Figure 1.1. Illustration of the typical geometry, internal layout, and operation of a vapor chamber	26
Figure 3.1. Schematic diagram of the test section (top inset shows the heater block assembly). 42	42
Figure 3.2. Photograph of the experimental facility.	43
Figure 3.3. Exploded view of the numerical conduction model domain and boundary conditions.	44
Figure 3.4. Comparison of thermocouple temperatures obtained from experiments against those from the simulations at an electrical heat input of 1 W and ambient temperature of 298.2 K. Each bar is an average temperature from each grouping of thermocouples.	45
Figure 3.5. (a) Calibrated numerical model estimates of the heat loss and (b) junction-to-ambient temperature differences, as a function of input power for the copper and aluminum heat spreaders.	46
Figure 3.6. Thermal resistance as a function of power for the solid copper spreader and the vapor chamber.	47
Figure 3.7. Contours of the condenser-side surface temperature for the (a) vapor chamber and (b) solid copper spreader at device heat inputs of approximately 1 W (left) and 2 W (right). Note the different temperature scales.	48
Figure 3.8. Condenser-side surface temperature difference from the mean, normalized by the device power (profile drawn along the length of the device passing through the center).	49
Figure 3.9. Spreading metric for the prototype vapor chamber relative to the solid copper heat spreader as a function of device heat input.	50
Figure 4.1. 2D vapor chamber geometry and mesh details for example case used to verify the behavior and effectiveness of the steady-state-seeking solution algorithm.	66
Figure 4.2. Progression of the (a) mean evaporator temperature (inset shows dashed region at the top left) and (b) evaporator-to-condenser power difference with solution steps for the full transient simulation and with the steady-state-seeking solution algorithm implemented.	67

Figure 4.3. Schematic representation of vapor chamber condenser-surface temperature profile (inset shows the boundary conditions). Performance improvement is measured as a reduction of the peak-to-mean surface temperature.	68
Figure 4.4. (a) Geometry and boundary conditions for the baseline design of the vapor chamber and (b) an axisymmetric section showing internal layout of the wick and vapor domains. Magnified details of the wick and vapor layout for (c) baseline case and (d) grooved condenser wick domain design.	69
Figure 4.5. Results for the baseline, uniformly distributed wick case: contours of (a) temperature (dimensions in the plot are scaled by 20× along the thickness), (b) velocity magnitude in the wick, (c) pressure in the wick, (d) velocity in the vapor core, (e) pressure in the vapor core (parts (b) through (e) are scaled by 90× along the thickness relative to the radius).	70
Figure 4.6. Results for the baseline, uniformly distributed wick case: plots of the radial distribution of (a) temperature and heat flux on the outer condenser-side surface, (b) pressure in the wick, and (c) heat flux due to condensation at the condenser-side wick-vapor interface.....	71
Figure 4.7. Results for the case with the grooved condenser-side wick domain design: plots of the radial distribution of (a) temperature and heat flux on the outer condenser-side surface, (b) pressure in the wick, and (c) heat flux due to condensation at the condenser-side wick-vapor interface.....	72
Figure 4.8. Illustration of the groove width restriction.	73
Figure 4.9. Illustration of the biporous condenser-side wick domain design with radially discrete grooves. The illustration is shown for a wick with three radial sections; the geometry details are not shown to scale.	74
Figure 4.10. Results for the case with the biporous condenser-side wick domain design: plots of the radial distribution of (a) temperature and heat flux on the outer condenser-side surface, (b) pressure in the wick, and (c) heat flux due to condensation at the condenser-side wick-vapor interface.....	75
Figure 5.1. Schematic of the operation and the geometry of a vapor chamber.	89
Figure 5.2. Contours of effective vapor core conductance as a function of the liquid and vapor figures of merit for operating powers of (a) 0.25 W, (b) 1 W, and (c) 3 W. $R = 45$ mm, $R_e = 5$ mm, $t = 100$ μ m, $n = 3$, $F_s = 2$; the wick is sintered copper ($m = 0.21$, $f = 150$) with 60% porosity; thermophysical properties evaluated at 325 K.....	90

Figure 5.3. Plots showing the best working fluids in the power-working thickness space. Properties are calculated at (a) $T_v = 325$ K, (b) $T_v = 350$ K, and (c) $T_v = 375$ K. $R = 45$ mm, $R_e = 5$ mm, $n = 3$, $F_s = 2$; the wick is sintered copper ($m = 0.21$, $f = 150$) with 60% porosity. 91

Figure 6.1. Vapor chamber transport model geometry and boundary conditions (cross-section and bottom views)..... 121

Figure 6.2. Schematic diagram of the simulated geometry and boundary conditions used to validate the time-stepping analytical vapor chamber model, showing a bottom view at the bottom and cross-section at the top for (a) Case #1 (thickness scaled 50 \times), and (b) Case #2 (thickness scaled 25 \times). 122

Figure 6.3. Comparison of temperature results from vapor chamber simulations using the time-stepping analytical model and the finite-volume numerical model for Case #1. (a) The temperature profile is shown along the evaporator-side outer surface (solid lines; $z = 0$ mm, $y = 27.5$ mm) and the condenser-side outer surface (dashed lines; $z = 0.5$ mm, $y = 27.5$ mm), at $t = 44.5$ s. (b) The variation of the maximum temperature in the vapor chamber (at $z = 0$ mm, $x = 45$ mm, $y = 27.5$ mm) with time predicted by the two models is compared..... 123

Figure 6.4. Comparison of pressure results from the vapor chamber simulations using the time-stepping analytical model and the finite-volume numerical model for Case #1. The relative pressure variation in the (a) wick and (b) vapor core are shown for the cross-sectional plane $y = 27.5$ mm at $t = 44.5$ s. 124

Figure 6.5. Comparison of the temperature profile along the evaporator-side outer surface (solid lines; $z = 0$ mm, $y = 27.5$ mm) and the condenser-side outer surface (dashed lines; $z = 1$ mm, $y = 27.5$ mm), at steady-state is shown, from vapor chamber simulations using the time-stepping analytical model and the finite-volume numerical model for Case #2. 125

Figure 6.6. Comparison of pressure results from the vapor chamber simulations using the time-stepping analytical model and the finite-volume numerical model for Case #2. The relative pressure variation in the (a) wick and (b) vapor core are shown for the cross-sectional plane $y = 27.5$ mm at steady state..... 126

Figure 6.7. Schematic diagram of the geometry and boundary conditions used to simulate multiple time-varying inputs with the time-stepping analytical vapor chamber model (thickness scaled 45 \times). 127

Figure 6.8. Time-stepping analytical solution of the (a) maximum temperature at the centers of the two heaters with time; (b) snapshot at $t = 47$ s showing the 3D contours of temperature in the vapor chamber, with z -direction scaled 20 \times (video in Supplementary Materials of the publication [50]) played at 5 \times real-time speed) and temperature contours on the condenser-side outer surface ($z = 0.5$ mm) at (c) $t = 33$ s and (d) $t = 66$ s. 128

Figure 7.1. Geometry (not to scale) and boundary conditions for the transient heat spreading simulations showing (a) a section view for the copper spreader case, (b) a section view for the vapor chamber case, and (c) a bottom view of the evaporator-side that is common to both cases.

..... 145

Figure 7.2. Comparison between the vapor chamber and the copper spreader simulation results ($\delta_{vap} = 40 \mu\text{m}$) showing the temporal variation of the (a) peak temperature θ_p , (b) volume-averaged mean temperature θ_m , and (c) difference between the peak and mean temperatures $\Delta\theta_{p-m} = \theta_p - \theta_m$.

..... 146

Figure 7.3. The profile of local temperature difference from the mean ($\theta - \theta_m$) along a line on the evaporator-side surface of the heat spreader (dashed line in Figure 7.1c) at different times, for (a) the copper spreader and (b) the vapor chamber. Note the different scales of the vertical axis for (a) and (b).

..... 147

Figure 7.4. (a) Photograph of the vapor chamber sample in top view, (b) diagram of the locations of the thermocouple beads and heated length, and (c) illustration of the experimental test setup.

..... 148

Figure 7.5. Experimental measurements of the temperature θ at the five thermocouple locations as a function of time.

..... 149

Figure 7.6. Comparison of the experiment and simulation: (a) temperature at thermocouple location A (θ_A), (b) average surface temperature relative to the ambient temperature (θ_{avg}), and (c) the average difference between the temperatures at B and C ($\Delta\theta_{B-C}$).

..... 150

Figure 7.7. Vapor chamber local surface temperatures difference from the average surface temperature ($\theta - \theta_{avg}$) at the thermocouple locations at different times from (a) the experiment and (b) the simulation.

..... 151

Figure 7.8. Comparison between the vapor chamber and the copper spreader simulation results ($\delta_{vap} = 200 \mu\text{m}$) showing the temporal evolution of (a) peak temperature θ_p , (b) volume-averaged mean temperature θ_m , and (c) difference between the peak and mean temperatures $\Delta\theta_{p-m} = \theta_p - \theta_m$.

..... 152

Figure 7.9. Contour plot of the metric for the thermal performance of a vapor chamber relative to a copper spreader (M_{VC-Cu}), for a range of vapor core thicknesses, and as a function of time for (a) $t < 100$ s and (b) a zoomed-in view for $t < 5$ s. Threshold lines ($M_{VC-Cu} = 0$) for the thermal performance of a vapor chamber relative to that of a copper spreader as a function of time for a range of vapor core thicknesses at different input powers in the range (c) $t < 100$ s and (d) a zoomed-in view for $t < 5$ s.

..... 153

Figure 8.1. Geometry (not to scale) and boundary conditions for the transient vapor chamber simulations showing (a) a section view and (b) a bottom view of the evaporator side. 165

Figure 8.2. Simulated transient response of a vapor chamber for multiple values of vapor-core thickness, showing the temporal variation of the (a) peak temperature θ_p , (b) volume-averaged mean temperature θ_m , and (c) difference between the peak and mean temperatures $\Delta\theta_{p-m} = \theta_p - \theta_m$ 166

Figure 8.3. Simulated vapor chamber peak temperature θ_p as a function of vapor core thickness δ_{vap} (a) at $t = 50$ s and (b) at steady state ($t = 200$ s). 167

Figure 8.4. Selection of the working fluid between water and methanol using the simulated vapor chamber peak temperature θ_p as a function of vapor core thickness δ_{vap} (a) at $t = 50$ s and (b) at steady state ($t = 200$ s). 168

Figure B.1. Schematic diagram of the simulated geometry and boundary conditions used estimate the error in the predictions of the time-stepping analytical vapor chamber model. 180

Figure B.2 Estimated relative error in the difference between the maximum and minimum temperature in the vapor chamber due to the assumption of negligible temperature difference across the thickness of the wall and the wick on the evaporator side, as a function of power (plotted on a log scale) over a range of working thicknesses. 181

Figure B.3. Estimated relative error in the total pressure drop in the vapor chamber as a function of power (plotted on a log scale) over a range of working thickness due to (a) linearizing the Clausius-Clapeyron equation, and (b) neglecting the convection term in the momentum equation for the vapor core. 182

Figure C.1. Contour plot of the metric for the thermal performance of a vapor chamber relative to a copper spreader (M_{VC-Cu}), for a range of vapor core thicknesses, and as a function of time for (a) Case A and (b) Case B..... 183

ABSTRACT

Author: Patankar, Gaurav. PhD

Institution: Purdue University

Degree Received: May 2019

Title: Characterization, Modeling and Design of Ultra-Thin Vapor Chamber Heat Spreaders under Steady-State and Transient Conditions.

Committee Chair: Suresh V. Garimella, Justin, A. Weibel

This dissertation is focused on studying transport behavior in vapor chambers at ultra-thin form factors so that their use as heat spreaders can be extended to applications with extreme space constraints. Both the steady-state and transient thermal transport behaviors of vapor chambers are studied. The steady-state section presents an experimental characterization technique, methodologies for the design of the vapor chamber wick structure, and a working fluid selection procedure. The transient section develops a low-cost, 3D, transient semi-analytical transport model, which is used to explore the transient thermal behavior of thin vapor chambers: 1) The key mechanisms governing the transient behavior are identified and experimentally validated; 2) the transient performance of a vapor chamber relative to a copper heat spreader of the same external dimensions is explored and key performance thresholds are identified; and 3) practices are developed for the design of vapor chambers under transient conditions. These analyses have been tailored to ultra-thin vapor chamber geometries, focusing on the application of heat spreading in mobile electronic devices. Compared to the conventional scenarios of use for vapor chambers, this application is uniquely characterized by compact spaces, low and transient heat input, and heat rejection via natural convection.

Under steady-state conditions and at ultra-thin form factors, the performance-governing transport mechanisms of vapor chambers differ compared to a conventional scenario. Performance is primarily limited by the vapor core thermal resistance, rather than the thermal resistance across the evaporator wick. Additionally, thermal management requirements of mobile electronic devices are increasingly governed by user comfort, and hence vapor chamber performance needs to be characterized by the temperature at its condenser surface. This new paradigm creates a need for new experimental characterization techniques and design methodologies. Also, the heat load in mobile electronic devices is inherently transient in nature. However, no knowledge exists for the transient thermal behavior of vapor chambers. Hence, a new model is developed to solve for

transient transport in vapor chambers. The model is used to identify mechanisms governing the transient thermal behavior of vapor chambers, to compare the transient performance with metal spreaders and to develop design practices for improving transient performance.

In the experimental characterization approach developed in the steady-state section, the evaporator-side and ambient temperatures are measured directly; the condenser-side surface temperature distribution is measured using an infrared camera. The high thermal resistance imposed by natural convection in the vapor chamber heat dissipation pathway requires accurate prediction of the parasitic heat losses from the test facility using a combined experimental and numerical calibration procedure. Performance metrics are developed to characterize heat spreader performance in terms of the effective thermal resistance and the condenser-side temperature uniformity. The performance characterization technique offers a rigorous approach for testing and analysis of new designs of vapor chamber as heat spreaders, with accurate characterization of their performance relative to other heat spreaders.

To design vapor chambers under steady-state conditions, unlike previous approaches that have focused on designing evaporator-side wicks for reduced thermal resistance and delayed dryout at higher operating powers, this work focuses on manipulating the condenser-side wick to improve lateral heat spreading. The proposed condenser-side wick designs are evaluated using a 3D numerical vapor chamber transport model that accurately captures conjugate heat transport, phase change at the liquid–vapor interface, and pressurization of the vapor core due to evaporation. A biporous condenser-side wick design is proposed that facilitates a thicker vapor core, and thereby reduces the condenser surface peak-to-mean temperature difference by 37% relative to a monolithic wick structure.

This work explores the selection of the vapor chamber working fluid under steady-state conditions; in this case, a working fluid is sought that provides the minimal thermal resistance while ensuring a capillary limit is not reached at the target operating power. A resistance-network-based model is used to develop a simple analytical relationship for the vapor chamber thermal resistance (dominated by the saturation temperature gradient in the vapor core) as a function of the working fluid properties, operating power, and geometry. To satisfy the performance objective, it is shown that the choice of working fluid cannot be based on a single figure of merit containing only fluid properties. Instead, the functional relationship for thermal resistance must be analyzed

taking into account all operating and geometric parameters, in addition to the thermophysical fluid properties.

For the transient transport in vapor chambers, while detailed numerical models have been developed, a modeling approach with low computational cost is needed for parametric study and quick assessment of vapor chamber performance in system-level models. The low-cost, transient vapor chamber model developed in this work considers mass, momentum, and energy transport in the vapor chamber wall, wick, and vapor core as well as phase change at the wick-vapor interface. For an example case, the model is demonstrated to have a computational cost reduction of three to four orders of magnitude as compared to using a finite-volume discretized numerical model, but with comparable levels of accuracy. Additionally, an extensive model error estimation is conducted, where the errors in the field-variable computations are estimated by analyzing the simplifying assumptions employed in the model. The estimated errors match with difference in results between the time-stepping analytical model and the finite-volume based model for two extreme cases.

The model is used to identify the three key mechanisms that govern the transient thermal response: (1) the total thermal capacity of the vapor chamber governs the rate of increase of the volume-averaged mean temperature; (2) the effective in-plane diffusivity governs the time required for the spatial temperature profile to initially develop; and (3) the effective in-plane conductance of the vapor core governs the range of the spatial temperature variation, and by extension, the steady-state performance. An experiment is conducted using a commercial vapor chamber sample to confirm the governing mechanisms revealed by the transport model; the model accurately predicts the experimental measurements. The transient performance of a vapor chamber relative to a copper heat spreader of the same external dimensions is explored as a function of the heat spreader thickness and input power. The mechanisms governing the transient behavior of vapor chambers are used to explain the appearance of key performance thresholds beyond which performance is superior to the copper heat spreader.

The knowledge of these key mechanism is utilized to develop notional practices for the design of vapor chambers under transient heat loading. Two key aspect of the vapor chamber design are considered: (1) optimization of the thicknesses of the vapor chamber wall, wick, and vapor core, with a given total available thickness; and (2) selection of the working fluid. Simulations

performed with the time-stepping analytical model are used to identify and demonstrate a procedure for designing the vapor chamber.

This study develops the foundations for the utilization of the vapor chamber technology for thermal management in applications with extreme space constraints and transient heat loads.

1. INTRODUCTION

1.1 Background

A vapor chamber is a phase-change-driven passive heat spreading device. A typical design consists of a hollow chamber with a liquid-saturated porous wick lining its inner surface enclosing a central vapor core. The operation of a vapor chamber is illustrated in Figure 1.1. A localized heat input on the outer surface of the chamber is conducted through the wall, causing evaporation at the wick-vapor interface. Localized vapor generation causes vapor to flow away from the heat input and into the vapor core. The vapor condenses onto the opposing (colder) wick-vapor interface, and the heat is rejected from the condenser surface. Capillary forces in the porous wick draw the condensed liquid back towards the heat input region, enabling continuous passive operation. Mobile electronic devices such as smartphones and tablets are trending toward lower thickness and higher functionality, leading to higher heat generation density from active components. It is not practical to use active air-cooling methods or embed large, finned heat sinks, due to the size constraints. Thus, to minimize the temperature rise of components and surfaces to be cooled by natural convection, heat must be spread uniformly over the device surface. Ultra-thin vapor chambers may offer a viable solution for passive spreading within mobile devices.

Prior studies have assessed the performance of heat pipes and vapor chambers in situations where the heat is spread from a heat source to a cold plate or air-cooled heat sink, and the heater-to-ambient thermal resistance is determined [1]. In mobile electronic platforms, heat is rejected to the ambient via natural convection directly from the device surface (typically a smooth, flat surface that does not incorporate a finned heat sink due to lack of space and the low operating power). Hence, it is necessary to characterize the transport behavior of vapor chambers cooled by natural convection in this configuration. Investigation of vapor chambers operating at a low power density where the condenser-side boundary condition is one of natural convection has not been considered in the literature. Also, due to the proximity of the vapor chamber condenser surface to the outer device surface in thin form factor platforms, an assessment of the condenser-side surface temperature *distribution* is extremely important for ergonomic concerns. This product sector necessitates a paradigm shift in thermal management, where the external surface temperature threshold is dictated by user considerations, rather than by device operating temperature limits.

According to Moritz and Henriques [2], roughly 5 mins of contact with temperatures of ~ 50 °C can cause skin tissue damage; to avoid this condition, performance throttling would be dictated by user comfort standards. Berhe [3] defined ergonomic temperature limits on handheld devices of 41 °C for aluminum surfaces and 43 °C for plastic surfaces. It is clear that previous studies have stressed the total thermal resistance of the vapor chamber as the key performance metric, while few studies analyze the condenser-side temperature distribution. The surface temperature distribution must be considered to assess performance and to develop new designs of vapor chambers, for mobile electronics applications.

Recent research in vapor chamber design has focused on high-performance commercial and military electronics that require heat spreaders capable of dissipating high heat fluxes (over 500 W cm^{-2}) from small areas [4]. At such high heat fluxes, the wall superheat typically induces nucleate boiling in the evaporator wicks. Vapor chamber designs for these applications focus on tailoring the evaporator wick to tolerate operation in the boiling regime without suffering from dryout, in order to take advantage of the reduced evaporator thermal resistance that is characteristic of boiling heat transfer. The requirements of vapor chambers for mobile thermal management are in stark contrast to these high-power-density applications. For mobile applications, vapor chambers must be ultra-thin, on the order of less than 1 mm, and typically operate at significantly lower power inputs and heat fluxes. At such thicknesses and heat fluxes, the thermal resistances across the vapor chamber wall and wick are very low while the lateral temperature gradient in the confined vapor core governs the heat spreading resistance [5]. Boiling is not likely to occur in the evaporator wick. Thus, the design focus for mobile applications must shift away from the evaporator wick structure and toward the layout of the wick and vapor domains. Also, given the ergonomic considerations, improving condenser-surface temperature uniformity is a unique objective in the vapor chamber design process.

The choice of a working fluid is crucial in the design of such vapor chambers. Given the principle of operation of a vapor chamber (a two-phase thermodynamic cycle), the thermophysical properties of the fluid significantly impact its performance. One conventional ‘figure of merit’ used for guiding the choice of working fluid prioritizes maximizing the operating power. This figure of merit is derived by equating the capillary pressure and the pressure drop incurred [6] and is given by

$$M_l = \frac{\gamma \rho_l h_{fg}}{\mu_l} . \quad (1.1)$$

A higher value for this figure of merit indicates that the vapor chamber can operate at a larger power prior to reaching the capillary limit. Yadavalli *et al.* [5] analyzed the performance limitations of a thin heat pipe and developed a figure of merit based on the thermophysical fluid properties that affect the vapor core thermal resistance, given as

$$M_v = \frac{P_v \rho_v h_{fg}^2}{\mu_v R_g T_v^2} . \quad (1.2)$$

A higher value for this figure of merit corresponds to a lower thermal resistance in the vapor core.

While these two prevailing figures of merit are useful in the extreme cases where the exclusive concern is either maximizing total heat dissipation power (M_l) or minimizing vapor chamber thickness (M_v), a more practical design objective is to select a working fluid that provides the minimal thermal resistance while ensuring that the capillary limit is not reached at the target operating power for a given vapor chamber size. These figures of merit are also developed using modeling frameworks that intrinsically assume that the vapor chamber design is held constant when comparing across fluids; however, this may not be an appropriate comparison if the design could be tuned to take advantage of favorable characteristics unique to each candidate fluid.

The evaluation of vapor chamber designs for improved steady-state performance is readily possible because of the extensive modeling tools available and prior knowledge of the mechanisms governing the steady-state vapor chamber transport. To do the same under transient conditions, one needs to understand the mechanisms governing the transient thermal transport in vapor chambers. Thus, there is a need to develop low-cost modeling capabilities for evaluating vapor chamber transient performance. Existing vapor chamber transport models introduce a range of complexities that typically represent a compromise between computational cost and fidelity. Discretized numerical models are capable of simulating the transient behavior of complex vapor chamber geometries under different operating conditions. Such models are only limited by assumptions inherent in the governing equations used to represent the transport mechanisms. However, such numerical models have a relatively high computational cost incurred in iteratively solving the discretized nonlinear governing equations, especially for vapor chamber geometries with high aspect ratios, which require a large number of mesh elements with small cell sizes

dictated by the thinnest dimension. Such numerical models are best suited to single-point evaluation of single device designs. They are, however, not practical for simulating a large number of cases covering a wide range of parameters. Lower cost computational models for vapor chambers and heat pipes have also been developed in the literature, and they solve simplified governing equations analytically. For *steady-state* behavior, models are readily available for all levels of dimensionality. The few examples of low-cost *transient* models did not accommodate boundary conditions corresponding to heat spreading from multiple arbitrarily shaped and located hotspots. Thus, there is a need for a low-cost *transient* vapor chamber transport model that computes the 3D temperature fields in the vapor chamber when subjected to arbitrarily placed, localized transient heat inputs.

Several studies have considered the transient behavior of heat pipes and vapor chambers. However, such studies are limited using either experimental or numerical tools to demonstrate the transient response of specific vapor chambers under specific boundary conditions; they do not attempt to identify the key transport mechanisms that govern the transient response of the vapor chamber. Thus, there is a need to extract an understanding of these transient governing mechanisms in vapor chambers and use this understanding to explore the benefits and limitations in its performance relative to other heat spreading technology and to develop practices for the design of vapor chambers for improved transient performance.

1.2 Objectives and Major Contributions

The main goals of the present work are to: 1) develop a technique for characterizing the performance of ultra-thin vapor chambers for mobile electronics platforms operating at low power and cooled by natural convection; 2) design ultra-thin vapor chambers for improved condenser-surface temperature uniformity, targeting the mobile electronic device platform; 3) provide guidelines for the process of choosing a working fluid that yields the minimum thermal resistance for ultra-thin vapor chambers; 4) develop a low-cost, semi-analytical model for transient vapor chamber operation; and understand the mechanisms governing the transient thermal performance of vapor chambers; and 6) develop practices for the design of vapor chambers under transient conditions.

A novel approach was developed for characterization of vapor chambers of ultra-thin form factor. Given their intended application in mobile electronics platforms, the experimental facilities

are designed to evaluate performance at low heat input powers with heat rejection to the ambient by natural convection. The condenser surface temperature distribution was measured because of the critical ergonomics implications that govern the thermal management requirements for these applications. The high thermal resistance due to natural convection in the heat dissipation pathway necessitates careful calibration of the parasitic heat losses from the system. A calibration process was developed, which combines experimental and numerical methods to formulate a correlation for the heat loss as a function of surface temperature and electrical input power. A vapor chamber prototype was tested to demonstrate the metrology developed for characterizing the thermal resistance and condenser-side surface temperature uniformity. Comparing the performance of the vapor chamber to a copper heat spreader using the proposed condenser-surface-temperature-uniformity based metrics revealed that vapor chambers may redistribute the condenser-side surface temperature with increasing power, beyond what is possible with heat spreading by conduction alone.

Performance-enhancement strategies are developed in this work that provide a pathway for effectively introducing vapor chambers into mobile devices for thermal management. It was concluded that condenser-surface temperature uniformity is governed by the layout of the condenser-side wick; uniformity can be improved by increasing condenser-side wick permeability in order to reduce its thickness, and thereby increase the vapor-core thickness for lowered lateral thermal resistance. A hypothetical design implementing these two strategies was simulated and revealed that the second strategy can yield significant improvement in the condenser-surface temperature uniformity. A biporous condenser-side wick design was developed on this principle; numerical simulations comparing the baseline and biporous condenser-side wick designs showed that the peak-to-mean condenser surface temperature difference of the vapor chamber could be reduced by up to 37%. The approach developed can be adopted to produce vapor chamber wick designs in coordination with practical fabrication constraints.

Based on a design target of minimizing thermal resistance in ultra-thin vapor chambers, a simplified analytical relationship is proposed between the vapor core thermal conductance and two fluid figures of merit (M_l representing liquid properties and M_v representing vapor properties), which was necessary because the individual metrics by themselves are not sufficient for selecting working fluids at this form factor. A methodology for selecting between working fluids for a given

set of ultra-thin vapor chamber geometric and operating parameters was developed. The effects of important operating conditions and parameters on the choice of the working fluid were investigated

A transient model for vapor chamber operation was developed that allows for multiple, arbitrarily shaped, time-varying heat inputs on the evaporator-side face; the model predicts 3D fields of temperature, pressure, and velocity in the vapor chamber. The errors in the temperature and pressure fields computed by the time-stepping analytical model, due to the simplifying assumptions employed in the model development, were estimated. The model has low errors for cases from low- to high-power applications (less than 10 % for a majority of the simulated cases). The model is validated against a finite-volume-based numerical model for two cases, one for a low power application and one for a high power application. Based on this validation case, the newly developed time-stepping analytical model was demonstrated to have 3-4 orders of magnitude lower computational cost compared to the numerical model while maintaining physical accuracy. This model was then used to simulate the behavior of a vapor chamber subjected to multiple, time-varying heat input boundary conditions to demonstrate the capability of the time-stepping analytical model to resolve the transient 3D thermal response to complex boundary conditions expected in real-world applications.

The model for vapor chamber transport was used to simulate the transient behavior of a vapor chamber and a solid copper heat spreader. Comparison of the temporal temperature fields in the two devices was used to identify and understand the key mechanisms that govern the transient behavior and performance of vapor chambers. Experiments were conducted with a commercial vapor chamber and compared to predictions from the model to demonstrate the key governing mechanisms identified. Lastly, the transient performance of a vapor chamber relative to a copper heat spreader of the same external dimensions was explored as a function of two key parameters, namely the heat spreader thickness and input power. Thresholds were identified beyond which the vapor chamber offers improved performance relative to the copper heat spreader. The relationship between the key governing mechanisms and the transient performance thresholds was established.

This knowledge of the key mechanism was utilized to develop notional practices for design of vapor chambers under transient heat loading. Two key aspect of the vapor chamber design were considered: (1) optimization of the thicknesses of the vapor chamber wall, wick, and vapor core, with a given total available thickness; and (2) selection of the working fluid. Simulations

performed with the time-stepping analytical model were used to identify and demonstrate a procedure for designing the vapor chamber.

1.3 Organization of the Document

Chapter 1 contained the background information regarding characterization techniques, design methods, working fluid selection criteria, and modeling of vapor chambers, focusing on the application of heat spreading in mobile electronic devices. It also contained the objectives and major contributions of this work. Chapter 2 presents a review of the literature regarding characterization techniques, design methods, working fluid selection criteria, modeling of vapor chambers, and the transient analysis of vapor chambers. Chapter 3 presents a new characterization approach for ultra-thin vapor chambers operating at low powers and cooled by natural convection. Chapter 4 presents performance enhancing strategies for using ultra-thin vapor chambers as heat spreaders in mobile electronic devices and develops and tests new wick designs based on these strategies. Chapter 5 provides a new methodology for selecting working fluid so as to minimize thermal resistance in ultra-thin vapor chambers. Chapter 6 presents a transient model for vapor chamber operation that allows for multiple, arbitrarily shaped, time-varying heat inputs on the evaporator-side face; the model predicts 3D fields of temperature, pressure, and velocity in the vapor chamber. Chapter 7 presents an analysis identifying the key mechanisms governing the transient thermal transport in vapor chambers and identifies the benefits and limitations of using vapor chambers over metal spreaders for a range of vapor chamber parameters and time scales. Chapter 8 presents practices for the design of vapor chambers under transient conditions.

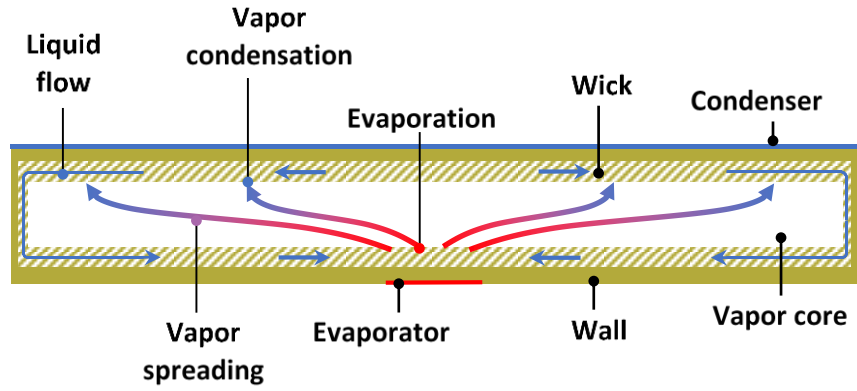


Figure 1.1. Illustration of the typical geometry, internal layout, and operation of a vapor chamber

2. LITERATURE REVIEW

This chapter presents a review of the literature pertaining to the experimental performance characterization, design, modeling and transient analysis of vapor chambers.

2.1 Experimental Performance Characterization of Vapor Chambers

In a testing configuration closely related to the current study, where the testing facility is designed to evaluate the condenser-surface performance at low heat input powers with heat rejection to the ambient by natural convection, Wang *et al.* [7] investigated copper vapor chambers that contained interlaced grooves and channels as the wick structure. The hot spot heat input was supplied through a copper platen with an embedded rake of thermocouples for heat flux measurement. Heat was rejected on the condenser side using a finned heat sink cooled by forced air convection. Thermal grease was used to reduce contact resistance between the vapor chamber and the heat sink; thermocouples were embedded in this grease layer between the heat sink and the vapor chamber to measure surface temperatures. The thermal performance of the vapor chamber was assessed based on its thermal resistance and condenser-side temperature uniformity [7]. This vapor chamber testing configuration has commonly been used [8–11]. Other variants use a liquid-cooled cold plate on the condenser side [12]. This testing configuration is tailored for high-power or high-density cooling applications for which the heat flux induces a large temperature gradient in the heater platen that can be accurately measured, and where the condenser-side heat rejection method mimics the intended application. For example, Mochizuki *et al.* [11] tested input heat fluxes from 20 to 100 W over 1 cm², Wong *et al.* [8] from 300 to 400 W over ~1–4 cm², and Chen *et al.* [10] from 20 to 80 W over ~2 cm². The lowest reported heat fluxes investigated under this vapor chamber testing configuration include measurements by Koito *et al.* [13] from 16 to 32 W cm⁻² and Wang *et al.* [5] from ~4 to 10 W cm⁻².

2.2 Design of Vapor Chambers

Wick design strategies in the literature have analyzed the ability of wicks to evacuate vapor bubbles generated during boiling in order to avoid dryout and reduce the thermal resistance [14]. This has been achieved through patterning the wick structure [15] or using biporous wicks [16] to

enable continuous feeding of liquid to the evaporator under boiling conditions. Alternate strategies aim to reduce the evaporator wick thermal resistance and preserve operation in the evaporative regime (avoiding boiling) using thin nanostructure arrays [17, 18] or thin monoporous copper particles with arterial liquid return paths [12, 19].

There is a fledgling body of literature that has investigated the design of ultra-thin heat pipes or vapor chambers. Aoki *et al.* [20] fabricated heat pipes with thickness less than 1 mm by simply flattening traditional cylindrical grooved heat pipes. Ding *et al.* [21] developed a titanium-based vapor chamber with a thickness of 0.6 mm that included a uniform array of microfabricated titanium pillars as the wick structure. Oshman *et al.* [22] fabricated a 1 mm-thick heat pipe with a hybrid copper mesh and micropillared wick encased in a liquid-crystal polymer chamber. Lewis *et al.* [23] fabricated a 0.5 mm-thick flexible heat pipe made of copper-cladded polyimide, with a copper mesh wick. In each of these studies, the wick was designed to allow dissipation of the maximum possible power and/or minimum evaporator-to-condenser thermal resistance at an ultra-thin form factor.

2.3 Vapor Chambers Transport Models

Vadakkan *et al.* [24] and Ranjan *et al.* [25, 26] developed a finite-volume-based numerical model to solve the mass, momentum, and energy transport equations in the wall, wick, and vapor core of the vapor chamber, coupled with phase change at the wick–vapor interfaces. A model solving the same governing equations using the finite-volume method was developed by Famouri *et al.* [27] using cylindrical coordinates to model the behavior of heat pipes. Harmand *et al.* [28] developed a transient 3D finite-difference based numerical model for vapor chambers that solves governing equations which are simplified by assuming control volumes that span the thickness of the wick and the vapor-core separately.

Prasher [29] and Yadavalli *et al.* [5] developed a 1D resistance-network-based model that predicts the steady-state temperature drop by assigning thermal resistances to each primary heat transport pathway in the heat pipe. Aghvami and Faghri [30] and Lefevre and Lallemand [31] respectively developed analytical models for computing 2D and 3D steady-state temperature fields in vapor chambers with arbitrary heat inputs. Zhu and Vafai [32] developed an analytical model that computed the transient temperature variation along the length and thickness of a vapor chamber. But the model utilized symmetry in the geometry and boundary conditions and thus did

not accommodate boundary conditions corresponding to heat spreading from multiple arbitrarily shaped and located hotspots.

2.4 Transient Analysis of Vapor Chambers

Several studies have considered the transient behavior of heat pipes and vapor chambers. El-Genk and Lianmin [33] experimentally studied the heat-up and cool-down of a heat pipe under a range of evaporator-side input powers and condenser-side coolant flow rates, concluding that the transient vapor temperature profiles could be locally represented by an exponential function in the cases investigated. Tournier and El-Genk [34] developed a finite-volume-based model to simulate the mass, momentum and thermal transport in the vapor chamber wick to predict pooling of the liquid phase at the condenser. Zhu and Vafai [32] developed a model for heat spreading from a central heater in disk-shaped and rectangular vapor chambers. The analytical model solved for 1D transient conduction in the vapor chamber wall and wick while the quasi-steady vapor hydrodynamics was modeled using an assumed spatial velocity profile. The model was used to simulate the startup process of a vapor chamber in terms of the transient temperature and velocity fields. Harmand *et al.* [28] developed a finite-volume-based transport model to predict the transient behavior of rectangular vapor chambers. The model was validated against experiments, and the model capabilities were then demonstrated under several different heating configurations (spatial and temporal). Similarly, [24, 9, 35, 36, 27] present models for the transient transport in vapor chambers and compare them against experiments.

3. THERMAL PERFORMANCE CHARACTERIZATION OF ULTRA-THIN VAPOR CHAMBERS COOLED BY NATURAL CONVECTION

This chapter presents an approach for characterizing the performance of ultra-thin vapor chambers for mobile electronics platforms operating at low power. An experimental test facility is developed that subjects the vapor chamber to a hot spot on the evaporator side and rejects heat from the condenser side by natural convection. Precise evaluation of performance at very low power densities ($\sim 1 \text{ W cm}^{-2}$) is enabled by a combined experimental and numerical approach for calibration of the heat transport through the vapor chamber. Keeping the heat source at the minimum possible temperature and mitigating hotspots on the condenser surface are key functional requirements. Hence, in addition to the conventional thermal resistance metric, IR measurement of the condenser-side surface temperature allows characterization of the vapor chamber performance in terms of temperature distribution. The assessment is based on the performance of an ultra-thin vapor chamber relative to a solid heat spreader with identical outer dimensions. The material in this chapter was presented at the *ASME 2015 International Technical Conference and Exhibition on Packaging and Integration of Electronic and Photonic Microsystems* in 2015 and published in the proceedings [37]. It was later invited for publication in the *Journal of Electronic Packaging* [38].

3.1 Experimental Facility

An experimental facility is developed to evaluate the performance of ultra-thin vapor chambers at low heat loads. The intrinsic challenge in vapor chamber characterization under such conditions is estimation of the percentage of heat input rejected through the vapor chamber versus parasitic losses through other pathways. To measure extremely low heat loads, a test section is typically designed to eliminate heat losses (an isolated system, e.g., Ref. [1]). To evaluate performance of a vapor chamber rejecting heat to the ambient via natural convection, which inserts a large associated thermal resistance in the primary heat rejection pathway, it is difficult to create a sufficiently isolated system. An alternative approach is to control the heat losses in a manner that allows for accurate estimation and calibration, as implemented in the current study.

3.1.1 Test Section Design and Instrumentation

A schematic diagram of the test section configuration is shown in Figure 3.1. The test section is comprised of the heat spreader sample, with insulation and a centered heater block on the underside; the top side of the heat spreader is exposed to ambient air. The test section insulation is made of PEEK ($k = 0.25 \text{ W m}^{-1} \text{ K}^{-1}$) with outer dimensions of $150 \text{ mm} \times 115 \text{ mm} \times 25.4 \text{ mm}$. A $92 \text{ mm} \times 52 \text{ mm} \times 0.7 \text{ mm}$ deep recess milled into the top surface of the insulation seats the heat spreader sample. In the center, a $10 \text{ mm} \times 10 \text{ mm}$ square pocket was machined to insert the heater block assembly. As shown in the inset of Figure 3.1, the hot spot heat input is simulated using a $10 \text{ mm} \times 10 \text{ mm}$ thin-film polyimide heater attached using thermally conductive paste to the base of a 10 mm copper heater block that ensures uniform distribution of the heat load imposed on the spreader. A uniform, thin layer of high-conductivity epoxy was applied onto the bottom surface of the heat spreader to cover the area overlapping the copper heater block. This allowed a consistent joint to be formed between the heat spreader and heater block across all samples to yield consistent calibration. The top surface of the vapor chamber is cooled by natural convection to the surrounding air.

A photograph of the experimental facility is shown in Figure 3.2. A sample is shown inserted into the test section, and the auxiliary components for temperature and power measurements are visible. The spatial temperature distribution on the top surface of the heat spreader is measured by a mid-wave IR camera (Indigo Merlin MID, FLIR) positioned above the test section. Visualization of the surface temperature via an IR camera allows for the development of performance metrics based on the surface temperature distribution. Calibration of the IR camera measurement was carried out using a reference black body (Blackbody Source Model 2004, SBIR) with a known emissivity (0.985 ± 0.015). The temperature of the black body was incremented in steps of $5 \text{ }^\circ\text{C}$ from $20 \text{ }^\circ\text{C}$ to $100 \text{ }^\circ\text{C}$. From the recorded images, a pixel-by-pixel calibration of the surface temperature versus sensor output was performed. A sixth-order polynomial curve was fit to the data to obtain a correlation between sensor output and temperature. Subsequent evaluation of the calibration at selected blackbody reference temperatures in the $20 \text{ }^\circ\text{C}$ to $100 \text{ }^\circ\text{C}$ range showed a maximum mean error averaged over the field of view of $0.2 \text{ }^\circ\text{C}$. The top surface of the heat spreader sample is painted black (#1602, Krylon) to impart a known emissivity of 0.96 [39]; the ratio of the calibration black body emissivity to the surface emissivity is used to correct the IR temperature measurement.

As shown in Figure 3.1, a total of 30 thermocouples are embedded throughout the insulation block to monitor the temperature. In particular, the thermocouple locations are classified into groupings of those embedded under the top, side, and bottom surfaces (four each) and in the middle of the insulation block (nine). Eight thermocouples are placed in grooves along the surface in contact with the bottom of the heat spreader. Finally, a thermocouple is inserted at the center of the copper heater block to measure the junction temperature. This deployment of thermocouples is essential to the calibration procedure used for estimation of the heat loss from the insulation block, as described in the following section. Each thermocouple was individually wired to a reference junction that is placed in a dry-block ice point reference (TRCIII, Omega). The thermocouples were individually calibrated using a thermostatic oil bath (7103 Micro-Bath, Fluke) and two factory-calibrated resistance temperature detectors (RTD, $\pm 0.1\text{K}$), one each for the ice point and the oil bath. Following calibration, the thermocouple temperature measurements have an absolute uncertainty of $\pm 0.3\text{ K}$. The ambient temperature is measured using an RTD.

The electrical power supplied to the film heater is determined by measuring the voltage drop across the resistance heating element and across a shunt resistance placed in series with the film heater. The electrical input power has a measured uncertainty of 0.2% (governed by the shunt resistance uncertainty).

3.1.2 Test Procedure

A strict experimental procedure is followed for all tests to ensure repeatability of the measurements. The IR camera is switched on at least 1 hr prior to starting the test to ensure that the sensor cools down to a steady temperature for reduced noise in the images. Boards are placed around the test section so as to prevent air flow disturbances in the surrounding ambient. To acquire each data point, the electrical power input to the heater is set at the desired value; all the monitored data are recorded every 4 s using an NI cDAQ 9178 data acquisition chassis with NI 9124 thermocouple, NI 9217 RTD, and NI 9205 voltage input modules. Active data processing is performed in a LABVIEW interface to determine when steady-state conditions have been reached, defined as when the standard deviation of the junction temperature for the last 150 data points is less than 0.02 K. The time usually taken to reach steady-state conditions is approximately 3 hrs. After steady-state conditions are reached, the performance is monitored for an extended period (~30 min) to obtain a large steady-state data set; IR images are acquired at 5-min intervals during

this period. Due to the small fluctuations in ambient temperature that affect the test section temperatures at steady state, a set of 150 data points is selected from the steady-state data set which has the lowest standard deviation in junction temperature. An average over these data is used for subsequent analysis, and associated with the specific steady-state IR image taken during this interval. This procedure for acquiring a single data point is repeated for each heat input power.

3.2 Calibration of the Test-Section Heat Loss

A calibration procedure is implemented that predicts heat loss from the test section. The experimental step of the calibration procedure evaluates heat spreading in two thin metal plates of known thermal conductivity, viz., copper and aluminum. The test section temperatures were recorded for heat loads in the nominal range of 0.15–4 W. Key characteristics of the metal heat spreaders used for the calibration process are listed in Table 3.1.

A numerical model of the test section is generated to simulate conduction in the heater block assembly, insulation block, and heat spreader. As shown in Figure 3.3, the model boundary conditions have a constant heat flux applied at the base of the heater block, a thermal resistance at the interface between the insulation and heat spreader, and convection coefficients on each external surface. A grid-independent rectangular mesh is used to discretize the geometry using a total of ~325,000 cells. The peripheral regions of the insulation block have a uniform coarse mesh; the solution is insensitive to further refinements because of the low temperature gradients in these regions. The copper heater block assembly has a finer mesh. In the heat spreader, a gradient-based mesh is used for refinement near the hotspot. The lateral cell lengths increase in the outward direction from 0.25 mm to 2.25 mm. There are 20 cells across the thickness of the heat spreader near the hotspot. The properties of the heat spreader are specified for the sample being tested according to Table 3.1. The governing energy equation is solved using the finite-volume method implemented in the commercial software ANSYS FLUENT [40].

The primary objective of the numerical model is to predict the boundary conditions and overall heat losses that cannot be determined directly from the available experimental data. A formal procedure is implemented in order to iterate on the boundary conditions in the model in order to produce good agreement between the experimental and numerical values of temperature at the locations in the test section measured by thermocouples. For each calibration data point, the free variables in the numerical simulation are the heat transfer coefficients on the top, side, and bottom

surfaces of the insulation block and the heat spreader top surface. Tuning of the thermal resistance at the interface between the insulation and heat spreader to a fixed value of $0.02 \text{ m}^2 \text{ K W}^{-1}$ across all test cases yielded the best agreement with experimental data (equivalent to an air gap thickness of 0.5 mm).

For the initial guess value, a prediction of the natural convection heat transfer coefficient at each surface with a different orientation obtained from standard correlations was imposed, and then was subsequently iterated to generate a match with the thermocouple data. Priority was given to first match the junction temperature closest to the heat source, and then finer adjustments to the boundary heat transfer coefficients (increments of $0.5 \text{ W m}^{-2} \text{ K}^{-1}$) were made to minimize the overall average deviation from the experimental temperature data. Simple rules were applied that ensure the heat transfer coefficients increased from the downward to upward facing surfaces according to the physical behavior expected. With a sufficient match to the experimental data, the heat transported through the heat spreaders and the heat loss through the insulation block can be easily extracted from the numerical data.

The values of the external heat transfer coefficients were found to be in the range from 4 to 16 $\text{W m}^{-2} \text{ K}^{-1}$. In the current study, where low heat loads are applied and the overall heat loss is a significant percentage of the overall heat input, a single value for the heat transfer coefficient on all exposed surfaces did not yield sufficient accuracy in the match between experimental and numerical temperatures. When these values were allowed to independently vary, the temperature mismatch between the measured and computed values was significantly decreased for all test cases.

The temperature mismatch between the test and the simulation, averaged over all the cases, is 0.34 K, with a standard deviation of 0.56 K. Figure 3.4 shows a comparison between the simulated temperatures after iterating on the boundary conditions compared with the measured values for a selected copper spreader test case. The thermocouple groups (as discussed in Section 3.1.1) are on the bottom, side, and top surfaces of the insulation block, inside the insulation block (internal), embedded below the heat spreader, and at the junction. For the selected case, the junction temperature is matched most closely (difference of 0.02K); the maximum difference is observed for the heat spreader group of thermocouples (difference of 0.71K).

Using this calibration procedure, the uncertainty in the evaluated heat loss from the test section is roughly estimated based on both the resolution of the heat transfer coefficient increments used

during the iteration process and the ultimate temperature mismatch at the surface-embedded thermocouple locations. Using these component uncertainty values for each case, and expressing the heat loss as a single equation of the form

$$Q_{loss} = h \times A \times (T - T_{amb}), \quad (3.1)$$

a standard propagation of errors can be used estimate the uncertainty in the predicted heat loss; this uncertainty varies from 3% to 14% of the calculated heat loss for the test cases described in Table 3.1.

The heat loss values extracted from the calibration of the copper and aluminum heat spreaders are plotted in Figure 3.5(a). A generalized regression is developed for the heat loss value as a function of the electrical input power and the junction-to-ambient temperature difference, as given by

$$Q_{loss} = \left[a \times \left(\frac{T_j - T_{amb}}{Q_{ele}} \right)^b \right] Q_{ele} \quad (3.2)$$

This form of the equation assumes that the heat loss value is proportional to the electrical input power (and that there is no heat loss at zero input power). This relationship can be clearly observed in Figure 3.5(a) (dashed lines indicate best linear fit to the data points). The proportionality constant would then depend on the thermal resistance of the sample being tested. The ratio of junction-to-ambient temperature difference and the electrical input reflects this thermal resistance. By evaluating the thermal resistance of both the copper and aluminum heat spreaders, as shown in Figure 3.5(b), the influence of the junction-to-ambient temperature on the overall heat loss can be incorporated into the regression. The result of the calibration yields the constants $a = 0.14$ and $b = 0.57$, which can subsequently be used to calculate the heat losses through the insulation block when evaluating heat spreading devices that have an unknown thermal resistance and heat spreading behavior. The values of these constants are specific to the current test section design; a similar calibration procedure would need to be employed with any change in the experimental setup.

3.3 Results and Performance Metrics

A representative vapor chamber device with outer dimensions of 90 mm × 50 mm × 0.8 mm, obtained from a commercial vendor, is characterized to demonstrate the testing approach developed. The copper vapor chamber has 0.2 mm-thick copper walls, uses water as the working fluid, and is lined with a single layer of copper mesh (pore sizes of approximately 50–100 μm). The heat spreading behavior of the vapor chamber is evaluated for 12 device power levels (electrical heat input minus losses) ranging from 0.4 to 2.2 W, and resulting in vapor chamber area-weighted mean condenser-side surface temperatures from 24.2 °C to 50.3 °C, and maximum condenser-side surface temperatures in the range of 32.8 °C to 55.9 °C. During testing, the ambient air temperature fluctuated from 22.2 °C to 24.0 °C. The data obtained from the tests were used to assess the behavior of the vapor chamber relative to the solid copper heat spreader of the same dimensions.

The key functional requirements of the vapor chamber are to keep the heat source at the lowest possible temperature and to mitigate any hot spots in the temperature profile on the condenser side for ergonomic comfort. Performance metrics are proposed based on these criteria as a standard approach to evaluating and comparing between thin vapor chambers and alternative heat spreader designs.

3.3.1 Device Thermal Resistance.

A common metric used for defining the thermal resistance of heat pipes and vapor chambers is the junction-to-ambient temperature rise as a function of device power [11]. However, the large thermal resistance contributed by the condenser-side natural convection (in addition to the comparatively smaller thermal resistances of the copper block and conductive epoxy layer) should be omitted from the device thermal resistance assessment for the current configuration, since its inclusion would mask any variations in performance of the actual device under test. The device thermal resistance is instead characterized using the difference between the evaporator temperature (T_e) and the area-averaged condenser-side surface temperature ($T_{s,m}$) shown as a function of heat input for the vapor chamber and copper spreader in Figure 3.6. The uncertainty in device power is the same as the computed heat loss (uncertainty in the electrical input power is negligible). The constant intrinsic thermal conductivity of the copper heat spreader yields a linear behavior. The vapor chamber performance is nonlinear and shows a crossover at approximately 1.5 W, above

which it performs better than the copper heat spreader. One reason for this nonlinear behavior for the ultra-thin vapor chamber tested can be attributed to its governing transport mechanism. The predominant contribution to the temperature rise across the vapor chamber is the vapor-core temperature gradient (related to the vapor pressure gradient via the Clausius–Clapeyron relation). Hence, for ultra-thin vapor chambers, the thermal resistance relative to a solid heat spreader is governed by the vapor temperature gradient, as shown by Yadavalli et al. [5]. The vapor figure of merit defined in Ref. [5] captures this effect and increases with operating temperature for water; thus, a performance increase with power input, which raises the vapor chamber mean temperature, is expected.

3.3.2 Surface Temperature Distribution.

A surface temperature-related spreading metric is developed to characterize the condenser-side temperature profile of the vapor chamber for ergonomics considerations. The contour plot in Figure 3.7 shows the condenser side temperature (T_s) distributions for the copper heat spreader and vapor chamber for two different heat input powers selected to be above and below the thermal resistance crossover. For the power input above the performance crossover, the vapor chamber qualitatively exhibits better spreading as compared to the copper spreader (as indicated by the reduced contour color gradient). This characteristic is captured by a surface spreading performance metric as developed below.

The condenser-side surface temperature data obtained from each image pixel are processed to evaluate the surface spreading metric. The difference between the local surface temperature and the mean surface temperature is first normalized by the device heat input as

$$T_{norm}(x, y) = \frac{(T_s(x, y) - T_{s,m})}{Q}. \quad (3.3)$$

Figure 3.8 shows this value along the center length of the condenser-side surface. For the solid copper spreader, the profile is independent of the heat input power, due to the constant thermal conductivity of copper. The same normalization is then applied to the vapor chamber, for which the profile is seen to flatten with increasing device power. A measure of the overall temperature uniformity of the condenser-side surface is the inverse of the root mean square value of T_{norm} taken across all pixels. Taking a ratio of this quantity for the vapor chamber to that of the solid

copper spreader yields a metric for the surface temperature spreading performance relative to the solid copper spreader

$$\text{Spreading metric} = \frac{\left(1 / \text{RMS} \left(\frac{T_s - T_{s,m}}{Q} \right) \right)_{VC}}{\left(1 / \text{RMS} \left(\frac{T_s - T_{s,m}}{Q} \right) \right)_{Cu}}. \quad (3.4)$$

This metric weighs the relative ability of each heat spreader to affect a uniform condenser-surface temperature profile. For an ideal heat spreader, the temperature profile would be a uniform temperature on the condenser surface at $T_{s,m}$ if the convective boundary condition on the condenser is uniform. The spreading metric would tend to infinity for an ideal heat spreader. The spreading metric results for the vapor chamber tested in the current study are plotted in Figure 3.9. A value of 1 indicates that the vapor chamber and the copper spreader perform identically. The plot in Figure 3.9 shows an increasing performance of the vapor chamber with increasing power, and a crossover at $\sim 2\text{W}$. The spreading metric can be used to compare any heat spreaders of the same dimensions to evaluate the spreading capability.

3.4 Conclusions

A novel approach was developed for characterization of vapor chambers of ultra-thin form factor. Given their intended application in mobile electronics platforms, the experimental facilities are designed to evaluate performance at low heat input powers with heat rejection to the ambient by natural convection. The condenser surface temperature distribution was monitored because of ergonomics implications that govern the thermal management requirements for these applications. The high thermal resistance due to natural convection in the heat dissipation pathway necessitates careful calibration of the parasitic heat losses from the system. A calibration process was developed, which combines experimental and numerical methods to formulate a correlation for the heat loss as a function of surface temperature and electrical input power. A vapor chamber prototype was tested to demonstrate the metrology developed for characterizing the thermal resistance and condenser-side surface temperature uniformity. Comparing the performance of the vapor chamber to a copper heat spreader using the proposed metrics revealed that vapor chambers may redistribute the condenser-side surface temperature with increasing power, beyond what is possible with heat spreading by conduction alone.

The testing methodology developed is an important tool for the development of vapor chambers and heat spreaders intended for use in mobile electronics platforms. Vapor chamber designs can thereby be characterized and compared using a standard approach.

Nomenclature

A	area (m^2)
h	convection coefficient ($\text{Wm}^{-2}\text{K}^{-1}$)
Q	heat input to the heat spreader (W)
Q_{ele}	electrical power (W)
Q_{loss}	heat loss through the insulation (W)
T	temperature (K)

Subscripts

amb	ambient
j	junction
e	evaporator
s	surface
m	mean
Cu	copper spreader
VC	vapor chamber
$bottom$	PEEK insulation bottom surface
top	PEEK insulation top surface
$side$	PEEK insulation side surface
$norm$	normalized

Table 3.1. Heat-loss calibration data set

	Copper	Aluminum
Thermal conductivity ($\text{Wm}^{-1}\text{K}^{-1}$)	387.6	202.4
Outer dimensions (mm)	$90 \times 55 \times 0.7$	$90 \times 51 \times 0.635$
Electrical heat input (W)	0.17 - 4.16	0.16 - 3.88
# of data points	8	10

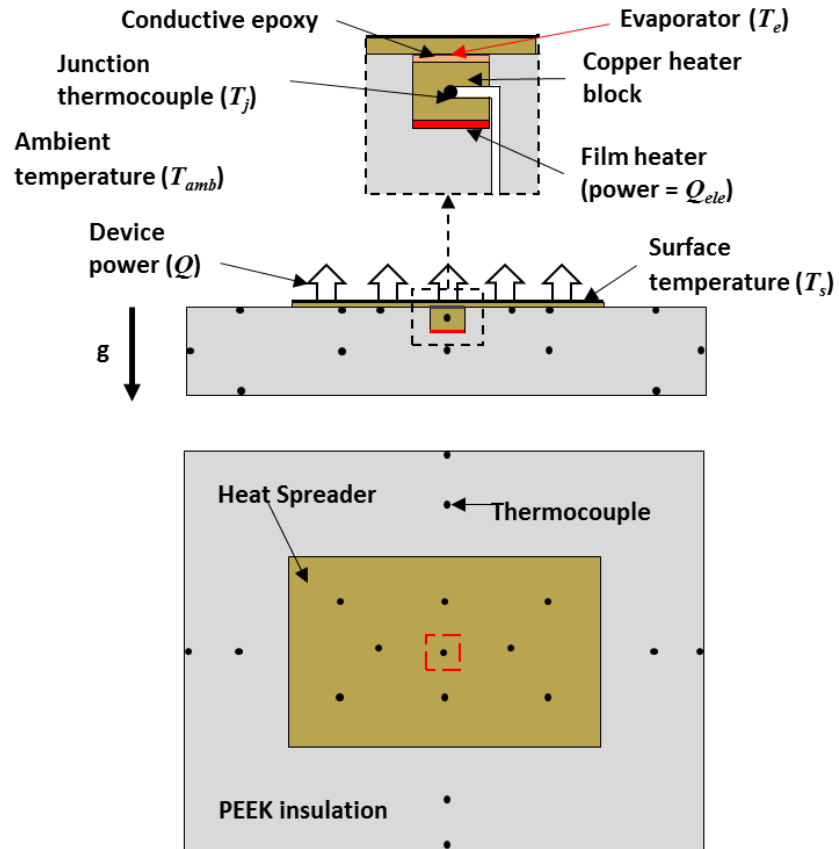


Figure 3.1. Schematic diagram of the test section (top inset shows the heater block assembly).

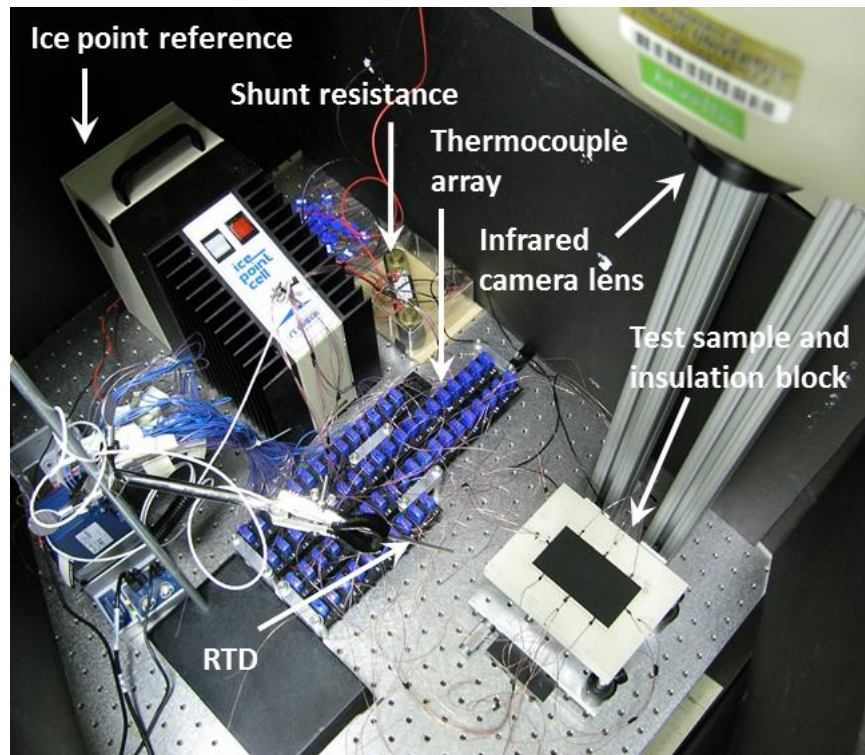


Figure 3.2. Photograph of the experimental facility.

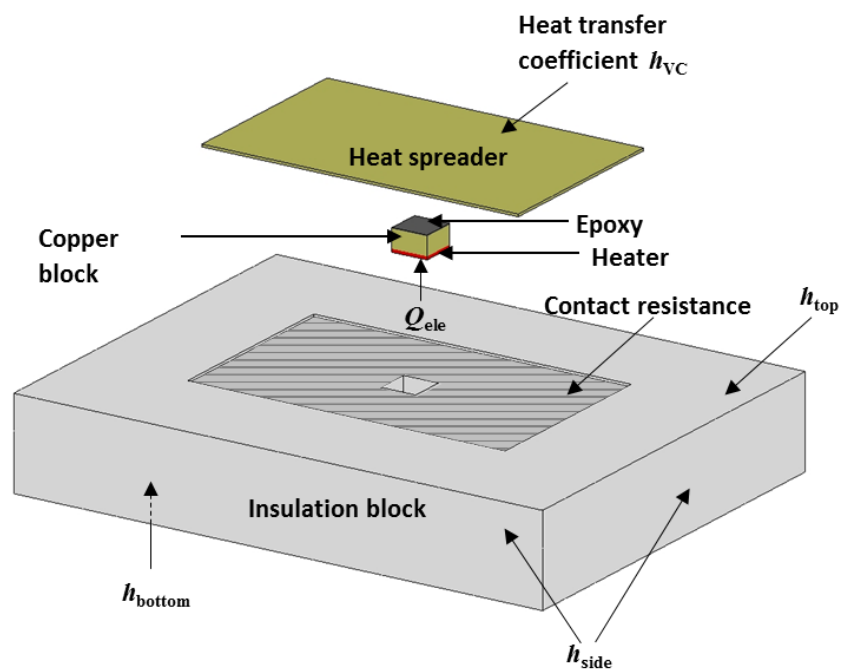


Figure 3.3. Exploded view of the numerical conduction model domain and boundary conditions.

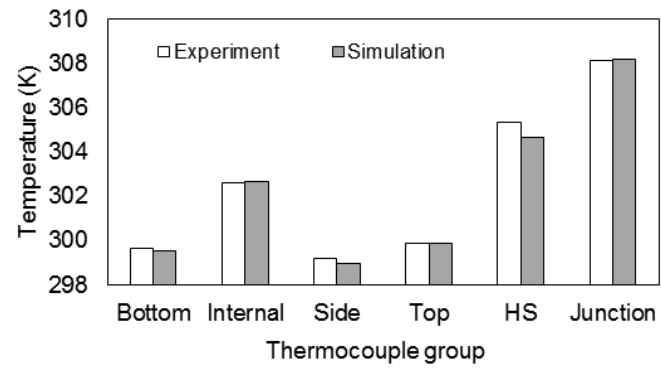


Figure 3.4. Comparison of thermocouple temperatures obtained from experiments against those from the simulations at an electrical heat input of 1 W and ambient temperature of 298.2 K. Each bar is an average temperature from each grouping of thermocouples.

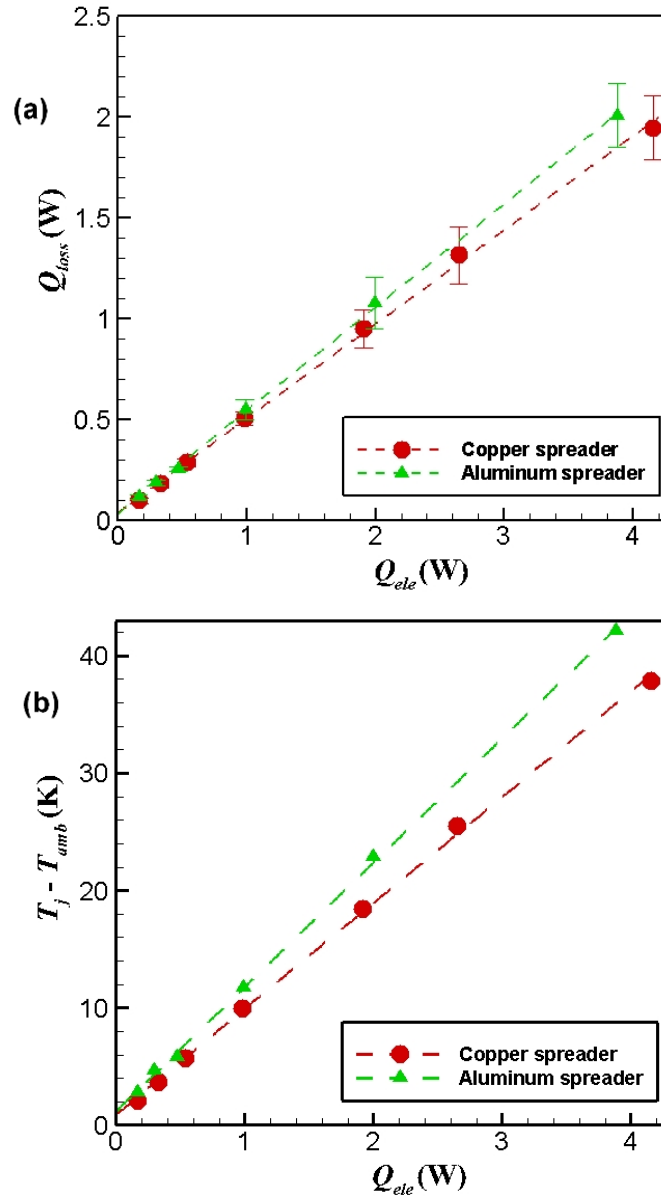


Figure 3.5. (a) Calibrated numerical model estimates of the heat loss and (b) junction-to-ambient temperature differences, as a function of input power for the copper and aluminum heat spreaders.

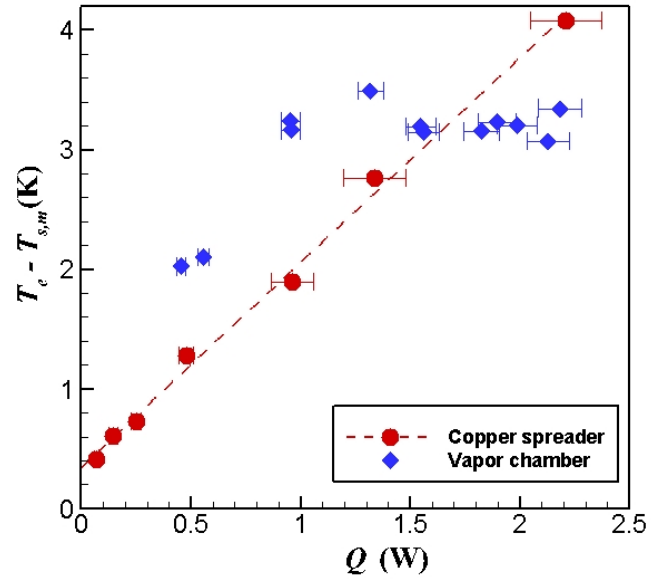


Figure 3.6. Thermal resistance as a function of power for the solid copper spreader and the vapor chamber.

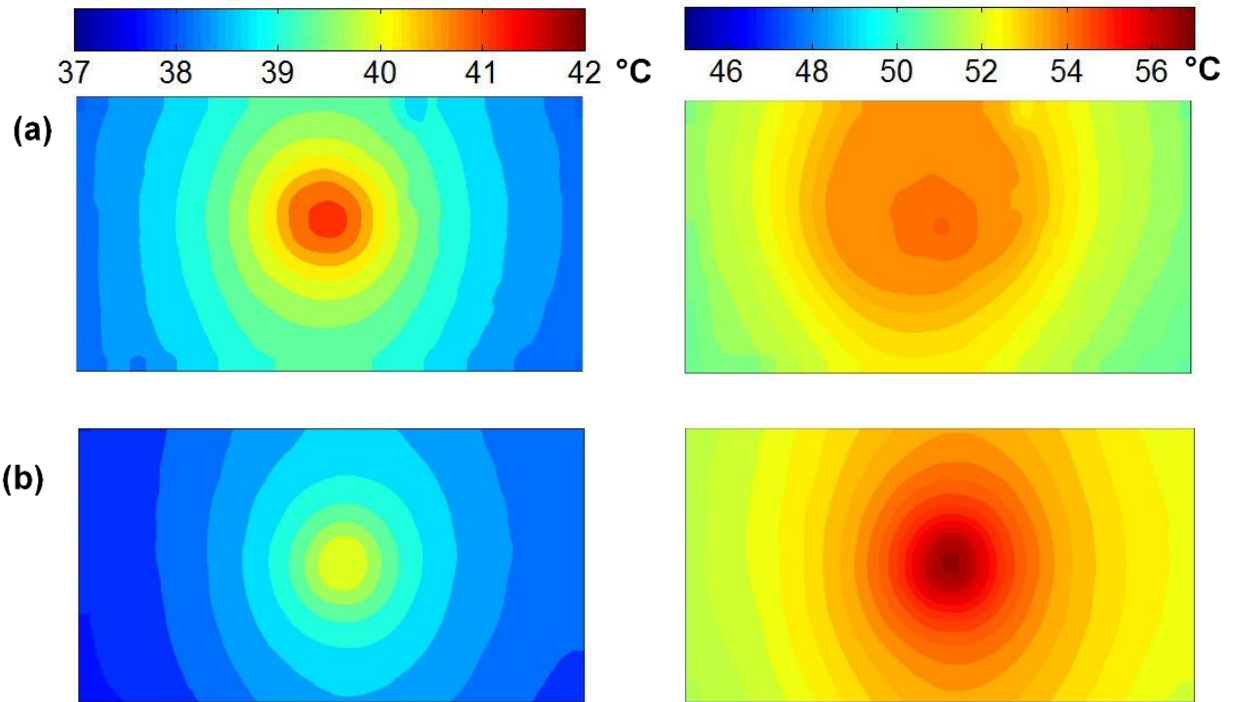


Figure 3.7. Contours of the condenser-side surface temperature for the (a) vapor chamber and (b) solid copper spreader at device heat inputs of approximately 1 W (left) and 2 W (right). Note the different temperature scales.

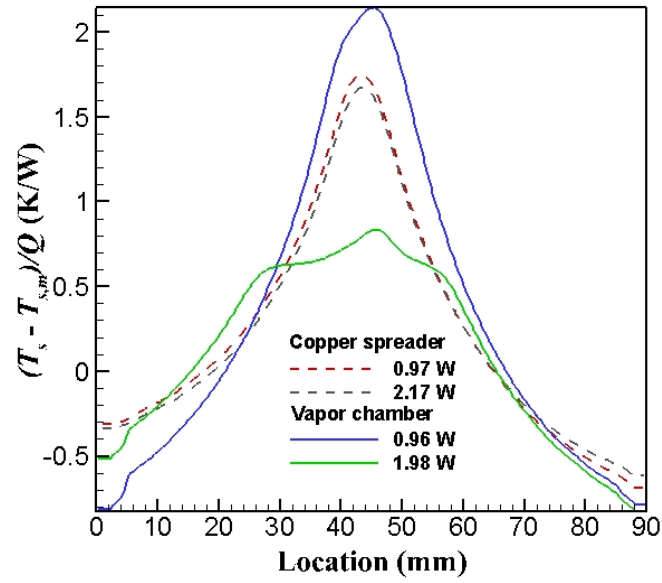


Figure 3.8. Condenser-side surface temperature difference from the mean, normalized by the device power (profile drawn along the length of the device passing through the center).

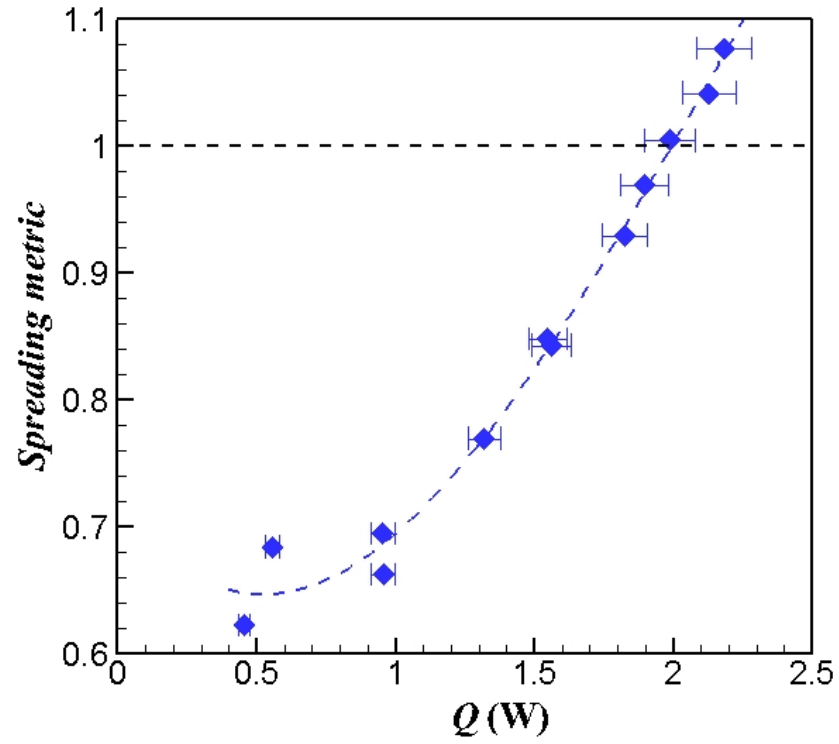


Figure 3.9. Spreading metric for the prototype vapor chamber relative to the solid copper heat spreader as a function of device heat input.

4. PATTERNING THE CONDENSER-SIDE WICK IN ULTRA-THIN VAPOR CHAMBER HEAT SPREADERS TO IMPROVE SKIN TEMPERATURE UNIFORMITY OF MOBILE DEVICES

This chapter focuses on the design of ultra-thin vapor chambers for improved condenser-surface temperature uniformity, targeting the mobile electronic device platform. A 3D numerical vapor chamber transport model is utilized to analyze the proposed vapor chamber wick domain layouts. The enhanced temperature uniformity produced by different candidate condenser-side wick designs are compared against a baseline design having a homogeneous, uniform wick layer. The material from this chapter was published in the *International Journal of Heat and Mass Transfer* [41].

4.1 Modeling Approach

4.1.1 Numerical Vapor Chamber Transport Model

The numerical modeling methodology used in the current work is adapted from Vadakkan et al. [24] and was previously validated against experimental data by Ranjan et al. [42]. The model solves the governing continuity and momentum equations in the wick and vapor core, and the energy equation in the wall, wick, and vapor core of the vapor chamber. The continuity equation is

$$\varphi \frac{\partial \rho}{\partial t} + \nabla \cdot (\rho V) = 0 \quad (4.1)$$

in which the $\partial \rho / \partial t$ term accounts for the mass addition and depletion in the wick and vapor core, and φ is the porosity of the zone with $\varphi = 1$ in the vapor core. The momentum equations are

$$\frac{\partial \rho u}{\partial t} + \nabla \cdot (\rho V u) = -\frac{\partial \varphi P}{\partial x} + \nabla \cdot (\mu \nabla u) - \frac{\mu \varphi}{K} u - \frac{C_E \varphi}{K^{1/2}} \rho |V| u \quad (4.2)$$

$$\frac{\partial \rho v}{\partial t} + \nabla \cdot (\rho V v) = -\frac{\partial \varphi P}{\partial y} + \nabla \cdot (\mu \nabla v) - \frac{\mu \varphi}{K} v - \frac{C_E \varphi}{K^{1/2}} \rho |V| v \quad (4.3)$$

$$\frac{\partial \rho w}{\partial t} + \nabla \cdot (\rho V w) = -\frac{\partial \phi P}{\partial z} + \nabla \cdot (\mu \nabla w) - \frac{\mu \phi}{K} w - \frac{C_E \phi}{K^{1/2}} \rho |V| w \quad (4.4)$$

in which K is the permeability of the zone. In the vapor core, $K = \infty$. The third and fourth terms in the momentum equations represent the Brinkman–Forchheimer extended Darcy model. The energy equation is

$$\frac{\partial (\rho C) T}{\partial t} + \nabla \cdot [(\rho C) V T] = \nabla \cdot (k_{eff} \nabla T) \quad (4.5)$$

in which (ρC) assumes different values in different zones: in the wall $(\rho C) = (\rho C)_{solid}$, in the wick $(\rho C) = \phi(\rho C)_{liquid} + (1 - \phi)(\rho C)_{solid}$, and in the vapor core $(\rho C) = (\rho C)_{vapor}$.

At the wick–vapor interface, an energy balance that accounts for conduction, convection, and phase change is applied to obtain the interface temperature T_i :

$$-k_{wick} A_i + m_i C_{liquid} T_i = -k_{vapor} A_i + m_i C_{vapor} T_i + m_i h_{fg} \quad (4.6)$$

in which a negative value of m_i indicates evaporation while a positive value indicates condensation. The Clausius-Clapeyron relation yields the interface pressure P_i , using some arbitrary reference pressure and temperature (P_0, T_0) :

$$\frac{R}{h_{fg}} \ln \left(\frac{P_i}{P_0} \right) = \frac{1}{T_0} - \frac{1}{T_i} \quad (4.7)$$

The evaporation/condensation mass flux at the interface is computed using a relation (Schrage [43]) based on kinetic theory of gases:

$$m_i'' = \left(\frac{2\sigma}{2 - \sigma} \right) \left(\frac{1}{(2\pi R)^{1/2}} \right) \left(\frac{P_{vapor}}{T_{vapor}^{1/2}} - \frac{P_i}{T_i^{1/2}} \right) \quad (4.8)$$

While the literature does not offer an established theoretical value for the accommodation coefficient (a wide range of experimental and theoretical values have been reported [44]), σ is chosen to be 0.03 for the current work. It is noted for the current work that the temperature difference at the wick–vapor interface is negligible compared to the overall temperature difference in the vapor chamber; the value of the accommodation coefficient chosen therefore does not affect the primary conclusions. The evaporation/condensation process connects the vapor core and wick

domains. The vapor phase density change caused by pressurization due to heating is computed using the ideal gas law. All flows are assumed laminar and incompressible. The wick is assumed to be always saturated, and the change in the liquid mass by evaporation or condensation is taken into account by adjusting the density (while keeping the volume constant), rather than by tracking the evolution of the liquid–vapor interface. A damping coefficient is used to under-relax the evaporation/condensation mass and energy source/sink terms during convergence within a time step to suppress numerical instabilities.

The governing equations are solved using the commercial finite-volume software FLUENT [40]; the interfacial transport equations are implemented using an additional script (termed as a user defined function). The PISO algorithm is used for pressure–velocity coupling, which allows use of larger time-steps in the transient solution. First-order discretization is used for the continuity and momentum equations (for numerical stability), while the energy equation uses second-order discretization. The transient formulation is first-order implicit.

4.1.2 Steady-State-Seeking Solution Algorithm

The numerical model has an inherently high computational cost. Thermophysical vapor properties and the evaporation/condensation mass flux are sensitive to temperature; thus, the hydrodynamics are coupled to the energy transport. In addition, the energy and mass source terms associated with phase change are damped for numerical stability. These factors increase the computational cost for iterative solvers. The cost is exacerbated by the extreme geometric aspect ratios to be investigated for mobile electronics, which require a high cell count in the computational mesh. A steady-state-seeking solution algorithm is developed to facilitate tractable simulation of the geometries investigated herein.

The model is inherently transient and the thermal performance metrics of interest to the current study are obtained by simulating in time until steady-state conditions are achieved. Given that the transient path is not of direct interest, the computational cost can be reduced by minimizing the number of time steps required to reach the steady-state conditions. This is achieved by forecasting the variable values for every cell in the mesh; a linear extrapolation (forward in time) is performed based on the values of each variable at consecutive transient time steps. This extrapolation process jumps to a solution that is closer to steady state without actually going through the physical transient path. It is noted that the intermediate faux-transient solutions obtained from such

extrapolations do not represent the actual transient behavior. After multiple such extrapolations, the solution tends to the physical steady state. The steady-state-seeking algorithm is implemented as follows:

1. Initialize variables: velocities are set to zero in the domain and the global temperature is set to an average of the condenser surface, computed using $Q = h \cdot A_s \cdot (T_{s,m} - T_{amb})$.
2. Run the simulation for n_t transient time steps.
3. Linearly extrapolate the flow variables (ρ, u, v, w, T) in each cell using the last two transient data points with an extrapolation coefficient n such that $T_{new} = n \cdot (T_1 - T_0) + T_1$.
4. Set the variable values to the extrapolated solution.
5. Repeat steps 2-4 until the solution converges to steady state.

Controls need to be applied for the choice of values n_t and n to ensure efficient convergence to steady state. The mean evaporator temperature over the area of heat input is used as the primary control variable. The mean evaporator temperature will always be higher than the initialized value of the mean condenser surface temperature. After an extrapolation of the evaporator temperature toward steady-state conditions and away from the initialized value, it is observed that this evaporator temperature may regress back toward the initial guess value for a few subsequent transient steps. This behavior is expected due to the approximate nature of the linear extrapolation used to forecast the behavior of the nonlinear system. The value of n_t is chosen to ensure that there is a sufficient number of solution steps so that the evolution of the evaporator temperature continues toward the steady-state conditions before another extrapolation is made. The value of n directly affects simulation time. If the value is set too high, the evaporator temperature jumps beyond the steady-state value (unknown *a priori*); this significantly extends the simulation time as the algorithm becomes inactive while the temperature reverts to the ultimate steady-state value. An overly low value of n would increase the number of extrapolation steps in the algorithm and thus also increase the simulation time. The value of n depends on the individual case being simulated, and an intermediate value that minimizes the simulation time is chosen heuristically. Because the various solutions steps do not lie on the actual transient solution, typical methods of tracking steady-state conditions (*e.g.*, change in temperature at key locations) cannot be used. In this case, therefore, the difference between the input power at the evaporator and the condenser is

tracked. Steady state is considered to be reached when this difference reaches 0.1% of the constant input power.

The algorithm is demonstrated using a 2D vapor chamber geometry for which obtaining the full transient simulation is computationally feasible for comparison. The 2D geometry and case details (Figure 4.1) are taken from Ref. [25]. The external dimensions are 30 mm \times 3 mm, with a uniform copper wall thickness of 0.25 mm and a uniform wick thickness of 0.2 mm; the wick has porosity, permeability, and effective conductivity of 0.56, 2.97×10^{-11} m², and 40 W/mK, respectively. The evaporator (heat input of 10 W/m²) is on one flat side, with a width of 5 mm, while the entire area of the opposing flat side is the condenser (convection coefficient of 400 W/m²K and ambient temperature of 298 K). The side walls are adiabatic. The working fluid is water. The numerical mesh has \sim 16,000 rectilinear cells with aspect ratios of \sim 1. Figure 4.2 compares the evaporator mean temperature and the evaporator-to-condenser power difference along the solution path for simulations with and without the steady-state-seeking solution algorithm implemented. For this case, the algorithm uses a value of 50 for the extrapolation coefficient n . In Figure 4.2a, it can be seen that the simulation proceeds towards the steady state much faster with the algorithm implemented due to the intermediate extrapolations in the solution. The inset in Figure 4.2a shows the jumps in the evaporator temperature for each extrapolation. It can also be seen, for some cases, that after the jump, the evaporator temperature deviates from the steady state. Hence the algorithm does not extrapolate till the evaporator temperature evolves toward the steady state (*i.e.*, away from the initial guess value). Figure 4.2b shows the evaporator-to-condenser power difference along the solution path, which is tracked for confirming steady state. The algorithm reduces the required number of solution steps from 700 to 37, representing an order-of-magnitude reduction in the computational cost.

The computational cost reduction offered by the steady-state-seeking solution algorithm allows for tractable simulation of high-aspect-ratio 3D vapor chamber geometries. The algorithm is implemented for all subsequent 3D simulations discussed in this work. The 3D simulations were performed using 16-core parallel processing (two 8-core Intel Xeon-E5 with 32 GB memory) to achieve a simulation time for each case on the order of one day.

4.2 Design Objective

The heat spreading performance of ultra-thin vapor chambers with boundary conditions that simulate the cooling of a mobile electronics device is investigated. The vapor chamber is used to spread heat from a local source to a condenser side close to the surface of the device, where heat is rejected by natural convection. Any ergonomics-based thermal performance metric, used to assess vapor chamber designs, would be governed by the condenser-side surface temperatures. The temperature distributions illustrated in Figure 4.3 are a schematic representation of temperatures along a rake on the condenser-side surface of a thin vapor chamber under the boundary conditions of interest (informed by experimental observations in Patankar *et al.* [45]). It is important to note that the area-averaged temperature on the condenser surface is independent of the vapor chamber design: for a constant power input and convective boundary conditions, the mean condenser-surface temperature is fixed as $T_{s,m} = Q / hA + T_{amb}$. While natural convection coefficients would vary with the local surface temperature, a constant value has been assumed for the current work due to the relatively small variations in temperature across the surface. The ideal flat profile at the mean temperature shown in Figure 4.3 can only be achieved if the vapor chamber has no lateral thermal resistance (*i.e.*, if heat could spread laterally without a temperature difference); this profile yields the minimum peak (condenser-surface) temperature. Thus, the objective of vapor chamber designs for ergonomics-driven mobile devices is to minimize the condenser-side peak-to-mean temperature difference, which is equivalent to obtaining the flattest possible temperature profile. In the current work, the effectiveness of designs (compared at identical boundary conditions) is based on this metric of the peak-to-mean temperature difference on the condenser-side surface.

4.3 Results and Discussion

A disc-shaped vapor chamber is considered so as to exploit axial symmetry to simplify the simulation domains, and thus maintain a low computational cost (Figure 4.4a). The disc has a radius of 45 mm and thickness of 0.5 mm. On the evaporator side, the vapor chamber receives heat input over a central circular area with radius of 5 mm. The opposite condenser-side face of the vapor chamber is exposed to a heat transfer coefficient representative of natural convection to the ambient ($h = 30 \text{ W/m}^2\text{K}$ and $T_{amb} = 298.15 \text{ K}$). The operating power is fixed at 5 W.

When designing the internal configuration of the wall, wick, and vapor space in a vapor chamber, the approach here assumes that the external envelope defined above is fixed. The copper wall thickness is held constant at 0.2 mm; in practice, the wall thickness would be selected for structural integrity at the vapor core pressure (determined based on the working fluid and operating temperature). The working fluid used is water. Thus, the flexibility for design enhancements lies in modifying the layout of the wick and vapor domains within the remaining 100 μm of allotted thickness. The current work assumes that the wick is composed of sintered copper powder with 60% open porosity and an effective conductivity of 40 W/mK. The permeability is computed using the relation $\varphi^3 d^2 / 150(1-\varphi)^2$, where d is the particle diameter and φ is the porosity. The wick thickness is ensured to be at least 3 times the particle diameter.

Due to the high aspect ratio of the geometry, an orthogonal meshing scheme is used to avoid highly skewed cells. There are three cells across the wick thickness, ten across the vapor core, and five across the wall. The aspect ratio of the cells (lateral to normal direction) is highest in the vapor core (ranging from 15 to 20, depending on the case).

4.3.1 Baseline Wick Domain Design

The baseline design considered is a monolithic wick layer of constant thickness on all internal surfaces of the vapor chamber (Figure 4.4b and c). The baseline case has a wick thickness of 30 μm composed of 7 μm -diameter copper particles. This minimum possible wick thickness is chosen such that the wick can just support the pressure drop in the system by capillary pressure at the 5 W of heat input; a factor of safety of 2 is used (*i.e.*, the capillary pressure in the wick is twice the total pressure drop in the wick and the vapor core). A minimized wick thickness yields the maximum possible vapor core cross-sectional flow area to minimize the lateral heat spreading resistance. The saturation temperature gradient in the radial direction in the vapor-core is proportional to the pressure drop. A higher cross-sectional flow area reduces the pressure drop, and hence the lateral temperature drop in the vapor-core, reducing the lateral heat spreading resistance. The axisymmetric baseline case was simulated using the numerical model. The results from the simulation are shown in Figure 4.5 and Figure 4.6; Figure 4.5 shows contour plots of the field variables on the axisymmetric plane and Figure 4.6 shows extracted profiles at key locations.

Interrogation of the thermal and hydrodynamic behavior of the baseline case helps understand the limiting transport mechanisms that can be targeted by design modifications. Figure 4.5a shows

the temperature field in the vapor chamber. The maximum temperature occurs at the centroid of the heat input. The temperature difference across the thickness is much lower than across the lateral extent. The conduction thermal resistances across the wall and wick are comparatively low due to their small thicknesses. Conversely, the thin vapor core induces a high lateral pressure drop and saturation temperature gradient, leading to the relatively larger lateral temperature variation observed. Figure 4.5b shows the velocity magnitude in the wick. On the condenser side, the velocity magnitude increases in the outward radial direction in the zone directly above the evaporator; in this region, the amount of liquid flow rate added to the wick by condensation outweighs the increasing area for flow. At regions further away from the center, where the condensation flux is reduced, the outward radial velocity decreases as the flow area increases. A complementary trend is observed in the evaporator wick: in regions beyond the active heat input zone where liquid loss due to evaporation is low, the velocity magnitude increases as the central axis is approached because the flow area decreases. Once in the heated evaporator region, however, the inward radial velocity decreases as the amount of liquid flow in the wick is drastically reduced due to evaporative loss. The pressure field in the wick is shown in Figure 4.5c; the pressure gradient is clearly proportional to the velocity magnitude in the wick. Figure 4.5d show the contours of velocity in the vapor core. It can be seen that the velocity magnitude is zero at the axis, and increases sharply in the radial direction to a high value till the maximum radius of the heat input. Outside the heat input region, the velocity magnitude reduces drastically in the outward radial direction. This is caused by the increasing area for vapor flow and by condensation, both of which reduce the vapor mass flux in the outward direction. This gradient of velocity is proportional to the pressure gradient in the vapor core (see the pressure field in Figure 4.5e).

Figure 4.6a plots the radial variation of temperature on the condenser-side surface. The shape of this temperature profile is identical to the local heat flux leaving the condenser surface (see right vertical axis of Figure 4.6a) due to the assumption of a constant heat transfer coefficient to a constant-temperature ambient. This heat flux profile is indicative of the relative thermal resistance from the evaporator to each location on the condenser surface. For example, consider two heat flow paths, one passing through the center of the condenser surface and the other near the outer circumference. Near the center, heat must only conduct across the walls and wicks; there is a higher thermal resistance to heat passing through the peripheral path due to the saturation temperature gradient in the vapor core. Thus the condenser-surface heat flux and temperature are higher near

the center. In order to improve the temperature uniformity on the condenser surface, the resistances along these pathways must be equalized, either by (1) reducing the vapor-core thermal resistance or (2) increasing the condenser-side wall and wick conduction resistances near the center of the vapor chamber. The following sections demonstrate how these thermal resistances may be manipulated by modifying the layout of the condenser-side wick in order to achieve improved condenser-surface temperature uniformity.

It is important to note that the capillary pressure ($P_{cap} = 2\gamma/(0.21d)$) driving the liquid from the condenser to the evaporator through the wick is the maximum possible pressure drop in the wick. The pressure drop in the wick in this baseline design (Figure 4.6b) is half of the capillary pressure (since a factor of safety of 2 is used as mentioned earlier). Modified condenser-side wick designs that lead to a wick pressure drop that is lower than 50% of the capillary pressure would indicate that the vapor chamber can operate at a lower wick thickness, allowing an increase in the vapor-core thickness and reduction in the lateral thermal resistance.

The heat flux at the condenser-side wick–vapor interface (proportional to the mass flux due to condensation) is plotted in Figure 4.6c. Similar to the condenser surface, the heat flux is high near the center and lower at the periphery. It is noted that the net heat transport rate across the wick–vapor interface is the same as that across the condenser outer surface. This heat flux is useful to track because the profile is more sensitive to modifications of the condenser-side wick compared to the condenser outer surface where the profile is smeared due to conduction in the condenser wall.

4.3.2 Grooved Condenser Wick Domain Design

Two potential approaches were identified in Section 4.3.1 for achieving a more uniform condenser-side surface temperature: (1) increasing the thermal conduction resistance in the central region of the condenser-side wall and wick, and (2) reducing the vapor core thermal resistance. One way to achieve both effects is to eliminate parts of the wick layer in the central condenser region. This would locally reduce the effective thermal conductivity of the wick in this region by replacing the porous sintered copper with a layer of lower-conductivity liquid (*viz.*, water). In addition, the effective permeability (of the sintered copper wick and the grooves) would increase, which would allow for a thinner wick over the entire condenser side inner wall while maintaining the same pressure drop, and hence reduce the vapor-core thermal resistance. This section explores

the potential improvement in temperature uniformity that may be achieved with such a design modification, and the relative benefits of the two mechanisms.

A wick design is evaluated that excises part of the wick material on the condenser side in the region $r < 10$ mm. This region is targeted because of the comparatively high heat flux it experiences before a steep drop-off outside this zone, as shown in Figure 4.6c. The design consists of radial patterned grooves in the condenser-side wick, as represented in Figure 4.4d. For this hypothetical case, the pattern has 36 periodic units (of 10 deg each) in the azimuthal direction; in each unit, 90% of the wick area is removed. The resulting pattern looks like a spoked wheel. The grooved condenser wick design otherwise has the same materials and geometry as the baseline design, and the behavior was simulated using the same boundary conditions.

The simulated results are compared in Figure 4.7 to the baseline (uniform-wick) design. Figure 4.7c shows that the amount of condensation heat flux at the condenser-side wick-vapor interface in the central region ($r < 10$ mm) has reduced by a small fraction, which is reflected in the condenser-surface temperature profile (shown in Figure 4.7a). While the heat flux has a small sharp peak at $r = 0$, this is smeared due to conduction in the condenser-side wall, and thus it does not have an adverse effect on the condenser-surface temperature profile. This indicates that the thermal resistance of the wick in the central region is increased, and the peak-to-mean temperature difference at the condenser surface has marginally reduced from 6.33 K for the baseline case to 5.96 K for the current design. Figure 4.7b shows the pressure distribution in the wick. It can be seen that the pressure gradient in the central region of the condenser wick has drastically reduced compared to the baseline case as a result of the increased effectively permeability to liquid flow.

The significant effect caused by a change in the effective wick permeability indicates that (1) it may be possible to achieve a significant reduction in the effective vapor core thermal resistance. In contrast, (2) a relatively small performance improvement is obtainable by increasing the condenser-side conduction resistance in the central region. Thus, a condenser-side wick design is explored in the next section that aims to maximize the benefit of increasing the condenser-side wick effective permeability.

4.3.3 Biporous Condenser-Side Wick Domain Design with Radially Discretized Grooves

As demonstrated in Section 4.3.2, the major advantage of a grooved condenser-side wick design lies in the reduced wick pressure drop rather than the increased thermal resistance in the

central region. Thus, this design approach need not be restricted to the central region ($r < 10$ mm), but instead can be extended to the full radius of the condenser-side wick. This extension would further reduce the wick pressure drop, allowing for an even thinner wick layer and lower vapor-core thermal resistance. However, the radial grooves cannot simply be extended from the center to the circumference of the condenser-side wick due to restrictions on the width of the grooves. In the grooves, vapor condenses onto the vapor chamber wall and forms a liquid pool with a meniscus connecting the neighboring strips of sintered copper, as illustrated in Figure 4.8. If a groove is too wide, the meniscus shape is stretched so that the liquid bridge between adjacent sintered copper strips is broken; condensing liquid may accumulate under these conditions and block the vapor flow. Thus, the width of the groove is limited to a maximum value.

Assuming a circular meniscus with a constant contact angle, a relation for the maximum groove width for a given wick thickness is obtained.

$$W_{\text{limit}} = \frac{2t_{\text{wick}} \cos(\theta)}{(1 - \sin(\theta))} \quad (4.9)$$

For a copper-water system with a contact angle of ~ 40 deg, this minimum width is of the order of $100 \mu\text{m}$. If a single groove were to extend from the center of the condenser-side wick to the circumference, where the maximum groove width is restricted to $100 \mu\text{m}$, this groove would need an impossibly small angle at the center. The strips of sintered copper wick between grooves must also adhere to a minimum width limit in order to accommodate 3 particle diameters.

These groove width limits are considered in the design of a biporous condenser-side wick with radially discretized grooves, as illustrated in Figure 4.9. The design has multiple sections, each having equal-length grooves in the radial direction. The number of grooves (and strips of sintered copper between the grooves) contained in each section can then increase for sections further away from the center. This strategy avoids nonviable groove angles at the center, while maintaining the width limits. The angle of the groove within each section is designed such that the groove reaches the width limit at the maximum radial location in that section. The angle of the sintered copper strips is determined such that their width is at the minimum limit at the minimum radial location in each section. This approach aims to minimize the wick pressure drop. It should be noted that the design does not attempt to increase the thermal resistance of the condenser-side wick in the

central region, since the ancillary benefits of doing so are negligible. A small circular section in the center has no grooves based on the minimum possible sintered copper strip thickness.

The vapor chamber behavior was simulated with this biporous condenser-side wick design. To capture the complex geometry of the condenser-side wick domain, an effective permeability formulation was implemented (Appendix A). Using this formulation, the biporous wick design could be simulated as an axisymmetric geometry. A minimum wick thickness is required to minimize the lateral temperature difference in the vapor-core, while satisfying the capillary pressure constraint defined in Section 4.3.1. Hence, the wick thickness was reduced from 30 μm in the baseline case to 21 μm for the biporous wick design. For a design with nine discrete radial sections of 5 mm-long grooves (except for the innermost section, which has 2.5 mm-long grooves), the approach described above resulted in a condenser-side wick with 240, 480, 786, 1080, 1372, 1662, 1951, 2240, and 2529 grooves in each of the radial sections; the central region without grooves has a radius of 2.5 mm. Other than the reduced wick thickness and biporous condenser-side wick design, the rest of the geometry and boundary conditions were the same as the baseline case.

The simulation results comparing the biporous and baseline wick designs are shown in Figure 4.10. Figure 4.10b shows the pressure in the wick; the pressure gradient in the condenser-side wick is much lower for the biporous wick design. The thinner biporous wick results in lowered vapor core thermal resistance, leading to a more uniform temperature profile on the condenser surface. This is reflected in the redistribution of heat flux due to condensation at the wick-vapor interface (Figure 4.10c). The condenser-surface temperature profile shows a reduction in the peak temperature when compared to the baseline case of 2.33 K (Figure 4.10a). The peak-to-mean temperature was reduced from 6.33 K to 4 K due with the biporous wick design, a 37% improvement.

4.4 Conclusions

The performance-enhancement strategies developed in this work provide a pathway for effectively introducing vapor chambers into mobile devices for thermal management. In mobile cooling applications, the ultra-thin form factor, low heat input power, and heat rejection to the ambient by natural convection -- which define the performance-governing transport mechanisms -- have limited the viability of vapor chambers designed using conventional performance metrics.

The design approach under such conditions must shift focus away from the traditional objective of reducing the chip/evaporator temperature and instead target improved condenser-surface temperature uniformity, where the effectiveness of the heat spreader directly affects user comfort in mobile platforms.

The design process used a three-dimensional numerical vapor chamber transport model to evaluate various geometries at a high fidelity. The computational cost issues associated with using this numerical model at ultra-thin form factor geometries were identified, and a cost-reducing steady-state-seeking solution algorithm was developed and implemented. This algorithm allowed for an order-of-magnitude reduction in the computational cost.

It was concluded that condenser-surface temperature uniformity is governed by the layout of the condenser-side wick; uniformity can be improved by (1) increasing thermal resistance across the condenser-side wick in the heat input region, and (2) increasing condenser-side wick permeability in order to reduce its thickness, and thereby increase the vapor-core thickness for lowered lateral thermal resistance. A hypothetical design implementing these two strategies was simulated and revealed that the second strategy can yield significant improvement in the condenser-surface temperature uniformity. A biporous condenser-side wick design was developed on this principle; numerical simulations comparing the baseline and biporous condenser-side wick designs showed that the peak-to-mean condenser surface temperature difference of the vapor chamber could be reduced by up to 37%. The approach developed in this work can be adopted to produce vapor chamber wick designs in coordination with practical fabrication constraints.

Nomenclature

V	velocity [m s^{-1}]
x, y, z	Cartesian coordinates [m]
r	radius [m]
u	x -velocity [m s^{-1}]
u_{eff}	effective x -velocity [m s^{-1}]
v	y -velocity [m s^{-1}]
w	z -velocity [m s^{-1}]
P	pressure [Pa]
P_{cap}	capillary pressure [Pa]
K	permeability [m^2]
K_{eff}	effective permeability [m^2]
C_E	Ergun's coefficient [–]
T	temperature [K]
C	specific heat capacity [$\text{J kg}^{-1} \text{K}^{-1}$]
k	thermal conductivity [$\text{W m}^{-1} \text{K}^{-1}$]
k_{eff}	effective thermal conductivity [$\text{W m}^{-1} \text{K}^{-1}$]
h_{fg}	enthalpy of vaporization [J kg^{-1}]
A	area [m^2]
m	mass flow rate [kg s^{-1}]
R	gas constant [$\text{J kg}^{-1} \text{K}^{-1}$]
Q	power (rate of heat flow) [W]
h	convection coefficient [$\text{W m}^{-2} \text{K}$]
t_{wick}	wick thickness [m]
W	groove width [μm]
n	extrapolation coefficient [–]
n_t	number of transient steps between extrapolations [–]
d	sintered copper particle diameter [m]

Greek symbols

ρ	density [kg m^{-3}]
ϕ	porosity [–]
μ	dynamic viscosity [Pa s]

σ	accommodation coefficient [-]
γ	surface tension [N m ⁻¹]

Subscripts

<i>i</i>	wick–vapor interface
<i>0</i>	reference
<i>solid</i>	solid properties
<i>liquid</i>	liquid properties
<i>vapor</i>	vapor properties
<i>wick</i>	wick properties
<i>s</i>	condenser surface
<i>m</i>	mean
<i>amb</i>	ambient

Superscripts

"	per unit area
---	---------------

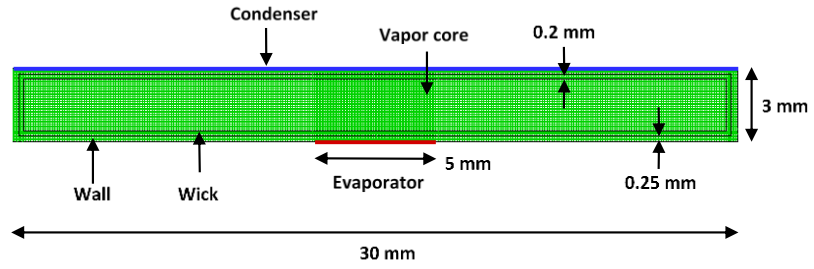
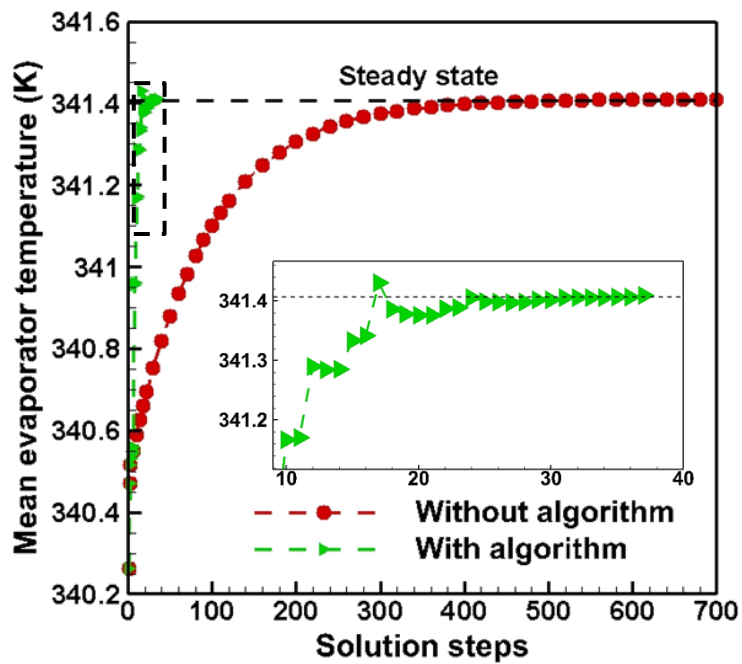
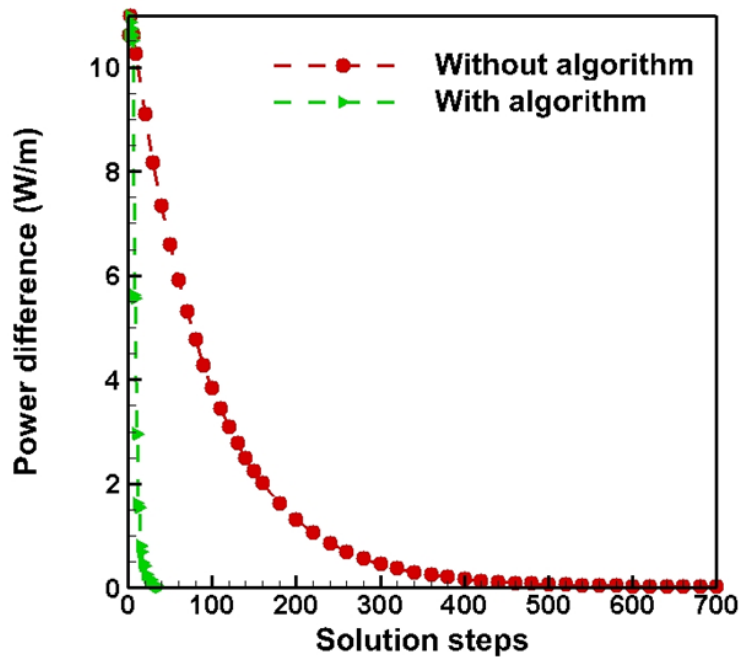


Figure 4.1. 2D vapor chamber geometry and mesh details for example case used to verify the behavior and effectiveness of the steady-state-seeking solution algorithm.



(a)



(b)

Figure 4.2. Progression of the (a) mean evaporator temperature (inset shows dashed region at the top left) and (b) evaporator-to-condenser power difference with solution steps for the full transient simulation and with the steady-state-seeking solution algorithm implemented.

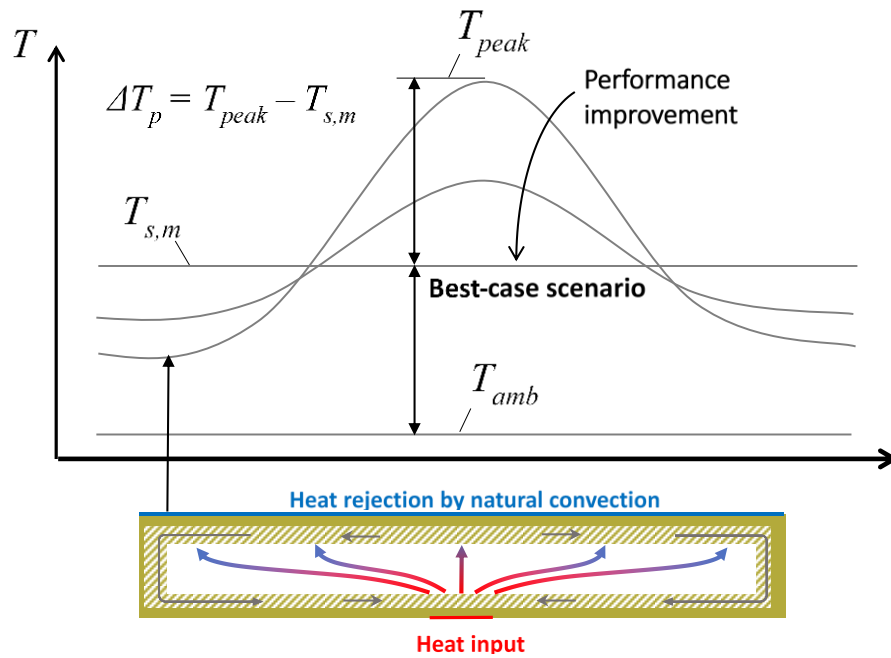


Figure 4.3. Schematic representation of vapor chamber condenser-surface temperature profile (inset shows the boundary conditions). Performance improvement is measured as a reduction of the peak-to-mean surface temperature.

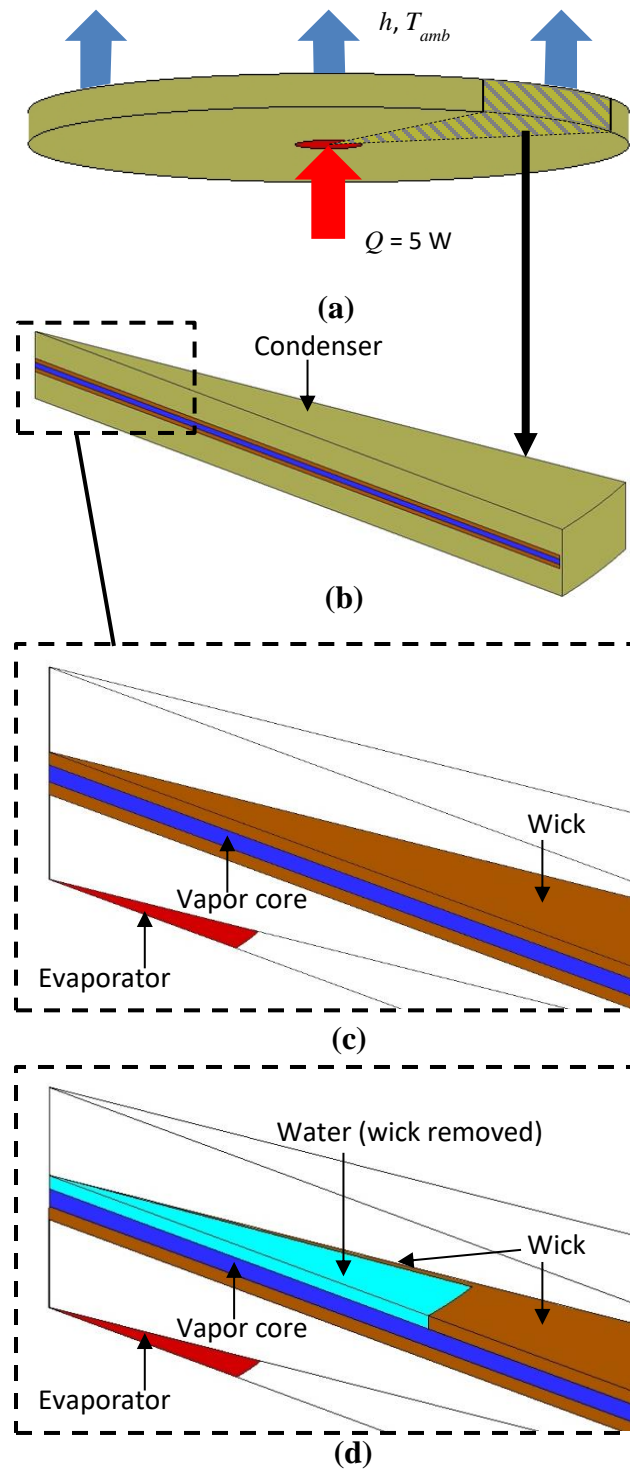


Figure 4.4. (a) Geometry and boundary conditions for the baseline design of the vapor chamber and (b) an axisymmetric section showing internal layout of the wick and vapor domains. Magnified details of the wick and vapor layout for (c) baseline case and (d) grooved condenser wick domain design.

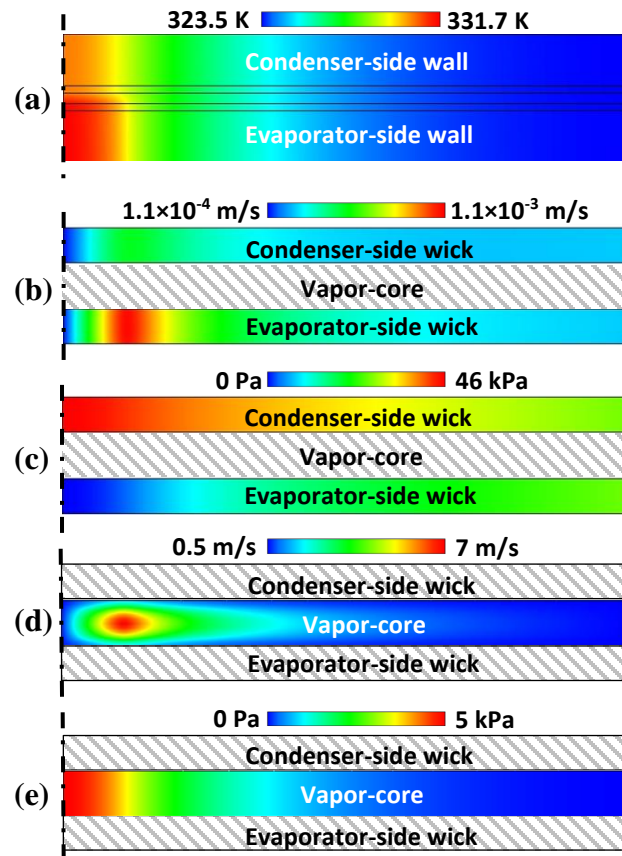
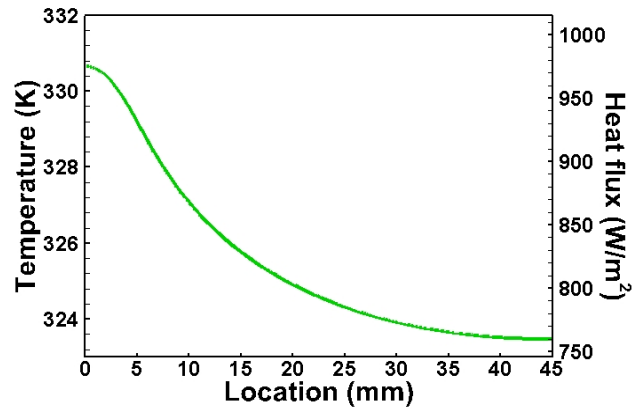
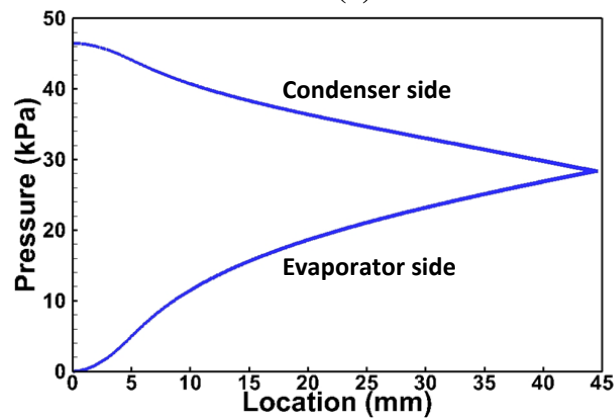


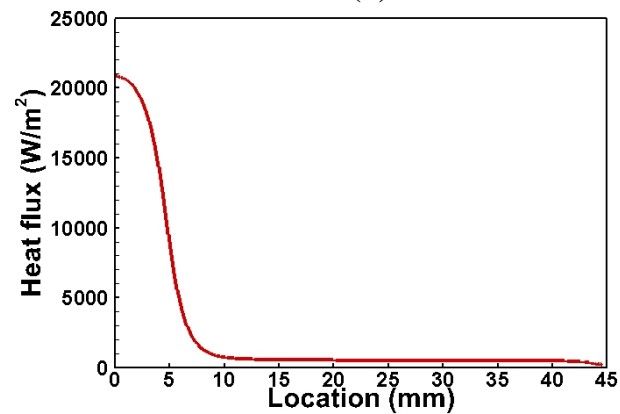
Figure 4.5. Results for the baseline, uniformly distributed wick case: contours of (a) temperature (dimensions in the plot are scaled by $20\times$ along the thickness), (b) velocity magnitude in the wick, (c) pressure in the wick, (d) velocity in the vapor core, (e) pressure in the vapor core (parts (b) through (e) are scaled by $90\times$ along the thickness relative to the radius).



(a)



(b)



(c)

Figure 4.6. Results for the baseline, uniformly distributed wick case: plots of the radial distribution of (a) temperature and heat flux on the outer condenser-side surface, (b) pressure in the wick, and (c) heat flux due to condensation at the condenser-side wick-vapor interface.

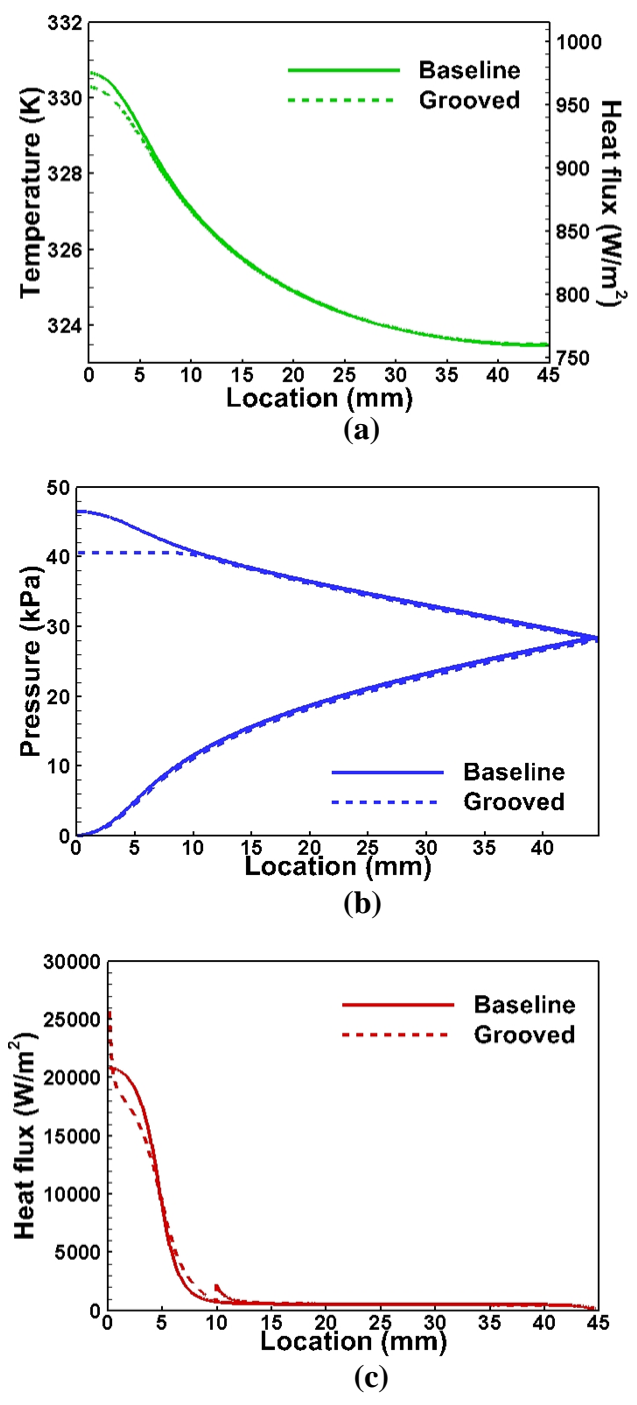


Figure 4.7. Results for the case with the grooved condenser-side wick domain design: plots of the radial distribution of (a) temperature and heat flux on the outer condenser-side surface, (b) pressure in the wick, and (c) heat flux due to condensation at the condenser-side wick-vapor interface.

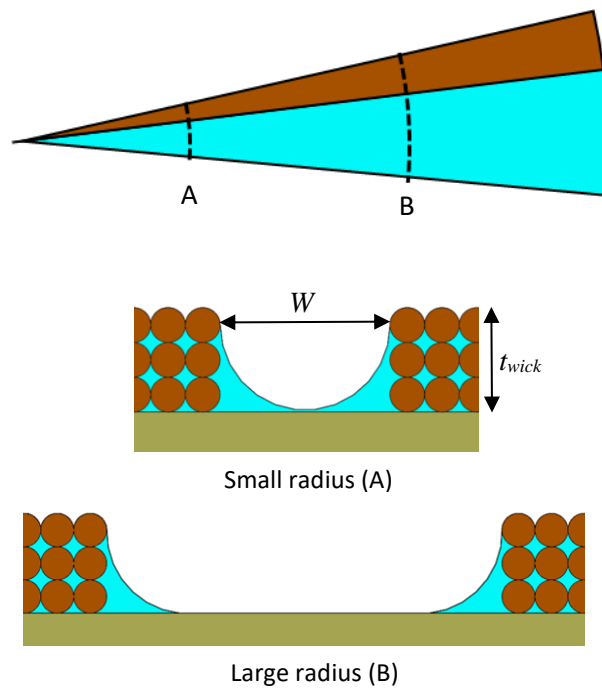


Figure 4.8. Illustration of the groove width restriction.

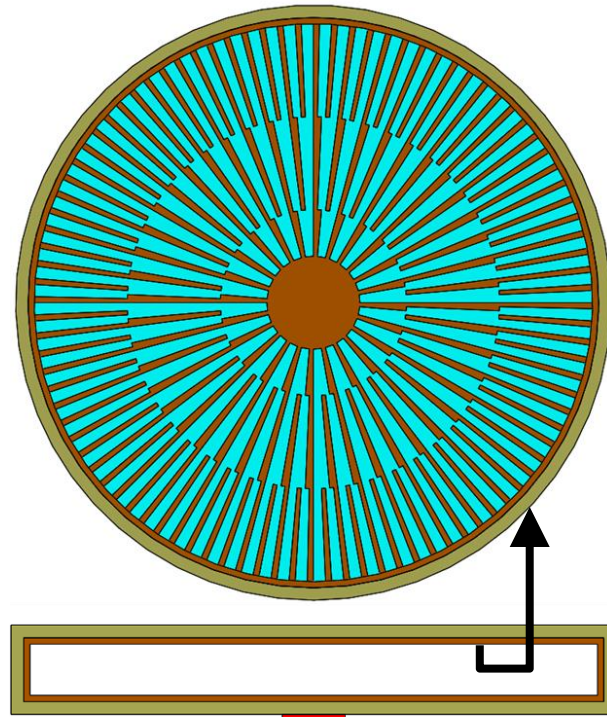
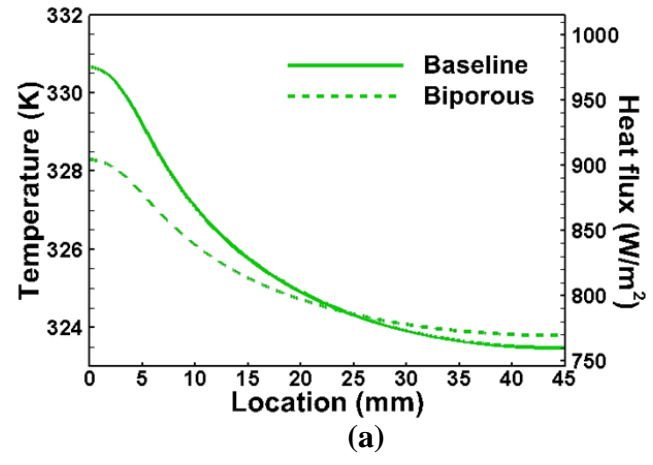
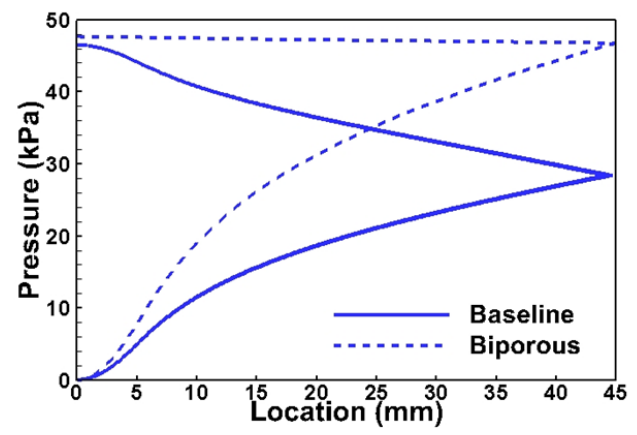


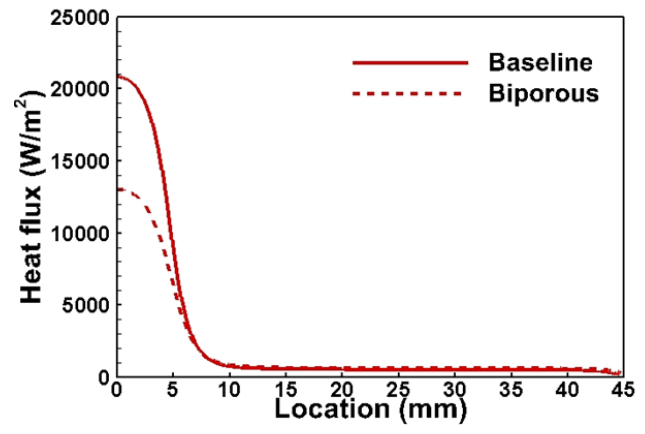
Figure 4.9. Illustration of the biporous condenser-side wick domain design with radially discrete grooves. The illustration is shown for a wick with three radial sections; the geometry details are not shown to scale.



(a)



(b)



(c)

Figure 4.10. Results for the case with the biporous condenser-side wick domain design: plots of the radial distribution of (a) temperature and heat flux on the outer condenser-side surface, (b) pressure in the wick, and (c) heat flux due to condensation at the condenser-side wick-vapor interface.

5. WORKING-FLUID SELECTION FOR MINIMIZED THERMAL RESISTANCE IN ULTRA-THIN VAPOR CHAMBERS

This chapter provides guidelines for the process of choosing a working fluid that yields the minimum thermal resistance for ultra-thin vapor chambers, which go beyond the more simplistic existing figures of merit. An analytical expression is developed for the effective resistance of an ultra-thin vapor chamber of axisymmetric geometry. Based on the expression, the significance of the existing individual figures of merit is discussed at the operational extremes. An approach is demonstrated for choosing the working fluid for any operating and geometric parameters, utilizing the complete analytical expression. The material in this chapter is published in the *International Journal of Heat and Mass Transfer* [46].

5.1 Model

A working fluid should be chosen to yield the best possible thermal performance, typically characterized in terms of the effective thermal resistance of the vapor chamber. A physics-based transport model for vapor chamber operation which predicts the effective thermal resistance is hence required to inform working fluid selection. To develop a standard practice for working fluid selection, the selection process in this work is based on a conventional thermal resistance network modeling approach [29]. This modeling approach divides the vapor chamber domain into a network of one-dimensional thermal resistances corresponding to conduction in the wall and wick, evaporation/condensation at the interfaces, and temperature drop in the vapor core. The performance of an ‘ultra-thin’ vapor chamber having negligible thermal resistance across the thickness of the wall and wick can be simply represented by the vapor core effective conductance, defined as

$$k_{vap} = \frac{Q}{\Delta T_{vap}}. \quad (5.1)$$

where ΔT_{vap} is the total saturation temperature change due to the pressure drop in the vapor core.

The geometry of the vapor chamber selected for demonstration of this fluid selection strategy is illustrated in Figure 5.1; this is representative of a typical internal layout in vapor chambers. The vapor chamber is disc-shaped with radius R . The evaporator is a circle of radius R_e at the center of

one face of the vapor chamber, with a power input Q . The entire opposing face acts as the condenser. The vapor chamber has walls of constant thickness. There is a uniform layer of wick (thickness t_{wick}) on internal surfaces of the chamber. A working thickness (t) is defined as the total thickness of the vapor core (t_{vap}) plus the two wick layers on each side ($2 \times t_{wick}$). The total working thickness is assumed to have a constant value (based on space constraints), but the relative thicknesses occupied by the wick and vapor core are allowed to vary.

The model is used to assess the effect of fluid properties on vapor chamber performance in two steps. (1) As a design premise, the wick thickness should be minimized to enable the largest vapor core thickness possible; a required minimum wick thickness is computed based on the capillary limit at power Q for each fluid. (2) The second step is computing the vapor core effective conductance for each respective vapor core thickness, and use it to compare and assess fluids. The primary objective of the current modeling approach is to obtain a simple analytical relationship (rather than a high-fidelity prediction) for the vapor core effective conductance that is a function of the fluid properties, vapor chamber geometry, and operating power. The same fluid selection approach presented here could be applied using alternative, high-fidelity model frameworks [25, 47].

5.1.1 Design for Minimized Wick Thickness

For a vapor chamber to operate, the capillary pressure driving the fluid flow must be larger than the pressure drop. To design for the minimum required wick thickness, the capillary pressure is equated to the pressure drop in the wick (*i.e.*, capillary limit at this minimum thickness). The pressure drop in the vapor core, although larger than conventional ‘thick’ vapor chambers, is still typically significantly less than the pressure drop in the wick for ultra-thin vapor chambers, and therefore is not considered. The capillary pressure in the wick is defined by

$$P_{cap} = \frac{2\gamma}{r_{eff}}; r_{eff} = m d_p, \quad (5.2)$$

where the effective pore radius (r_{eff}) is proportional to the particle diameter of the wick (d_p) with a proportionality constant of m . The pressure drop in the wick is computed using Darcy’s law for one-dimensional radial flow. This assumes that all of the pressure gradient in the porous wick structure is attributed to viscous drag based on the relation given by

$$\frac{dP_{wick}}{dr} = -\frac{\mu_l}{K} u_{r,wick}(r); u_{r,wick}(r) = \frac{\dot{m}_{wick}(r)}{\rho_l 2\pi r t_{wick}}. \quad (5.3)$$

The permeability of the wick can be expressed using the Carman-Kozeny relation, given by

$$K = \frac{d_p^2 \phi^3}{f(1-\phi)^2} = A d_p^2, \quad (5.4)$$

where f is an empirical factor depending on the wick morphology; the term A is introduced to simplify presentation of this expression in subsequent equations.

In the condenser-side wick, the outward liquid mass flow is supplied by condensation at the wick-vapor interface. We assume that the rate of condensation is uniform across the entire interface (constant mass flux across the interface) to obtain a simplified analytical expression for the mass flow rate:

$$\dot{m}_{wick}(r) = \frac{Q}{h_{fg}} \left(\frac{r}{R} \right)^2. \quad (5.5)$$

In the evaporator-side wick, it is assumed that mass flow is reduced by uniform evaporation over the heat input area ($0 < r < R_e$). Hence, the mass flow rate is expressed as:

$$\begin{aligned} \dot{m}_{wick}(r) &= -\frac{Q}{h_{fg}} \quad \text{for } r > R_e \\ \dot{m}_{wick}(r) &= -\left(\frac{Q}{h_{fg}} - \frac{Q}{h_{fg}} \left(1 - \left(\frac{r}{R_e} \right)^2 \right) \right) \quad \text{for } r < R_e \end{aligned} \quad (5.6)$$

Substituting the expressions for mass flow rate in Eqs. (5.5) and (5.6) into Eq. (5.3) and integrating yields the total pressure drop in the wick:

$$\Delta P_{wick} = \frac{\mu_l Q}{2\pi h_{fg} \rho_l t_{wick} A d_p^2} \left(\ln \left(\frac{R}{R_e} \right) + \frac{5}{8} \right). \quad (5.7)$$

The particle diameter is defined as a fixed fraction of the wick thickness ($d_p = t_{wick} / n$). A factor of safety F_s is introduced for the wick pressure drop, to avoid the certain failure if the capillary limit were reached:

$$P_{cap} = F_s \times \Delta P_{wick} . \quad (5.8)$$

This results in the following relation for minimum wick thickness

$$t_{wick} = \frac{1}{2} a_1 \left(\frac{Q}{M_l} \right)^{0.5} ; \quad M_l = \frac{\rho_l \gamma h_{fg}}{\mu_l} ; \quad a_1 = 2 \left(\frac{nmF_s}{4\pi A} \left(\ln \left(\frac{R}{R_e} \right) + \frac{5}{8} \right) \right)^{0.5} . \quad (5.9)$$

5.1.2 Expression for Vapor Core Effective Conductance as a Function of M_v

The temperature gradient in the vapor core is due to the saturation pressure gradient. The pressure gradient is computed using the steady-state fluid momentum transfer equation (cylindrical coordinates) in the radial direction. The following simplifying assumptions are used: (1) for $t_{vap} \ll R$, momentum diffusion predominantly occurs in the z -direction, (2) for $Re \left(\frac{t_{vap}}{R} \right)^2 \ll 1$ where

$Re = \frac{\rho_v U_r R}{\mu_v}$, convection is negligible compared to diffusion in the z -direction. The resulting equation is

$$\frac{dP_{vap}}{dr} = \mu \frac{d^2 u_{r,vap}}{dz_{vap}^2} . \quad (5.10)$$

Integrating twice along z gives the velocity profile

$$u_{r,vap} = -\frac{t_{vap}^2}{8\mu} \frac{dP_{vap}}{dr} \left(1 - \frac{4z_{vap}^2}{t_{vap}^2} \right) . \quad (5.11)$$

The mass flow rate in the vapor core is given by $\dot{m}_{vap}(r) = \int_{-t_{vap}/2}^{t_{vap}/2} \rho_v u_{r,vap} 2\pi r dz_{vap}$. Combining with Eq. (5.11) yields

$$\frac{dP_{vap}}{dr} = -\frac{6\mu_v \dot{m}_{vap}(r)}{\pi t_{vap}^3 r \rho_v} . \quad (5.12)$$

The vapor mass flow rate at any radial location is the difference between evaporation mass rate and condensation mass rate:

$$\begin{aligned} \dot{m}_{vap}(r) &= \frac{Q}{h_{fg}} \left(\frac{r^2}{R_e^2} - \frac{r^2}{R^2} \right) \quad \text{for } r < R_e \\ \dot{m}_{vap}(r) &= \frac{Q}{h_{fg}} \left(1 - \frac{r^2}{R^2} \right) \quad \text{for } r > R_e \end{aligned} \quad (5.13)$$

Substituting Eq. (5.13) into Eq. (5.12) and integrating over r gives the pressure drop in the vapor core as

$$\Delta P_{vap} = \frac{6\mu_v Q}{\pi t_{vap}^3 \rho_v h_{fg}} \ln \left(\frac{R}{R_e} \right). \quad (5.14)$$

The temperature difference in the vapor-core is obtained using the Clausius-Clapeyron relation

$$\Delta T_{vap} = \frac{R_g T_v^2}{P_v h_{fg}} \Delta P_{vap} = \frac{6R_g T_v^2 \mu_v Q}{P_v \pi t_{vap}^3 \rho_v h_{fg}^2} \ln \left(\frac{R}{R_e} \right) \quad (5.15)$$

where P_v and T_v are taken as the average vapor pressure and temperature. The ultimate performance of the vapor chamber is expressed by the effective vapor core conductance,

$$k_{vap} = \frac{Q}{\Delta T_{vap}} = a_2 M_v t_{vap}^3; \quad M_v = \frac{P_v \rho_v h_{fg}^2}{R_g T_v^2 \mu_v}; \quad a_2 = \frac{\pi}{6 \ln \left(\frac{R}{R_e} \right)}. \quad (5.16)$$

To obtain an expression based on the desired design parameter of the constraining working thickness t , substitute $t_{vap} = t - 2t_{wick}$ into Eq. (5.9) to get:

$$k_{vap} = a_2 M_v \left(t - a_1 \left(\frac{Q}{M_l} \right)^{0.5} \right)^3. \quad (5.17)$$

This model assumes that the vapor chamber thermal resistance is dominated by the vapor core resistance. The assumption is valid when the vapor core resistance is larger than all other primary resistances (*viz.*, the diffusive thermal resistance in the wick and the solid wall and the resistance due to phase change). A simple check of the model validity is provided by ensuring that the vapor-core conductance is significantly less than the evaporator wick conductance, according to

$$a_2 M_v \left(t - a_1 \left(\frac{Q}{M_l} \right)^{0.5} \right)^3 \ll \frac{k_{wick} \pi R_e^2}{\frac{1}{2} a_1 \left(\frac{Q}{M_l} \right)^{0.5}} \quad (5.18)$$

5.2 Results

The model developed above indicates that the vapor core effective conductance (Eq. (5.17)) increases with an increase in either of the conventional figures of merit that contain both liquid properties (M_l) and vapor properties (M_v). A candidate working fluid with higher values of both M_l and M_v can be deemed preferable without computing the vapor-core effective conductance. However, when comparing two fluids where the value of M_l is higher for one fluid but M_v is higher for the other (or *vice versa*), the appropriate choice can only be made by computing the vapor core effective conductance using Eq. (5.17). Thus, while figures of merit containing only fluid properties (M_l and M_v) are useful indicators in some instances, a generalized model for the vapor chamber thermal resistance is required for choosing the working fluid, as demonstrated below.

The vapor core effective conductance depends not only on the fluid property figures of merit, but also on different vapor chamber geometric parameters and operating conditions. This study analyzes the effects of three key parameters, namely operating power, working thickness, and operating temperature, on the vapor core conductance (and hence the choice of working fluid).

5.2.1 Effect of Operating Power and Working Thickness on the Choice of Working Fluid

The operating power has a significant effect on fluid choice. Consider the vapor core conductance in the limit of a very low operating power. Eq. (5.17) becomes

$$\{Q \rightarrow 0\} \Rightarrow \left\{ a_1 \left(\frac{Q}{M_l} \right)^{0.5} \rightarrow 0 \right\} \Rightarrow \{k_{vap} \rightarrow a_2 M_v t^3\}. \quad (5.19)$$

At a low operating power, a fluid with a high value of M_v is preferred; the value of M_l is less relevant. On the other hand, a high value of operating power implies

$$\left\{ t_{wick} = a_1 \left(\frac{Q}{M_l} \right)^{0.5} \right\} \rightarrow t, \quad (5.20)$$

i.e., the wick thickness will approach the limit where it must occupy the entire working thickness in order to convey liquid at the high operating power. Thus, to keep the value of wick thickness below the available working thickness, a working fluid with a high value of M_l is critical; the value of M_v is less relevant.

This influence of operating power is illustrated using three example fluids: water, acetone, and pentane. Figure 5.2 shows a contour map of the vapor core conductance as a function of M_l (horizontal axis) and M_v (vertical axis); the different panels consider evaporator input powers of 0.25 W, 1 W, and 3 W. The vapor core effective conductances of the fluids are marked on the contours. Pentane has the highest M_v and lowest M_l , water has the highest M_l and lowest M_v , and acetone has intermediate values. The thermophysical properties of the fluids are computed using the REFPROP database [48].

At the lowest operating power of 0.25 W, the contour lines are the most parallel to the M_l axis, among the three cases considered. This is consistent with the conclusion drawn with Eq. (5.19) that the fluid choice is dominated by the value of M_v at low powers. In this example, pentane has the highest vapor core effective conductance, and would be the best choice of working fluid. At the intermediate operating power of 1 W, the contour lines are more angled from the horizontal axis (compared to the 0.25 W case) and M_l has a higher influence on the vapor core effective conductance. Thus, pentane is heavily penalized for its low M_l , and acetone is the best choice. At this power, the contour plot includes a vertical line marked $M_{l,min}$. For values of M_l lower than this limit, the minimum wick thickness required to avoid a capillary limit would exceed the available working thickness, and such a fluid is unviable. At the highest power of 3 W, the relative importance of M_l is even greater. The requirement imposed by $M_{l,min}$ excludes pentane and acetone as candidate working fluids. Water, which has the highest value of M_l , is the best choice despite having the lowest value of M_v .

Besides operating power, the working thickness also affects the choice of working fluid. Guidelines for choosing the best-performing working fluid for an ultra-thin vapor chamber can be represented on a map of the operating power (Q) and working thickness (t); this Q - t space can then be divided into regions where particular fluids have the best performance. This is illustrated in Figure 5.3a for a map generated using the example set of fluids (with corresponding values of M_l

and M_v) shown in Table 5.1. To generate this fluid selection map, the value of the vapor core effective conductance for each fluid is computed throughout the Q - t space; regions on the map are colored according to the fluid that has the highest vapor core conductance. The map in Figure 5.3a was generated for a grid of 60×60 points over the range of operating powers and working thicknesses shown. A fluid selection tool with a graphical user interface was developed using the commercial software MATLAB [49] to generate such Q - t space maps as a function of user-defined vapor chamber geometric and operating parameters, and is included as Supplementary Data of the publication [46].

The effect of power and working thickness on fluid choice is apparent in this map (Figure 5.3a). With increasing power, the preferred fluid shifts from one with high M_v (e.g., pentane) to a fluid with high M_l (e.g., water); with increasing thickness, the preferred fluid shifts from high M_l to high M_v . The map includes a region with high powers and low thicknesses which does not map to a viable working fluid; in this region marked in white, none of the candidate fluids included in the analysis have a sufficiently high M_l to ensure a wick thickness less than the available working thickness (i.e., in this region, $M_l < M_{l,min}$ for all candidate fluids).

Note the critical transition lines separating the best-fluid regions in Figure 5.3. Consider loci in the Q - t space defined by $t = C \cdot Q^{0.5}$, where C is an arbitrary constant. Substituting in Eq. (5.17) yields

$$k_{vap} = a_2 M_v \left(C - a_1 \left(\frac{1}{M_l} \right)^{0.5} \right)^3 Q^{1.5}. \quad (5.21)$$

In this expression, the operating power becomes a standalone multiplier. Thus, the vapor core effective conductance for all the fluids is changed by the same factor related to operating power, and the relative performance between different fluids is unchanged on these loci. This is illustrated in Figure 5.3a where one example locus with $C = 100 \mu\text{m W}^{-0.5}$ is shown as a dashed line on which all fluids considered can be ranked by their performance relative to the best fluid; the values in the inset box of Figure 5.3a provide the vapor conductances weighted against that of acetone for this locus. Transition lines on the Q - t map are always defined by loci of this functional form at different values of C .

5.2.2 Effect of Operating Temperature on the Choice of Working Fluid

The temperature-dependence of the thermophysical fluid properties affects the choice of working fluid that would yield the best performance. For computing fluid properties, the operating temperature can be defined as the area-weighted average temperature on the surface of the condenser because the temperature difference across the thickness of the vapor chamber is minimal. The effect of operating temperature on working fluid choice is illustrated in Figure 5.3, where the Q - t maps at temperatures of 325 K, 350 K, and 375 K are shown, generated for the fluids shown in Table 5.1. The appearance of the map changes based on the temperature-dependent thermophysical properties of each fluid. The operating temperature determines the saturation pressure of the fluid in the vapor core. It is critical to note that the walls of the vapor chamber must support the pressure difference between the vapor core and ambient, and mechanical design considerations may exclude some working fluids. For example, in the maps shown in Figure 5.3, fluids which have a vapor pressure higher than an arbitrary limit of 3 atm are shown cross-hatched.

5.3 Conclusion

This work investigated the effects of the thermophysical properties of working fluids on the performance of ultra-thin vapor chambers. At these form factors, the vapor chamber thermal resistance is dominated by the fluid flow in the vapor core. Based on a design target of minimizing thermal resistance, a simplified analytical relationship is proposed between the vapor core thermal conductance and two fluid figures of merit (M_l representing liquid properties and M_v representing vapor properties). A methodology for selecting between working fluids for a given set of ultra-thin vapor chamber geometric and operating parameters was developed. The primary conclusions from this study of the effects of important operating conditions and parameters on the choice of the working fluid are:

- 1) Vapor chambers operating at a relatively high power require a fluid with higher M_l to prevent the required wick thickness from occupying the entire vapor space; at lower powers, a fluid with high M_v is preferred, with a tradeoff between these prioritizations in the intermediate power range;

- 2) With decreasing vapor chamber thickness, the preference changes from a fluid with high M_v to one with high M_l ; at the lowest thicknesses, a high M_l becomes a requirement so that the wick does not occupy the entire thickness available; and
- 3) The unique temperature-dependence of thermophysical properties for each fluid govern fluid selection; caution must be exercised to ensure a reasonable vapor pressure at which the structural integrity of the vapor chamber is not compromised.

Nomenclature

a_1, a_2	constants in k_{vap} relation [-]
A	factor $(\frac{\phi^3}{f(1-\phi)^2})$ [-]
C	arbitrary constant [m W ^{-0.5}]
d_p	particle diameter [m]
f	factor in Carman-Kozeny relation [-]
F_s	factor of safety [-]
h_{fg}	specific enthalpy of vaporization [kJ kg ⁻¹]
k_{vap}	vapor core effective conductance [W K ⁻¹]
k_{wick}	wick effective conductivity [W m ⁻¹ K ⁻¹]
K	permeability [m ²]
m	ratio of particle diameter with effective pore radius (d_p/r_{eff}) [-]
\dot{m}	mass flow rate [kg s ⁻¹]
M_l	liquid figure of merit $(\frac{\gamma\rho_l h_{fg}}{\mu_l})$ [W m ⁻²]
$M_{l,min}$	minimum required liquid figure of merit [W m ⁻²]
M_v	vapor figure of merit $(\frac{P_v \rho_v h_{fg}^2}{\mu_v R_g T_v^2})$ [W m ⁻³ K ⁻¹]
n	number of particle diameters along the wick thickness [-]
P	pressure [Pa]
P_v	vapor pressure [Pa]
P_{cap}	capillary pressure [Pa]
Q	power [W]
r	radial coordinate [m]
r_{eff}	effective pore radius [m]
R	radius of vapor chamber [m]
R_e	radius of evaporator [m]
Re	Reynolds number [-]
R_g	gas constant [J kg ⁻¹ K ⁻¹]
t	working thickness [m]
t_{vap}	vapor core thickness [m]

t_{wick}	wick thickness [m]
T	temperature [K]
u_r	radial velocity [m s^{-1}]
U_r	radial velocity scale [m s^{-1}]
z	axial coordinate [m]

Greek symbols

γ	surface tension [N m^{-1}]
μ	dynamic viscosity [Pa s]
ρ	density [kg m^{-3}]
ϕ	porosity [-]

Subscript

l	liquid phase
v	vapor phase
vap	vapor core domain
$wick$	wick domain

Table 5.1. Fluid property figures of merit for six fluids at $T_v = 325$ K.

	M_l (W/m ²)	M_v (W/m ³ K)
Acetone	3.06×10^{10}	23.2×10^{13}
Methanol	4.52×10^{10}	5.99×10^{13}
Water	30.0×10^{10}	1.29×10^{13}
Pentane	1.47×10^{10}	75.6×10^{13}
Ethanol	1.87×10^{10}	7.31×10^{13}
R141b	1.22×10^{10}	73.0×10^{13}

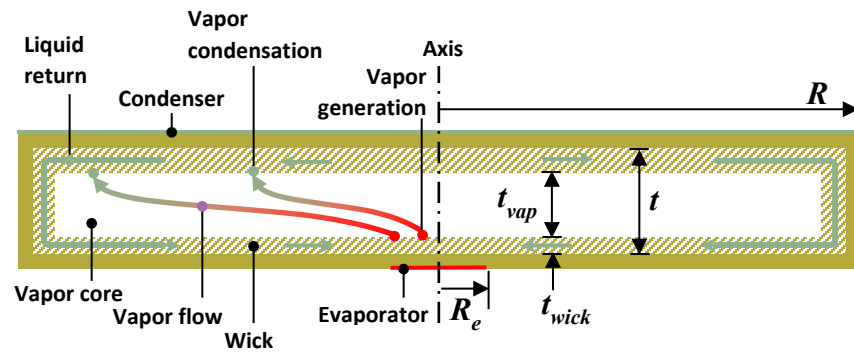


Figure 5.1. Schematic of the operation and the geometry of a vapor chamber.

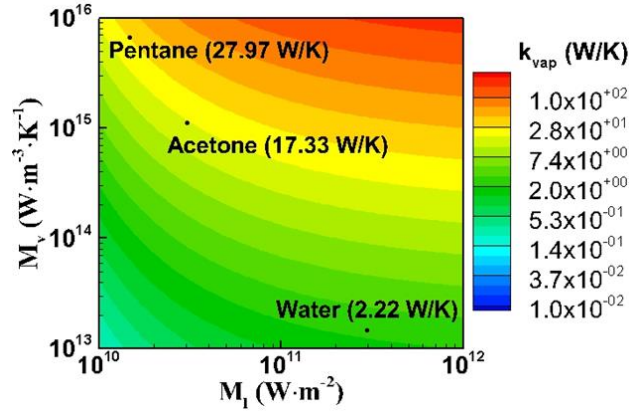
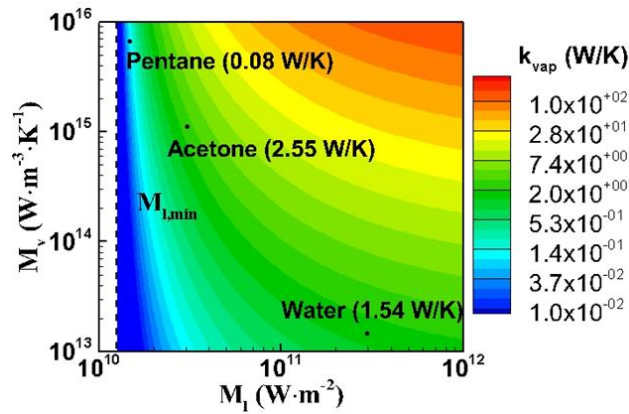
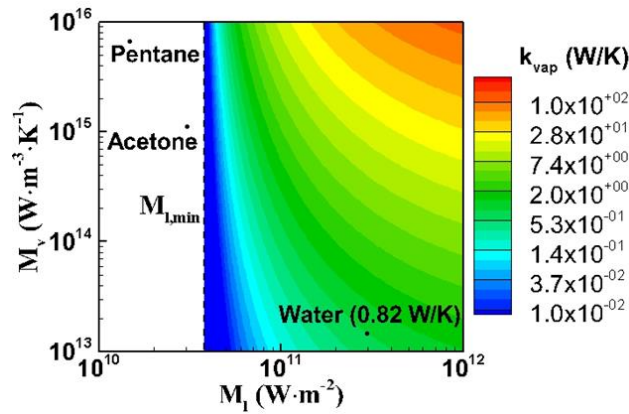
(a) $Q = 0.25$ W(b) $Q = 1$ W(c) $Q = 3$ W

Figure 5.2. Contours of effective vapor core conductance as a function of the liquid and vapor figures of merit for operating powers of (a) 0.25 W, (b) 1 W, and (c) 3 W. $R = 45$ mm, $R_e = 5$ mm, $t = 100$ μm , $n = 3$, $F_s = 2$; the wick is sintered copper ($m = 0.21$, $f = 150$) with 60% porosity; thermophysical properties evaluated at 325 K.

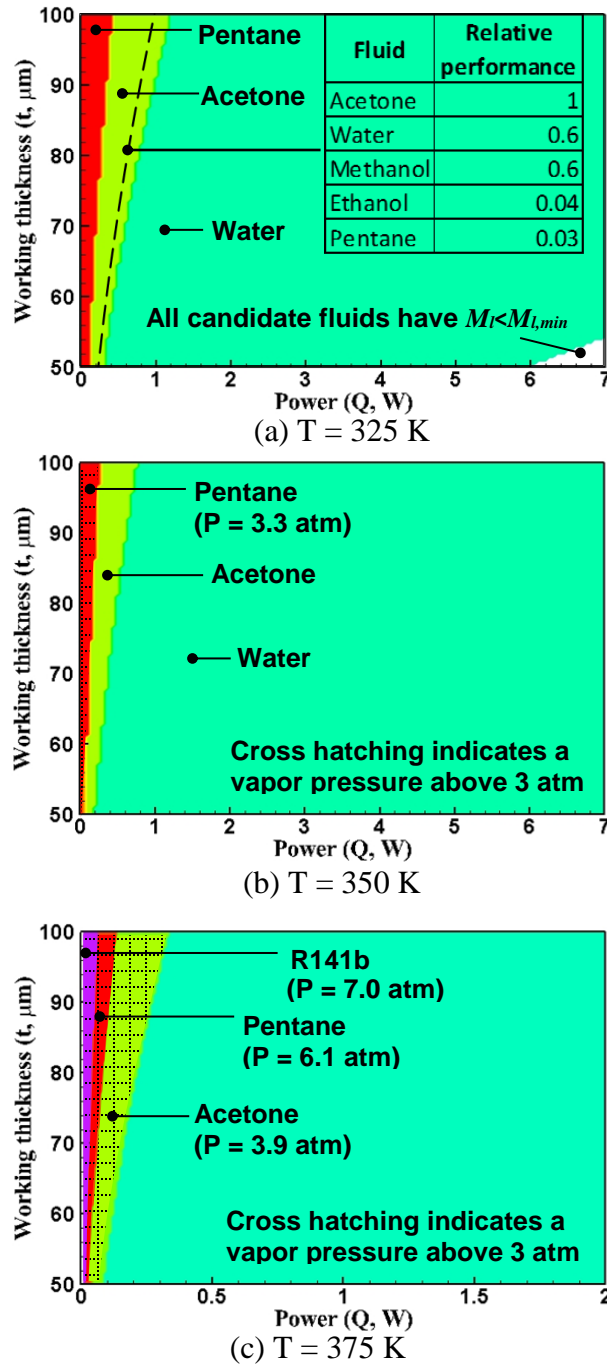


Figure 5.3. Plots showing the best working fluids in the power-working thickness space. Properties are calculated at (a) $T_v = 325$ K, (b) $T_v = 350$ K, and (c) $T_v = 375$ K. $R = 45$ mm, $R_e = 5$ mm, $n = 3$, $F_s = 2$; the wick is sintered copper ($m = 0.21$, $f = 150$) with 60% porosity.

6. A VALIDATED TIME-STEPPING ANALYTICAL MODEL FOR 3D TRANSIENT VAPOR CHAMBER TRANSPORT

This chapter develops a low-cost, semi-analytical model for transient vapor chamber operation. The model solves for mass, momentum, and energy transport in the vapor chamber wall, wick and vapor core, along with phase change at the wick–vapor interface. The model simplifies the governing equations to a set of linear differential equations, which are solved using Fourier series substitutions and implicit time-stepping. Multiple, arbitrarily shaped, time-varying heat inputs can be imposed on the evaporator-side of the vapor chamber, with a uniform convective boundary condition on the condenser side. The computational cost of the model is compared with that of a high-fidelity, finite-volume numerical model. The material in this chapter is published in the *International Journal of Heat and Mass Transfer* [50] and was presented at the *Sixteenth Intersociety Conference on Thermal and Thermomechanical Phenomena in Electronic Systems* [51] in 2017 and is published in the proceedings.

6.1 Model Development

6.1.1 Geometry, Governing Equations, and Boundary Conditions

The vapor chamber has a three-dimensional rectangular geometry; Figure 6.1 illustrates the wall, wick, and vapor core domains and their sizes in the x , y , and z coordinate directions. The wall, wick and the vapor-core have dimensions of L_x and L_y , respectively, in the x and y directions. The vapor chamber is subjected to multiple arbitrarily shaped and time-varying heat inputs on one of its faces ($z = 0$), while the other face ($z = h_{wall,1} + h_{wick,1} + h_{vap} + h_{wick,2} + h_{wall,2}$) is subjected to a uniform convective boundary condition. The lateral walls are insulated. The thickness of the walls and wick along the sides at $x = 0$, $x = L_x$, $y = 0$ and $y = L_y$ is assumed to be negligible.

The governing equations solved in the vapor chamber transport model are described below. The wick is assumed to be a homogeneous porous medium with its pores fully saturated by the working liquid; the model does not account for recession of liquid into the wick. Flow in the wick and vapor core is assumed to be laminar and incompressible. The governing equations for mass, momentum and energy transport are

$$\frac{\partial u}{\partial x} + \frac{\partial v}{\partial y} + \frac{\partial w}{\partial z} = 0 \quad (6.1)$$

$$\begin{aligned} & \rho \frac{\partial \vec{V}}{\partial t} + \rho \left(u \frac{\partial \vec{V}}{\partial x} + v \frac{\partial \vec{V}}{\partial y} + w \frac{\partial \vec{V}}{\partial z} \right) \\ &= -\nabla(\phi P) + \mu \left(\frac{\partial^2 \vec{V}}{\partial x^2} + \frac{\partial^2 \vec{V}}{\partial y^2} + \frac{\partial^2 \vec{V}}{\partial z^2} \right) - \frac{\mu \phi}{K} \vec{V} \end{aligned} \quad (6.2)$$

$$\begin{aligned} & (\rho C_p)_{eff} \left(\frac{\partial T}{\partial t} \right) + (\rho C_p)_l \left(u \frac{\partial T}{\partial x} + v \frac{\partial T}{\partial y} + w \frac{\partial T}{\partial z} \right) \\ &= k_{eff} \left(\frac{\partial^2 T}{\partial x^2} + \frac{\partial^2 T}{\partial y^2} + \frac{\partial^2 T}{\partial z^2} \right) \end{aligned} \quad (6.3)$$

In the vapor core, the porosity ϕ is 1 and the permeability K is ∞ . For the wick, k_{eff} is the effective conductivity of the porous medium. For the wall and vapor core, the effective conductivity is equal to the corresponding material thermal conductivity. For the wick and the vapor core, $(\rho C_p)_l$ is the fluid volumetric heat capacity, while for the wall, $(\rho C_p)_l$ is set to zero; $(\rho C_p)_{eff}$ is the effective volumetric heat capacity, and

$$\text{for the wick, } (\rho C_p)_{eff} = \phi(\rho C_p)_l + (1-\phi)(\rho C_p)_s,$$

$$\text{for the wall, } (\rho C_p)_{eff} = (\rho C_p)_{wall}, \text{ and}$$

$$\text{for the vapor core, } (\rho C_p)_{eff} = (\rho C_p)_{vap},$$

where $(\rho C_p)_s$ is the volumetric heat capacity of the solid material of the porous wick. All thermophysical properties are assumed to be constant at a given time instant.

The mass flux rate due to phase change at the wick–vapor interface is evaluated using the difference between the local interface temperature and the local vapor-core saturation temperature [52] as:

$$\dot{m}'' = \frac{2\sigma}{2-\sigma} \frac{h_{fg} \rho_{vap}}{T_{vap}^{1.5}} \left(\frac{1}{2\pi R} \right)^{0.5} (T_{int} - T_{sat}). \quad (6.4)$$

A positive value indicates evaporation, while a negative value indicates condensation. The value

of σ is chosen to be 0.03 [44]. The saturation temperature in the vapor core is computed using the Clausius-Clapeyron equation

$$\frac{dP_{vap}}{dT_{sat}} = \frac{h_{fg} P_{vap}}{RT_{sat}^2}. \quad (6.5)$$

The boundary conditions for the vapor core specify that there is no slip in velocity at the thermally insulated lateral sidewalls.

$$\begin{aligned} \text{at } x = 0, \quad u = v = w = 0; \quad \frac{\partial T}{\partial x} &= 0 \\ \text{at } x = L_x, \quad u = v = w = 0; \quad \frac{\partial T}{\partial x} &= 0 \\ \text{at } y = 0, \quad u = v = w = 0; \quad \frac{\partial T}{\partial y} &= 0 \\ \text{at } y = L_y, \quad u = v = w = 0; \quad \frac{\partial T}{\partial y} &= 0 \end{aligned} \quad (6.6)$$

At the interfaces with the wick domain, the velocity has a no-slip condition and mass and energy are conserved across the interface (accounting for enthalpy of vaporization):

$$\begin{aligned} \text{at } z = h_{wall,1} + h_{wick,1}, \\ (\rho w)_{wick} &= (\rho w)_{vap}; \quad u = v = 0; \\ \left(-k_{eff} \frac{\partial T}{\partial z} \right)_{wick} - \dot{m}_1'' h_{fg} &= \left(-k \frac{\partial T}{\partial z} \right)_{vap} \end{aligned} \quad (6.7)$$

$$\begin{aligned} \text{at } z = h_{wall,1} + h_{wick,1} + h_{vap}, \\ (\rho w)_{wick} &= (\rho w)_{vap}; \quad u = v = 0; \\ \left(k_{eff} \frac{\partial T}{\partial z} \right)_{wick} - \dot{m}_2'' h_{fg} &= \left(k \frac{\partial T}{\partial z} \right)_{vap} \end{aligned}$$

where \dot{m}_1'' is the evaporative mass flux rate at $z = h_{wall,1} + h_{wick,1}$ and \dot{m}_2'' is the value at $z = h_{wall,1} + h_{wick,1} + h_{vap}$. The wall and wick layers on the evaporator and condenser sides are indicated by the indices 1 and 2, respectively. The two walls, two wicks, and vapor core are termed as *zones* henceforth. The boundary conditions at the edges of both wicks are

$$\begin{aligned}
&\text{at } x = 0, \quad w = 0; \quad \frac{\partial T}{\partial x} = 0 \\
&\text{at } x = L_x, \quad w = 0; \quad \frac{\partial T}{\partial x} = 0 \\
&\text{at } y = 0, \quad w = 0; \quad \frac{\partial T}{\partial y} = 0 \\
&\text{at } y = L_y, \quad w = 0; \quad \frac{\partial T}{\partial y} = 0
\end{aligned} \tag{6.8}$$

Flow of liquid between the two wicks is connected at the boundaries at x and y limits by imposing the conditions shown below.

$$\begin{aligned}
&\text{at } x = 0, \quad u_{wick,1} = -u_{wick,2}; \quad P_{wick,1} = P_{wick,2} \\
&\text{at } x = L_x, \quad u_{wick,1} = -u_{wick,2}; \quad P_{wick,1} = P_{wick,2} \\
&\text{at } y = 0, \quad v_{wick,1} = -v_{wick,2}; \quad P_{wick,1} = P_{wick,2} \\
&\text{at } y = L_y, \quad v_{wick,1} = -v_{wick,2}; \quad P_{wick,1} = P_{wick,2}
\end{aligned} \tag{6.9}$$

At the interfaces of the wicks with the wall and the vapor core, the velocity has a no-slip condition and energy is conserved:

$$\text{at } z = h_{\text{wall},1}, \mathbf{u} = \mathbf{v} = \mathbf{w} = \mathbf{0};$$

$$\left(-k \frac{\partial T}{\partial z} \right)_{\text{wall}} = \left(-k_{\text{eff}} \frac{\partial T}{\partial z} \right)_{\text{wick}}$$

$$\text{at } z = h_{\text{wall},1} + h_{\text{wick},1},$$

$$(\rho w)_{\text{wick}} = (\rho w)_{\text{vap}}; \mathbf{u} = \mathbf{v} = \mathbf{0};$$

$$\left(-k_{\text{eff}} \frac{\partial T}{\partial z} \right)_{\text{wick}} - \dot{m}_1'' h_{fg} = \left(-k \frac{\partial T}{\partial z} \right)_{\text{vap}}$$

$$\text{at } z = h_{\text{wall},1} + h_{\text{wick},1} + h_{\text{vap}},$$

$$(\rho w)_{\text{wick}} = (\rho w)_{\text{vap}}; \mathbf{u} = \mathbf{v} = \mathbf{0};$$

$$\left(k_{\text{eff}} \frac{\partial T}{\partial z} \right)_{\text{wick}} - \dot{m}_2'' h_{fg} = \left(k \frac{\partial T}{\partial z} \right)_{\text{vap}}$$

(6.10)

$$\text{at } z = h_{\text{wall}_-1} + h_{\text{wick}_-1} + h_{\text{vap}} + h_{\text{wick}_-2},$$

$$\mathbf{u} = \mathbf{v} = \mathbf{w} = \mathbf{0}; \left(-k \frac{\partial T}{\partial z} \right)_{\text{wall}} = \left(-k_{\text{eff}} \frac{\partial T}{\partial z} \right)_{\text{wick}}$$

The lateral boundaries of the vapor chamber are insulated, which yields the following boundary conditions for both the walls:

$$\text{at } x = 0, \quad \frac{\partial T}{\partial x} = 0$$

$$\text{at } x = L_x, \quad \frac{\partial T}{\partial x} = 0$$

$$\text{at } y = 0, \quad \frac{\partial T}{\partial y} = 0$$

$$\text{at } y = L_y, \quad \frac{\partial T}{\partial y} = 0$$

(6.11)

The vapor chamber walls receive heat input(s) at the $z = 0$ surface, are exposed to a convective condition at the $z = h_{\text{wall},1} + h_{\text{wick},1} + h_{\text{vap}} + h_{\text{wick},2} + h_{\text{wall},2}$ surface, and energy is conserved at the wick interfaces:

$$\begin{aligned}
& \text{at } z = 0, \left(-k \frac{\partial T}{\partial z} \right)_{\text{wall}} = q_{in}''(x, y) \\
& \text{at } z = h_{\text{wall},1}, \left(-k \frac{\partial T}{\partial z} \right)_{\text{wall}} = \left(-k_{\text{eff}} \frac{\partial T}{\partial z} \right)_{\text{wick}} \\
& \text{at } z = h_{\text{wall},1} + h_{\text{wick},1} + h_{\text{vap}} + h_{\text{wick},2}, \quad . \quad (6.12) \\
& \left(-k \frac{\partial T}{\partial z} \right)_{\text{wall}} = \left(-k_{\text{eff}} \frac{\partial T}{\partial z} \right)_{\text{wick}} \\
& \text{at } z = h_{\text{wall},1} + h_{\text{wick},1} + h_{\text{vap}} + h_{\text{wick},2} + h_{\text{wall},2}, \\
& \left(-k \frac{\partial T}{\partial z} \right)_{\text{wall}} = h(T - T_{\infty})
\end{aligned}$$

6.1.2 Scaling Analysis

To render the governing equations more amenable to analytical solution, assumptions regarding the scales of the variables are used to eliminate terms of comparatively low magnitude. The scales used are shown in Table 6.1. Time scales based on z -diffusion used for momentum transport in the wick and the vapor core are

$$\begin{aligned}
& \text{for wick 1, } \tau \sim \frac{\rho_{\text{wick}} h_{\text{wick},1}^2}{\mu_{\text{wick}}}; \text{ for wick 2, } \tau \sim \frac{\rho_{\text{wick}} h_{\text{wick},2}^2}{\mu_{\text{wick}}}; \\
& \text{for vapor core, } \tau \sim \frac{\rho_{\text{vap}} h_{\text{vap}}^2}{\mu_{\text{vap}}} . \quad (6.13)
\end{aligned}$$

The following conditions are imposed on the scale variables in the vapor core and the wick. The thicknesses of the two wicks and the vapor core are considered to be much smaller than the size of the vapor chamber in the x and y directions.

$$\begin{aligned}
& h_{\text{vap}} \ll L_x, h_{\text{wick},1} \ll L_x, h_{\text{wick},2} \ll L_x, \\
& h_{\text{vap}} \ll L_y, h_{\text{wick},1} \ll L_y, h_{\text{wick},2} \ll L_y \quad (6.14)
\end{aligned}$$

This condition allows the diffusion in the x and y directions in the momentum and energy equations for the vapor core and wicks to be assumed negligible compared to diffusion in the z direction (in the respective equations and zones). Thus,

$$\frac{\partial^2}{\partial x^2} \ll \frac{\partial^2}{\partial z^2}, \frac{\partial^2}{\partial y^2} \ll \frac{\partial^2}{\partial z^2} \quad (6.15)$$

The following conditions are imposed on the scale variables regarding flow in the vapor core and the wick:

$$\begin{aligned} \left(\text{Re}_{x,vap} \frac{h_{vap}^2}{L_x^2} \right) \ll 1, \quad \left(\text{Re}_{x,wick_1} \frac{h_{wick,1}^2}{L_x^2} \right) \ll 1, \\ \left(\text{Re}_{x,wick_2} \frac{h_{wick,2}^2}{L_x^2} \right) \ll 1, \quad \left(\text{Re}_{y,vap} \frac{h_{vap}^2}{L_y^2} \right) \ll 1, \\ \left(\text{Re}_{y,wick_1} \frac{h_{wick,1}^2}{L_y^2} \right) \ll 1, \quad \left(\text{Re}_{y,wick_2} \frac{h_{wick,2}^2}{L_y^2} \right) \ll 1 \end{aligned} \quad (6.16)$$

These conditions allow the convection terms in the momentum equation for the wicks and the vapor core to be assumed negligible compared to diffusion in the z direction. Thus,

$$\rho u \frac{\partial}{\partial x} \ll \mu \frac{\partial^2}{\partial z^2}, \quad \rho v \frac{\partial}{\partial y} \ll \mu \frac{\partial^2}{\partial z^2}, \quad \rho w \frac{\partial}{\partial z} \ll \mu \frac{\partial^2}{\partial z^2} \quad (6.17)$$

The conditions imposed on the scale variables, regarding energy transport in the wicks and the vapor core, are:

$$\begin{aligned}
& \left(\text{Pr}_{vap} \text{Re}_{x,vap} \frac{h_{vap}^2}{L_x^2} \right) \ll 1, \\
& \left(\text{Pr}_{wick} \text{Re}_{x,wick,1} \frac{h_{wick,1}^2}{L_x^2} \right) \ll 1, \\
& \left(\text{Pr}_{wick} \text{Re}_{x,wick,2} \frac{h_{wick,2}^2}{L_x^2} \right) \ll 1, \\
& \left(\text{Pr}_{vap} \text{Re}_{y,vap} \frac{h_{vap}^2}{L_y^2} \right) \ll 1, \\
& \left(\text{Pr}_{wick} \text{Re}_{y,wick,1} \frac{h_{wick,1}^2}{L_y^2} \right) \ll 1, \\
& \left(\text{Pr}_{wick} \text{Re}_{y,wick,2} \frac{h_{wick,2}^2}{L_y^2} \right) \ll 1
\end{aligned} \tag{6.18}$$

These conditions allow the convection terms in the energy equation for the wicks and the vapor core to be assumed negligible compared to diffusion in the z direction. Thus,

$$\begin{aligned}
\rho C_{p,l} u \frac{\partial}{\partial x} \ll k \frac{\partial^2}{\partial z^2}, \quad \rho C_{p,l} v \frac{\partial}{\partial y} \ll k \frac{\partial^2}{\partial z^2}, \\
\rho C_{p,l} w \frac{\partial}{\partial z} \ll k \frac{\partial^2}{\partial z^2}
\end{aligned} \tag{6.19}$$

In the two wicks, the permeability is proportional to the square of the particle diameter, which is smaller than the wick thickness. Thus, the following conditions are imposed regarding the porous medium:

$$\frac{K_{wick}}{\phi_{wick}} \ll h_{wick,1}^2, \quad \frac{K_{wick}}{\phi_{wick}} \ll h_{wick,2}^2. \tag{6.20}$$

Based on these conditions and the time scales, it may be written for the two wicks,

$$\mu \frac{\partial^2}{\partial z^2} \ll \frac{\mu \phi}{K}, \quad \rho \frac{\partial}{\partial t} \ll \frac{\mu \phi}{K}. \tag{6.21}$$

Given the above simplifications, the governing momentum and energy equations are simplified. For the vapor core, Eqs. (6.2) and (6.3) reduce to:

$$\rho \frac{\partial \vec{V}}{\partial t} = -\nabla P + \mu \frac{\partial^2 \vec{V}}{\partial z^2} \quad (6.22)$$

$$(\rho C_P)_{eff} \left(\frac{\partial T}{\partial t} \right) = k_{eff} \frac{\partial^2 T}{\partial z^2}, \quad (6.23)$$

and for the wick zones to

$$\nabla(\phi P) = -\frac{\mu \phi}{K} \vec{V} \quad (6.24)$$

$$(\rho C_P)_{eff} \left(\frac{\partial T}{\partial t} \right) = k_{eff} \frac{\partial^2 T}{\partial z^2}. \quad (6.25)$$

6.1.3 Combined Energy Equation

The energy equations for the walls (6.3), vapor core (6.23), and wicks (6.25) are integrated along z in each zone, over their respective thicknesses. Thus, for the evaporator-side wall,

$$\begin{aligned} & (\rho C_P)_{eff} \left(\frac{\partial \bar{T}_{wall,1}}{\partial t} \right) \\ & = k_{eff} \left(\frac{\partial^2 \bar{T}_{wall,1}}{\partial x^2} + \frac{\partial^2 \bar{T}_{wall,1}}{\partial y^2} \right) + \frac{k_{eff}}{h_{wall,1}} \frac{\partial T}{\partial z} \Big|_0^{h_{wall,1}}; \end{aligned} \quad (6.26)$$

for the condenser-side wall,

$$\begin{aligned} & (\rho C_P)_{eff} \left(\frac{\partial \bar{T}_{wall,2}}{\partial t} \right) = k_{eff} \left(\frac{\partial^2 \bar{T}_{wall,2}}{\partial x^2} + \frac{\partial^2 \bar{T}_{wall,2}}{\partial y^2} \right) \\ & + \frac{k_{eff}}{h_{wall,2}} \frac{\partial T}{\partial z} \Big|_{h_{wall,1}+h_{wick,1}+h_{vap}+h_{wick,2}+h_{wall,2}}^{h_{wall,1}+h_{wick,1}+h_{vap}+h_{wick,2}+h_{wall,2}}; \end{aligned} \quad (6.27)$$

for the evaporator-side wick,

$$(\rho C_P)_{eff} \left(\frac{\partial \bar{T}_{wick,1}}{\partial t} \right) = \frac{k_{eff}}{h_{wick,1}} \frac{\partial T}{\partial z} \Big|_{h_{wall,1}}^{h_{wall,1}+h_{wick,1}}; \quad (6.28)$$

for the condenser-side wick,

$$(\rho C_p)_{eff} \left(\frac{\partial \bar{T}_{wick,2}}{\partial t} \right) = \frac{k_{eff}}{h_{wick,2}} \frac{\partial T}{\partial z} \Big|_{h_{wall,1}+h_{wick,1}+h_{vap}+h_{wick,2}}^{h_{wall,1}+h_{wick,1}+h_{vap}} ; \quad (6.29)$$

and for the vapor core

$$(\rho C_p)_{eff} \left(\frac{\partial \bar{T}_{vap}}{\partial t} \right) = \frac{k_{eff}}{h_{vap}} \frac{\partial T}{\partial z} \Big|_{h_{wall,1}+h_{wick,1}}^{h_{wall,1}+h_{wick,1}+h_{vap}} ; \quad (6.30)$$

where \bar{T} is the z -averaged temperature in each zone. Information regarding the variation of temperature in the z direction is lost due to the integration. Hence, profiles are assigned to temperature in the z direction. In the walls and the wicks, the temperature difference across the thickness is assumed to be negligible compared to the temperature difference along the x and y directions. The temperature is thus taken to be constant along the z direction. In the vapor core, the temperature is assumed to have a quadratic profile in the z direction. To interface between the zones, continuity is imposed at the zone boundaries. Thus, in the walls and the wicks,

$$\bar{T}_{wall,1} = \bar{T}_{wick,1} = \bar{T}_1 \quad \text{and} \quad \bar{T}_{wall,2} = \bar{T}_{wick,2} = \bar{T}_2 . \quad (6.31)$$

The temperature in the vapor core can be written as

$$T = a(z - h_{wall,1} - h_{wick,1})^2 + b(z - h_{wall,1} - h_{wick,1}) + c, \quad (6.32)$$

$$a = \frac{3(\bar{T}_1 + \bar{T}_2 - 2\bar{T}_{vap})}{h_{vap}^2}, \quad b = \frac{6\bar{T}_{vap} - 4\bar{T}_1 - 2\bar{T}_2}{h_{vap}}, \quad c = \bar{T}_1 .$$

Combining the energy equations (6.26) through (6.30) for all zones, using the boundary conditions in Eqs. (6.7), (6.10) and (6.12), and the assumed temperature profiles specified by Eqs. (6.31) and (6.32), energy transport in the vapor chamber is represented by a linear differential equation with a three-component vector variable, written as

$$\frac{\partial \underline{\Theta}}{\partial t} = \underline{A} \left(\frac{\partial^2 \underline{\Theta}}{\partial x^2} + \frac{\partial^2 \underline{\Theta}}{\partial y^2} \right) + \underline{B} \underline{\Theta} + \underline{C},$$

$$\underline{\Theta} = \begin{bmatrix} \bar{T}_1 \\ \bar{T}_{vap} \\ \bar{T}_2 \end{bmatrix}, \quad \underline{C} = \begin{bmatrix} \frac{q_{in}'' - \dot{m}_1'' h_{fg}}{\beta_1} \\ 0 \\ \frac{hT_\infty - \dot{m}_2'' h_{fg}}{\beta_2} \end{bmatrix}, \quad (6.33)$$

$$\beta_1 = (\rho C_P)_{wall,1} h_{wall,1} + (\rho C_P)_{eff,wick,1} h_{wick,1},$$

$$\beta_2 = (\rho C_P)_{wall,2} h_{wall,2} + (\rho C_P)_{eff,wick,2} h_{wick,2},$$

The matrices \underline{A} (units of $[m^2 s^{-1}]$) and \underline{B} (units of $[s^{-1}]$) contain thermophysical properties and geometric variables:

$$\underline{A} = \begin{bmatrix} \frac{k_{wall,1} h_{wall,1}}{\beta_1} & 0 & 0 \\ 0 & 0 & 0 \\ 0 & 0 & \frac{k_{wall,2} h_{wall,2}}{\beta_2} \end{bmatrix},$$

$$\underline{B} = \begin{bmatrix} \frac{-k_{vap}}{\beta_1 h_{vap}} & 0 & 0 \\ 0 & \frac{6k_{vap}}{h_{vap}^2 (\rho C_P)_{vap}} & 0 \\ 0 & 0 & \frac{-k_{vap}}{\beta_2 h_{vap}} \end{bmatrix} \times \begin{bmatrix} 4 & -6 & 2 \\ 1 & -2 & 1 \\ 2 & -6 & 4 + \frac{h_{vap} h}{k_{vap}} \end{bmatrix}. \quad (6.34)$$

Eq. (6.33) contains the two unknown mass flux rates due to phase change at the two interfaces, which are solved for in the next two sections.

6.1.4 Vapor Core Hydrodynamics

The continuity and momentum equations for the vapor core are used to obtain a single equation for the pressure field in this section. The characteristic time scales of thermal diffusion in the x and y directions per the system energy equation (6.33) are $\sim L_x^2 / \alpha_{wall}$ and $\sim L_y^2 / \alpha_{wall}$, respectively. The characteristic time scale of momentum diffusion in the z direction per the vapor momentum

equation (6.22) is $\sim h_{vap}^2 / \alpha_{vap}$. For typical vapor chamber geometries and working fluid properties, assuming $h_{vap}^2 / \alpha_{vap} \ll L_x^2 / \alpha_{wall}$, the vapor hydrodynamics can be considered quasi-steady. Thus, the momentum equation (6.22) in the vapor core reduces to:

$$\nabla P = \mu \frac{\partial^2 \vec{V}}{\partial z^2}. \quad (6.35)$$

Eq. (6.35) along with the boundary conditions in (6.7) yields,

$$\begin{aligned} u &= \frac{1}{2\mu} \frac{\partial P}{\partial x} \left(z^2 - (2h_{wall,l} + 2h_{wick,l} + h_{vap})z + \right. \\ &\quad \left. (h_{wall,l} + h_{wick,l})(h_{wall,l} + h_{wick,l} + h_{vap}) \right), \\ v &= \frac{1}{2\mu} \frac{\partial P}{\partial y} \left(z^2 - (2h_{wall,l} + 2h_{wick,l} + h_{vap})z + \right. \\ &\quad \left. (h_{wall,l} + h_{wick,l})(h_{wall,l} + h_{wick,l} + h_{vap}) \right) \end{aligned} \quad (6.36)$$

Substituting velocity relations from Eq. (6.36) into the mass conservation in Eq. (6.1) and integrating along z over the vapor core thickness, using the boundary conditions in (6.7), yields

$$\frac{\partial^2 P}{\partial x^2} + \frac{\partial^2 P}{\partial y^2} = -\frac{12\mu}{\rho h_{vap}^3} (\dot{m}_2'' + \dot{m}_1'') \quad (6.37)$$

6.1.5 Coupling Energy Equation with Vapor Hydrodynamics

In this section, the unknown mass flux rates in Eq. (6.33) are related to the pressure field in the vapor core and the temperature field. The Clausius-Clapeyron equation (6.5) is simplified by assuming a linear relation between the vapor pressure and saturation temperature. Thus, the right hand side of the equation is substituted by an average in the field

$$\frac{dP}{dT_{sat}} = \lambda = \frac{h_{fg} P_o}{R (T_{sat}^2)_{mean}}, \quad (6.38)$$

where P_o is the saturation pressure corresponding to the volume-averaged vapor core temperature, and $(T_{sat}^2)_{mean}$ is the volume average value of T_{sat}^2 in the vapor core. The computation of the mass flux rate due to phase change (Eq. (6.4)) is simplified to create a linear relation with the difference in the interface temperature and the vapor core saturation temperature. Thus,

$$\begin{aligned} \dot{m}'' &= \varphi(T_{int} - T_{sat}), \\ \varphi &= \frac{2\sigma}{2 - \sigma} \frac{h_{fg} \rho_{vap}}{(T_{vap}^{1.5})_{mean}} \left(\frac{1}{2\pi R} \right)^{0.5} \end{aligned} \quad (6.39)$$

where $(T_{vap}^{1.5})_{mean}$ is the volume-averaged value of $T_{vap}^{1.5}$. The T_{sat} value at the interface on the evaporator side is equal to \bar{T}_1 and at the interface on the condenser side is equal to \bar{T}_2 . The pressure variable in Eq. (6.37) is substituted with the saturation temperature using Eq. (6.38). The mass flux rate terms in Eq. (6.37) are replaced using (6.39). Thus, an equation is obtained for the saturation temperature as

$$\lambda \left(\frac{\partial^2 T_{sat}}{\partial x^2} + \frac{\partial^2 T_{sat}}{\partial y^2} \right) = - \frac{12\mu_{vap}}{\rho_{vap} h_{vap}^3} \varphi (\bar{T}_1 + \bar{T}_2 - 2T_{sat}). \quad (6.40)$$

The boundary conditions for saturation temperature are obtained from Eq. (6.6), using the relations from Eq. (6.36) and Eq. (6.38).

$$\begin{aligned} &\text{at } x = 0 \text{ and } x = L_x, \\ u = 0 &\Rightarrow \frac{\partial P}{\partial x} = 0 \Rightarrow \frac{\partial T_{sat}}{\partial x} = 0 \\ &\text{at } y = 0 \text{ and } y = L_y, \\ v = 0 &\Rightarrow \frac{\partial P}{\partial y} = 0 \Rightarrow \frac{\partial T_{sat}}{\partial y} = 0 \end{aligned} \quad (6.41)$$

6.1.6 Solution to the Combined Energy Equation

The combined energy equation (Eq. (6.33)) and the saturation temperature equation (Eq. (6.40)) are solved using Fourier series substitution. For the combined energy equation, the substitution

$$\underline{\Theta} = \begin{bmatrix} \bar{T}_1 \\ \bar{T}_{vap} \\ \bar{T}_2 \end{bmatrix} = \sum_{l=0}^{\infty} \sum_{k=0}^{\infty} \left(\underline{a}_{lk} \cos\left(\frac{l\pi x}{L_x}\right) \cos\left(\frac{k\pi y}{L_y}\right) \right), \quad (6.42)$$

$$\text{where } \underline{a}_{lk} = \begin{bmatrix} a_1 \\ a_{vap} \\ a_2 \end{bmatrix}_{lk}$$

is used. This satisfies the boundary conditions in Eqs. (6.6), (6.8), and (6.11) at $x = 0$, $x = L_x$, $y = 0$ and $y = L_y$. For the saturation temperature equation, the substitution

$$T_{sat} = \sum_{l=0}^{\infty} \sum_{k=0}^{\infty} \left(c_{lk} \cos\left(\frac{l\pi x}{L_x}\right) \cos\left(\frac{k\pi y}{L_y}\right) \right) \quad (6.43)$$

satisfies the boundary conditions in Eq. (6.41). Substituting Eqs. (6.42) and (6.43) into Eq. (6.40) yields

$$c_{lk} = \frac{[1 \ 0 \ 1] \underline{a}_{lk}}{\left(\frac{\lambda \rho_{vap} h_{vap}^3}{12 \mu_{vap} \varphi} \pi^2 \left(\frac{l^2}{L_x^2} + \frac{k^2}{L_y^2} \right) + 2 \right)}. \quad (6.44)$$

The mass flux rate defined in Eq. (6.39) is substituted into Eq. (6.33); $\underline{\Theta}$ in Eq. (6.33) is substituted using Eq. (6.42), and T_{sat} (introduced from Eq. (6.39)) is substituted using Eq. (6.43).

Eq. (6.44) is then used to eliminate the c_{lk} variable:

$$\sum_{l=0}^{\infty} \sum_{k=0}^{\infty} \left(\underline{b}_{lk} \cos\left(\frac{l\pi x}{L_x}\right) \cos\left(\frac{k\pi y}{L_y}\right) \right) = \begin{bmatrix} \frac{q_{in}''}{\beta_1} \\ 0 \\ \frac{hT_{\infty}}{\beta_2} \end{bmatrix}, \quad (6.45)$$

where

$$\underline{b}_{lk} = \frac{\partial \underline{a}_{lk}}{\partial t} + \underline{G} \underline{a}_{lk}. \quad (6.46)$$

The matrix \underline{G} contains thermophysical and geometric parameters.

$$\begin{aligned}
\mathcal{G} &= \pi^2 \left(\frac{l^2}{L_x^2} + \frac{k^2}{L_y^2} \right) \underline{A} - \underline{B} \\
&= \begin{bmatrix} \frac{-\phi h_{fg}}{\beta_1} & 0 & 0 \\ 0 & 0 & 0 \\ 0 & 0 & \frac{-\phi h_{fg}}{\beta_2} \end{bmatrix} \\
&= \begin{bmatrix} \frac{\phi h_{fg}}{\beta_1} \\ 0 \\ \frac{\phi h_{fg}}{\beta_2} \end{bmatrix} \frac{[1 \ 0 \ 1]}{\left(\frac{\lambda \rho h_{vap}^3}{12 \mu \phi} \pi^2 \left(\frac{l^2}{L_x^2} + \frac{k^2}{L_y^2} \right) + 2 \right)}
\end{aligned} \tag{6.47}$$

The left hand side of Eq. (6.45) is a 2D Fourier series. The coefficients of a 2D Fourier series are computed using

$$\begin{aligned}
\underline{b}_{lk} &= \frac{\delta_{lk}}{L_x L_y} \int_0^{L_y} \int_0^{L_x} \begin{bmatrix} \frac{q_{in}''}{\beta_1} \\ 0 \\ \frac{h T_\infty}{\beta_2} \end{bmatrix} \cos\left(\frac{l\pi x}{L_x}\right) \cos\left(\frac{k\pi y}{L_y}\right) dx dy, \\
\delta_{lk} &= 4 \text{ for } l > 0 \text{ and } k > 0 \\
\delta_{lk} &= 2 \text{ for } l = 0 \text{ and } k > 0 \text{ or } l > 0 \text{ and } k = 0 \\
\delta_{lk} &= 1 \text{ for } l = 0 \text{ and } k = 0
\end{aligned} \tag{6.48}$$

Eq. (6.46) is solved by discretizing it in time using a backward difference approximation. Thus,

$$\begin{aligned}
\underline{b}_{lk}^{n+1} &= \frac{\underline{a}_{lk}^{n+1} - \underline{a}_{lk}^n}{\Delta t} + \mathcal{G} \underline{a}_{lk}^{n+1} \\
&\text{by rearranging terms,} \\
\underline{a}_{lk}^{n+1} &= (I_3 + \Delta t \mathcal{G})^{-1} (\Delta t \underline{b}_{lk}^{n+1} + \underline{a}_{lk}^n)
\end{aligned} \tag{6.49}$$

where n is the time step number. The initial values of \underline{a}_{lk} are computed based on the temperature at time zero.

$$\underline{a}_{lk}^0 = \frac{\delta_{lk}}{L_x L_y} \int_0^{L_y} \int_0^{L_x} \begin{bmatrix} \bar{T}_1^0 \\ \bar{T}_{vap}^0 \\ \bar{T}_2^0 \end{bmatrix} \cos\left(\frac{l\pi x}{L_x}\right) \cos\left(\frac{k\pi y}{L_y}\right) dx dy \quad (6.50)$$

where \bar{T}_1^0 , \bar{T}_{vap}^0 , and \bar{T}_2^0 are the initial temperatures.

At each time step, using the known boundary heat flux at the evaporator, Eq. (6.48) is solved to obtain \underline{b}_{lk} . This is used to solve the time stepping Eq. (6.49) to obtain \underline{a}_{lk} . The computed \underline{a}_{lk} value is used to compute c_{lk} using Eq. (6.44). Once these coefficients are obtained, the temperature field in the vapor chamber and the saturation temperature in the vapor core can be computed. The pressure and velocity fields can then be computed.

6.1.7 Wick Hydrodynamics

The continuity and momentum equations in the wick zones are combined to compute the wick pressure field. The momentum equation in the wick (Eq. (6.24)) combined with the continuity equation (Eq. (6.1)) yields equations for the pressure in the evaporator-side and condenser-side wicks, respectively, as

$$\begin{aligned} \left(\frac{\partial^2 P_{wick,1}}{\partial x^2} + \frac{\partial^2 P_{wick,1}}{\partial y^2} \right) &= \frac{\dot{m}_1'' \mu}{\rho K_{wick,1} h_{wick,1}} \\ \left(\frac{\partial^2 P_{wick,2}}{\partial x^2} + \frac{\partial^2 P_{wick,2}}{\partial y^2} \right) &= \frac{\dot{m}_2'' \mu}{\rho K_{wick,2} h_{wick,2}} \end{aligned} \quad (6.51)$$

Setting $P_{sum} = P_{wick,1} + P_{wick,2}$ and $P_{diff} = P_{wick,1} - P_{wick,2}$, Eq. (6.51) yields

$$\begin{aligned} \left(\frac{\partial^2 P_{sum}}{\partial x^2} + \frac{\partial^2 P_{sum}}{\partial y^2} \right) &= \frac{\dot{m}_1'' \mu}{\rho K_{wick,1} h_{wick,1}} + \frac{\dot{m}_2'' \mu}{\rho K_{wick,2} h_{wick,2}} \\ \left(\frac{\partial^2 P_{diff}}{\partial x^2} + \frac{\partial^2 P_{diff}}{\partial y^2} \right) &= \frac{\dot{m}_1'' \mu}{\rho K_{wick,1} h_{wick,1}} - \frac{\dot{m}_2'' \mu}{\rho K_{wick,2} h_{wick,2}} \end{aligned} \quad (6.52)$$

Based on the boundary conditions given by Eq. (6.8) and the wick momentum Eq. (6.24), the boundary conditions for P_{sum} and P_{diff} are

$$\begin{aligned}
&\text{at } x = 0 \text{ and } x = L_x, u_{sum} = 0 = \frac{\partial P_{sum}}{\partial x}; P_{diff} = 0 \\
&\text{at } y = 0 \text{ and } y = L_y, v_{sum} = 0 = \frac{\partial P_{sum}}{\partial y}; P_{diff} = 0
\end{aligned} \tag{6.53}$$

where $u_{sum} = u_{wick,1} + u_{wick,2}$ and $u_{diff} = u_{wick,1} - u_{wick,2}$. To solve the Laplacians in Eq. (6.52), 2D Fourier series substitutions are used.

$$\begin{aligned}
P_{sum} &= \sum_{l=0}^{\infty} \sum_{k=0}^{\infty} \left(d_{sum,lk} \cos\left(l\pi \frac{x}{L_x}\right) \cos\left(k\pi \frac{y}{L_y}\right) \right) \\
P_{diff} &= \sum_{l=0}^{\infty} \sum_{k=0}^{\infty} \left(d_{diff,lk} \sin\left(l\pi \frac{x}{L_x}\right) \sin\left(k\pi \frac{y}{L_y}\right) \right)
\end{aligned} \tag{6.54}$$

satisfy the boundary conditions in Eq. (6.53). Substituting into Eq. (6.52) yields

$$\begin{aligned}
&-\sum_{l=0}^{\infty} \sum_{k=0}^{\infty} \left(d_{sum,lk} \pi^2 \left(\left(\frac{l}{L_x} \right)^2 + \left(\frac{k}{L_y} \right)^2 \right) \right) \\
&\quad \cos\left(l\pi \frac{x}{L_x}\right) \cos\left(k\pi \frac{y}{L_y}\right) \\
&= \frac{\dot{m}_1'' \mu}{\rho K_{wick,1} h_{wick,1}} + \frac{\dot{m}_2'' \mu}{\rho K_{wick,2} h_{wick,2}} \\
&-\sum_{l=0}^{\infty} \sum_{k=0}^{\infty} \left(d_{diff,lk} \pi^2 \left(\left(\frac{l}{L_x} \right)^2 + \left(\frac{k}{L_y} \right)^2 \right) \right) \\
&\quad \cos\left(l\pi \frac{x}{L_x}\right) \cos\left(k\pi \frac{y}{L_y}\right) \\
&= \frac{\dot{m}_1'' \mu}{\rho K_{wick,1} h_{wick,1}} - \frac{\dot{m}_2'' \mu}{\rho K_{wick,2} h_{wick,2}}
\end{aligned} \tag{6.55}$$

Using the formula for the coefficients of a 2D Fourier series yields

$$\begin{aligned}
d_{sum, lk} &= \frac{\delta_{lk} \int_0^{L_y} \int_0^{L_x} \left(\left(\frac{\dot{m}_1'' \mu}{\rho K_{wick,1} h_{wick,1}} + \frac{\dot{m}_2'' \mu}{\rho K_{wick,2} h_{wick,2}} \right) \cos\left(\frac{l\pi x}{L_x}\right) \cos\left(\frac{k\pi y}{L_y}\right) \right) dx dy}{-\pi^2 \left(\left(\frac{l}{L_x}\right)^2 + \left(\frac{k}{L_y}\right)^2 \right) L_x L_y} \\
d_{diff, lk} &= \frac{4 \int_0^{L_y} \int_0^{L_x} \left(\left(\frac{\dot{m}_1'' \mu}{\rho K_{wick,1} h_{wick,1}} - \frac{\dot{m}_2'' \mu}{\rho K_{wick,2} h_{wick,2}} \right) \cos\left(\frac{l\pi x}{L_x}\right) \cos\left(\frac{k\pi y}{L_y}\right) \right) dx dy}{-\pi^2 \left(\left(\frac{l}{L_x}\right)^2 + \left(\frac{k}{L_y}\right)^2 \right) L_x L_y} \tag{6.56}
\end{aligned}$$

The velocity fields in the wick can then be computed using the governing momentum equation (6.24).

6.1.8 Model Implementation

A time-stepping based model is developed for the vapor chamber transport that computes the 3D fields of temperature in the vapor chamber, as well as the pressure and velocity fields in the wick and the vapor core. The temperature-dependent thermophysical properties of the fluid are computed at each time step based on the volume-averaged temperature for the corresponding zone. The infinite-series sums in the model are truncated to finite sums whose number is chosen such that adding another term does not change the magnitude significantly.

$$sum = \sum_{i=0}^{\infty} var_i \approx \sum_{i=0}^N var_i \tag{6.57}$$

where *var* is the summand of the series.

It is important to note that using a time-discretized solution method allows for the use of temperature-dependent properties for the vapor phase. The vapor phase properties can be expected to change considerably over the range of typical operating temperatures (from the initial ambient to full-power operation), and thus temperature-dependent properties are necessary for achieving

reasonable accuracy of the model. Combining analytical and time-discretized solution methods in this manner allows for a low-computational cost without sacrificing accuracy.

6.2 Estimation of Model Accuracy

The accuracy of the time-stepping analytical model depends on the validity of the assumptions underlying each of the simplifications to the governing equations. The Appendix B describes an estimate of the errors in the temperature and pressure fields computed by the model as a result of the simplifying assumptions for a range of vapor chamber thicknesses and input power. Based on this analysis, the following three assumptions were found to cause the largest errors in the temperature and pressure fields across the simulated cases: (1) assuming a negligible temperature difference across the thickness of the wall and the wick on the evaporator side (Eq. (31)); (2) linearizing the Clausius-Clapeyron equation (Eq. (38)); and (3) neglecting convection in the momentum equation in the vapor core (Eq. (17)).

As detailed in Appendix B, at the most extreme working thickness and operating power, the relative error in the maximum temperature drop is only 30%; for most of the simulated cases, the error is under 10%. Similarly, the total pressure drop in the vapor chamber is generally predicted with good accuracy. Thus the model has excellent accuracy in computing the maximum temperature drop and total pressure drop in a vapor chamber over a wide range of thicknesses and powers.

6.3 Results

6.3.1 Model Validation

The predictions of the time-stepping analytical vapor chamber model developed in this work are validated against a numerical model for the same geometry, materials, and boundary conditions. This benchmark numerical model is the finite-volume-based vapor chamber model described in Ref. [53] (without the microscale model corrections to the evaporation rate and interfacial area). Two validation cases were simulated comparing the time-stepping analytical model against the benchmark numerical model for the same geometry and boundary conditions as described in Figure 6.2; Figure 6.2a shows Case #1 and Figure 6.2b shows Case #2. For both cases, the vapor chamber has copper walls with a uniform layer of sintered copper wick on the inner

surface of the walls. The length and width of the vapor chamber are $L_x = 90$ mm and $L_y = 55$ mm, respectively. The thickness of the walls are $h_{wall,1} = h_{wall,2} = 0.2$ mm. The thickness of the wicks in Case #1 are $h_{wick,1} = h_{wick,2} = 37$ μm , and in Case #2 are $h_{wick,1} = h_{wick,2} = 120$ μm . The thickness of the vapor core in Case #1 is $h_{vap} = 26$ μm , and in Case #2 is $h_{vap} = 360$ μm . Water is used as the working fluid. The properties of the working fluid, copper, and porous wick materials are shown in Table 6.2. The vapor chamber is initially at a uniform temperature of 300 K. Starting at $t = 0$ s, the vapor chamber receives a heat input power 10 W for Case #1 and 160 W for Case #2, applied over a square area of 1 cm^2 at the center of the evaporator side; the rest of the evaporator-side face is insulated. The opposing condenser side experiences a convective boundary condition with a heat transfer coefficient of $75\text{ W/m}^2\text{K}$ for Case #1 and of $1200\text{ W/m}^2\text{K}$ for Case #2, and an ambient temperature of 300 K. The sides of the vapor chamber are insulated.

The time-stepping analytical model is solved using the commercial software MATLAB [16]; the temperature-dependent properties of the water vapor are obtained using the commercial software REFPROP [17]. Each infinite-series summation is truncated to 40 terms. The finite-volume numerical vapor chamber model is implemented in the commercial software FLUENT [40]; the vapor chamber geometry is discretized into a rectangular grid with 540,000 cells. The complete transient behavior of Case #1 was simulated using variable time-steps in the range of 0.1 s to 2 s. Case #2 was simulated to obtain a comparison at steady-state, using the steady-state-seeking solution algorithm described in Section 4.1.2. The simulation with the time-stepping analytical model uses a time step of 0.1 s for both the simulations.

The temperature fields predicted by the two different modeling approaches for Case #1 are shown in Figure 6.3. Figure 6.3a shows the spatial temperature variation, while Figure 6.3b shows the temporal temperature variation. Figure 6.3a shows the spatial temperature variation along two lines on the evaporator-side ($z = 0$ mm, $y = 27.5$ mm) and condenser-side ($z = 0.5$ mm, $y = 27.5$ mm) vapor chamber faces at $t = 44.5$ s. The temperature profile has a maximum temperature at $x = 45$ mm for both the curves and decreases in both directions away from the center. A temperature difference between the evaporator and condenser sides is also apparent from the plots. The plots reveal a good match between the two simulations for the prediction of spatial temperature variation; the relative error in the total temperature drop in the vapor chamber is 0.075. In Section 6.2, it was estimated that the temperature field would have no error due to the linearization of the Clausius-Clapeyron equation, but would primarily manifest as an error in the pressure field. We

note here that the linearization of the Clausius-Clapeyron equation does lead to an error in the temperature field, albeit one that is small compared to the effect on the pressure field. Figure 6.3b shows the temporal variation of maximum temperature in the vapor chamber, which increases with time due to the heat input applied to vapor chamber; the predictions with the two approaches again match very well.

Figure 6.4 shows the pressure fields in the wicks (Figure 6.4a) and the vapor core (Figure 6.4b) at $t = 44.5$ s on the cross-sectional plane ($y = 27.5$ mm) shown in Figure 6.2, for Case #1. The pressure values in both the plots are offset from the absolute pressure such that the relative pressure value is zero at $x = 0$ mm and $x = 90$ mm. The pressure in the wick is highest at the center of the condenser-side wick and reduces outward in the direction of liquid flow. Once the liquid returns to the evaporator side at the peripheries the pressure reduces as liquid flows toward the center of the heated region. The pressure in the vapor core is highest at the center where vapor is generated in the vicinity of the heat input and reduces in the outward direction of vapor flow. The plot reveals a good match between the two simulations for the relative pressure in the wick and the vapor core, except near the heat input. Section 6.2 estimated that the error for this case would be mainly due to use of the linearized Clausius-Clapeyron relation and should appear in the vapor core pressure. The vapor core pressure plots show this predicted error; the error in the pressure gradients is high near the heat input zone, where the pressure is noticeably higher than the average pressure in the vapor core. The wick pressure plot also shows a slight mismatch near the heat input, on the evaporator side. This mismatch is due to a change in the local evaporated mass flux corresponding to the differences in the vapor core pressure field. The relative error in the total pressure drop in the wick is 0.096, which matches the value predicted by the error estimation analysis (0.095).

The steady-state temperature fields predicted by the two modeling approaches for Case #2 are shown in Figure 6.5. The temperature profiles are shown along two lines on the evaporator-side ($z = 0$ mm, $y = 27.5$ mm) and condenser-side ($z = 1$ mm, $y = 27.5$ mm) vapor chamber faces. The temperature profiles have a maximum temperature at $x = 45$ mm and decrease in both directions away from the center. Unlike Case #1, the temperature variation on the condenser side is negligible compared to that on the evaporator side. The reason is that the comparatively thick vapor core leads to a very small vapor core resistance as compared to the resistance due to phase change across the vapor core. The relative error in the total temperature drop in the vapor chamber is 0.08, which is lower than the value estimated in the previous section (0.21), albeit in the opposite

direction. This is because the thermal convection in the vapor core (which is neglected in the simplified governing equation) reduces the resistance due to phase change; this indirect error cannot be accounted for using the methods employed in Section 6.2.

Figure 6.6 shows the pressure fields in the wicks (Figure 6.6a) and the vapor core (Figure 6.6b) at steady state on the cross-sectional plane ($y = 27.5$ mm) shown in Figure 6.2, for Case #2. The pressure values in both the plots are offset from the absolute pressure such that the relative pressure value at $x = 0$ mm and $x = 90$ mm is zero. The pressure profiles in the wick and the vapor core have a similar trend as observed in Case #1. The vapor core pressure predicted by the time-stepping analytical model deviates from the simulation with the finite-volume based numerical model, which is attributed to neglecting the convection term in the momentum equation in the vapor core, as discussed in Section 6.2. The wick pressure plot also shows a mismatch near the heat input on the evaporator side. This mismatch is due to the change in the local evaporated mass flux associated with the differences in the vapor core pressure field. The relative error in the total pressure drop in the wick is 0.086, which matches the value predicted by the error estimation analysis (0.095).

The errors in the temperature and pressure profiles of the time-stepping analytical model are remarkably low, both in time and space, considering the significantly reduced computational cost. For Case#1, the computational time for the finite-volume numerical simulation, on a supercomputer node (Xeon-E5, Intel) using 15 parallel processes, is 319 hr. The computational time is reduced to 0.4 hr for the time-stepping analytical model running on a desktop computer, which is a reduction of 3 orders of magnitude.

6.3.2 Time-Stepping Analytical Model Simulation with Multiple Time-Varying Heat Inputs

The time-stepping analytical model is demonstrated for a case where the vapor chamber is subjected to multiple time-varying heat inputs. For this case, the vapor chamber uses the same materials and properties as the previous case (Table 6.2), with a modified geometry. The length and width of the vapor chamber are $L_x = 80$ mm and $L_y = 60$ mm, respectively. The wall thicknesses are $h_{wall,1} = h_{wall,2} = 0.2$ mm, with wick thicknesses of $h_{wick,1} = h_{wick,2} = 30$ μm and a vapor core thickness of $h_{vap} = 40$ μm . The vapor chamber is initially at a uniform temperature of 300 K. Starting at $t = 0$ s, it is subjected to two heat inputs (Heaters A and B) of 0.5 W each over separate square areas of 1 cm^2 at the locations identified in Figure 6.7. At $t = 50$ s, Heater B is switched off

(0 W) and Heater A remains on at 0.5 W. The rest of the evaporator-side face is insulated. A convective boundary condition, with heat transfer coefficient $15 \text{ W/m}^2\text{K}$ and ambient temperature of 300 K, is imposed on the opposing condenser-side face. The sides of the vapor chamber are insulated. In the time-stepping analytical solution, the simulation truncates each infinite-series summation to 40 terms, and is run for 100 time steps of 1 s each.

Results for the temperature field from the time-stepping analytical solution are shown in Figure 6.8. Figure 6.8a shows the temporal variation of the maximum temperature at the center of both heat inputs. The maximum temperatures of Heater A and Heater B both increase at a similar rate upon the initial imposition of 0.5 W heat inputs to each. Heater B is switched off at $t = 50 \text{ s}$, and the temperature at this location decreases suddenly. After $t = 53 \text{ s}$, the temperatures at both Heaters A and B increase due to the heat input at Heater A, albeit at a lower rate than before $t = 50 \text{ s}$, due to the lower total heat input. A video with the 3D and transient contours of temperature is included in the Supplementary Materials of the publication [50] (snapshot in Figure 6.8b) Figure 6.8c and Figure 6.8d show the temperature contours on the vapor chamber condenser-side outer surface at $t = 33 \text{ s}$ and 66 s , respectively. The contours at $t = 33 \text{ s}$ reveal the non-uniform temperature field that results from the two localized heat inputs. The temperature at Heater B is higher than at Heater A, despite the heaters having the same input power and size, because Heater B is closer to the edges of the vapor chamber. The contours at $t = 66 \text{ s}$ only shows only one hotspot, which corresponds to Heater A, since Heater B is switched off at $t = 50 \text{ s}$. The simulation is able to capture the transient thermal response of a vapor chamber to multiple time-varying heat inputs.

6.4 Conclusions

A transient model for vapor chamber operation was developed that allows for multiple, arbitrarily shaped, time-varying heat inputs on the evaporator-side face; the model predicts 3D fields of temperature, pressure, and velocity in the vapor chamber. The governing mass, momentum, and energy equations in the wall, wick, and vapor core domains were simplified based on a scaling analysis and assuming temperature profiles across the thickness of each zone. The simplified linear differential equations were solved using a combination of analytical and time-discretized methods. The errors introduced into the temperature and pressure fields computed by the time-stepping analytical model due to the simplifying assumptions employed in the model development were estimated. The model has low errors for cases from low- to high-power

applications (less than 10% for a majority of the simulated cases). The model is validated against a finite-volume-based numerical model for two cases, one for a low-power application and another for a high-power application. Based on this validation case, the newly developed time-stepping analytical model was demonstrated to have 3-4 orders of magnitude lower computational cost compared to the numerical model while maintaining good physical accuracy. This model was then used to simulate the behavior of a vapor chamber subjected to multiple, time-varying heat input boundary conditions to demonstrate the capability of the time-stepping analytical model to resolve the transient 3D thermal response to complex boundary conditions expected in real-world applications.

Nomenclature

$\underline{A}, \underline{B}$	matrix containing thermophysical and geometric properties
\underline{b}_k	coefficients of 2D Fourier series [K s^{-1}]
\underline{C}	vector source term [K s^{-1}]
$\underline{a}_k, \underline{c}_k$	coefficients of 2D Fourier series [K]
CN_{CC}	condition number for linearizing the Clausius-Clapeyron equation
CN_{conv}	condition number for assuming negligible convection in the momentum equation in the vapor core
CN_T	condition number for assuming negligible temperature difference across the thicknesses of the wall and the wick on the evaporator side
$d_{sum, lk}$	coefficients of 2D Fourier series [Pa]
$d_{diff, lk}$	
d_p	wick particle diameter [m]
ρC_p	volumetric specific heat capacity [$\text{J kg}^{-1} \text{K}^{-1}$]
h	convection coefficient [$\text{W m}^{-2} \text{K}^{-1}$]
h_{fg}	specific enthalpy of vaporization [J kg^{-1}]
h_{vap}	thickness of vapor core [m]
$h_{wall, 1}$	thickness of evaporator-side wall [m]
$h_{wall, 2}$	thickness of condenser-side wall [m]
$h_{wick, 1}$	thickness of evaporator-side wick 1 [m]
$h_{wick, 2}$	thickness of condenser-side wick 2 [m]
K	permeability of the porous medium [m^2]
k	thermal conductivity [$\text{W m}^{-1} \text{K}^{-1}$]
k_{eff}	porous medium effective thermal conductivity [$\text{W m}^{-1} \text{K}^{-1}$]
L_x	length of the vapor chamber in x direction [m]
L_y	width of the vapor chamber in y direction [m]
l, k	indices of summations in the 2D Fourier series [-]
\dot{m}''	mass flux rate due to phase change [$\text{kg m}^{-2} \text{s}^{-1}$]
N	number of terms in truncated infinite series
P	pressure [Pa]
P_{cap}	capillary pressure [Pa]

P_o	saturation pressure corresponding to the volume-averaged vapor core temperature [Pa]
Pr	Prandtl number $\left(\frac{\mu}{\rho\alpha}\right)$ [-]
q''_{in}	external boundary heat flux [W m ⁻²]
R	specific gas constant [J kg ⁻¹ K ⁻¹]
Re	Reynolds number $\left(\frac{\rho UL}{\mu}\right)$ [-]
T	temperature [K]
\bar{T}	z -averaged temperature [K]
T_{sat}	saturation temperature [K]
T_∞	ambient temperature [K]
t	time [s]
u	x -component of velocity [m s ⁻¹]
\vec{V}	velocity vector [m s ⁻¹]
v	y -component of velocity [m s ⁻¹]
w	z -component of velocity [m s ⁻¹]
x	x -coordinate (length) direction [m]
y	y -coordinate (width) direction [m]
z	z -coordinate (thickness) direction [m]

Greek

α	thermal diffusivity ($k_{eff}/(\rho C_p)_{eff}$) [m ² s ⁻¹]
γ	surface tension [Pa s]
ε_{CC}	relative error in the pressure field due to linearization of the Clausius-Clapeyron equation
ε_{conv}	relative error in the pressure field due to neglecting convection in the momentum equation in the vapor core
ε_T	relative error in the temperature field due to neglecting temperature difference across the thicknesses of the wall and the wick on the evaporator side
Θ	vector of temperature field variables [K]

λ	constant $\left(\frac{h_{fg} P_o}{R (T_{sat})_{mean}^2} \right)$ [Pa K ⁻¹]
μ	viscosity [Pa s]
ρ	density [kg m ⁻³]
σ	accommodation coefficient [-]
φ	constant $\left(\frac{2\sigma}{2-\sigma} \frac{h_{fg} \rho_{vap}}{(T_{vap})_{mean}^{1.5}} \left(\frac{1}{2\pi R} \right)^{0.5} \right)$ [kg m ⁻² s ⁻¹ K ⁻¹]
ϕ	porosity [-]

Subscript

<i>int</i>	wick–vapor interface
<i>sum</i>	wick 1 plus wick 2
<i>diff</i>	wick 1 minus wick 2
<i>vap</i>	corresponding to the vapor core
<i>wall</i>	corresponding to the wall
<i>wick</i>	corresponding to the wick
<i>x</i>	along <i>x</i> coordinate direction
<i>y</i>	along <i>y</i> coordinate direction
<i>z</i>	along <i>z</i> coordinate direction
<i>1</i>	corresponding to the evaporator side
<i>2</i>	corresponding to the condenser side

Superscript

<i>n</i>	time step
<i>0</i>	initial condition

Vector notation

–	Vector
~	Matrix

Table 6.1. Scales for the model variables.

Variable	Scale
t	τ
x	L_x
y	L_y
z in vapor core	h_{vap}
z in wick 1	$h_{wick,1}$
z in wick 2	$h_{wick,2}$
z in wall 1	$h_{wall,1}$
z in wall 2	$h_{wall,2}$
u in vapor core	U_{vap}
v in vapor core	V_{vap}
w in vapor core	W_{vap}
u in wick 1	$U_{wick,1}$
v in wick 1	$V_{wick,1}$
w in wick 1	$W_{wick,1}$
u in wick 2	$U_{wick,2}$
v in wick 2	$V_{wick,2}$
w in wick 2	$W_{wick,2}$

Table 6.2. Properties of the working fluid, copper, and porous wick materials used in the vapor chamber simulations. Vapor properties are shown at a temperature of 300 K.

Property	Value
Copper density (ρ)	8978 kg/m ³
Water liquid density (ρ)	998.2 kg/m ³
Water vapor density (ρ)	0.02 kg/m ³
Copper thermal conductivity (k_{eff})	387.6 W/mK
Wick effective thermal conductivity (k_{eff})	40 W/mK
Water vapor thermal conductivity (k_{eff})	0.0187 W/mK
Copper specific heat capacity (C_P)	381 J/kgK
Water liquid specific heat capacity (C_P)	4182 J/kgK
Water vapor specific heat capacity (C_P)	1889 J/kgK
Water liquid viscosity (μ)	1.79×10^{-5} Pa s
Water vapor viscosity (μ)	1×10^{-3} Pa s
Enthalpy of vaporization (h_{fg})	2.446×10^6 J/kg
Water vapor specific gas constant (R)	462 J/kgK
Wick porosity (ϕ)	0.6
Wick permeability (K)	$\frac{\phi^3 h_{wick}^2}{1350(1-\phi)^2}$
Capillary pressure (P_{cap})	$\frac{2\gamma}{0.07 h_{wick}}$

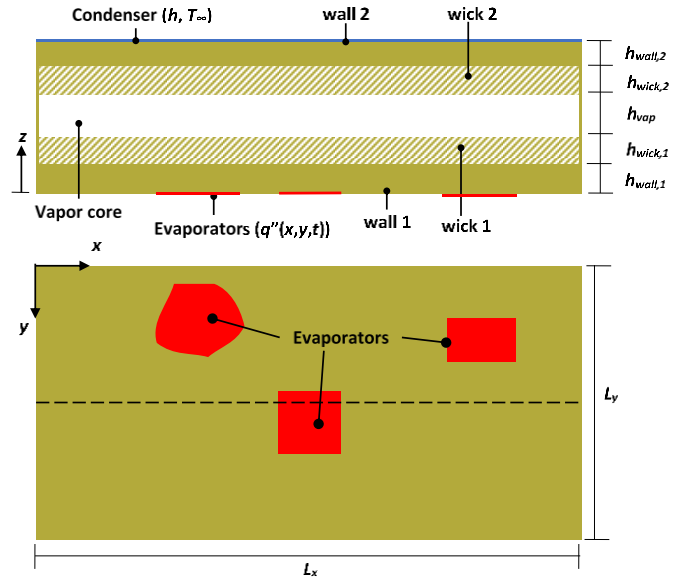


Figure 6.1. Vapor chamber transport model geometry and boundary conditions (cross-section and bottom views).

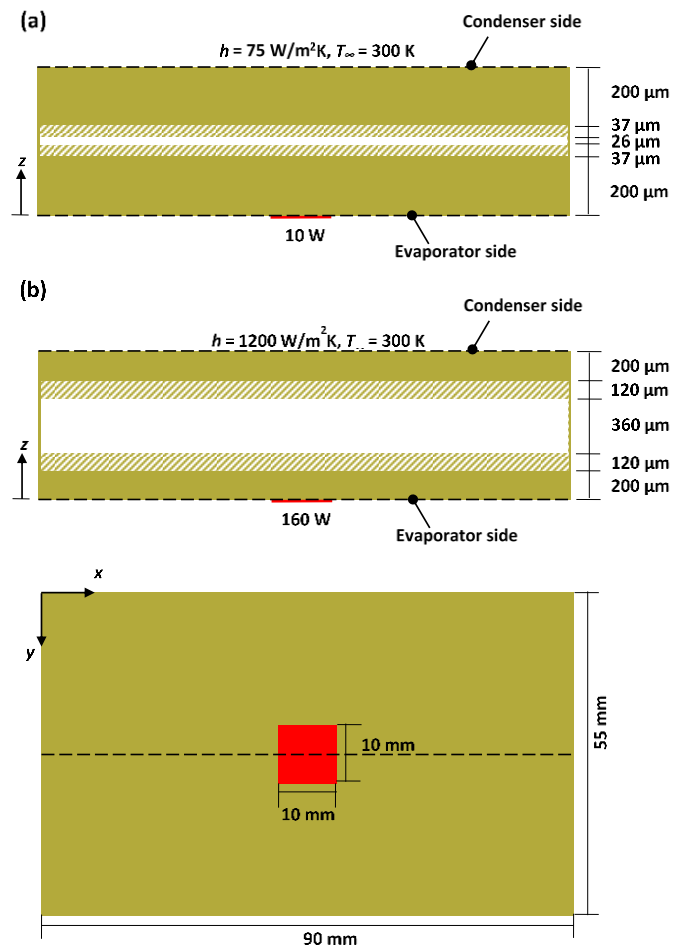


Figure 6.2. Schematic diagram of the simulated geometry and boundary conditions used to validate the time-stepping analytical vapor chamber model, showing a bottom view at the bottom and cross-section at the top for (a) Case #1 (thickness scaled $50\times$), and (b) Case #2 (thickness scaled $25\times$).

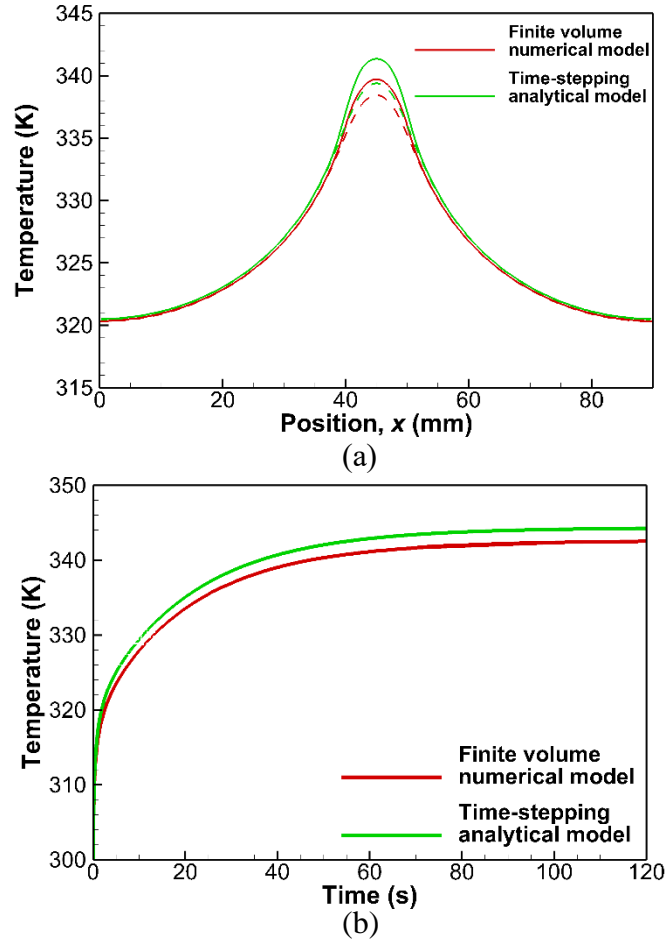


Figure 6.3. Comparison of temperature results from vapor chamber simulations using the time-stepping analytical model and the finite-volume numerical model for Case #1. (a) The temperature profile is shown along the evaporator-side outer surface (solid lines; $z = 0$ mm, $y = 27.5$ mm) and the condenser-side outer surface (dashed lines; $z = 0.5$ mm, $y = 27.5$ mm), at $t = 44.5$ s. (b) The variation of the maximum temperature in the vapor chamber (at $z = 0$ mm, $x = 45$ mm, $y = 27.5$ mm) with time predicted by the two models is compared.

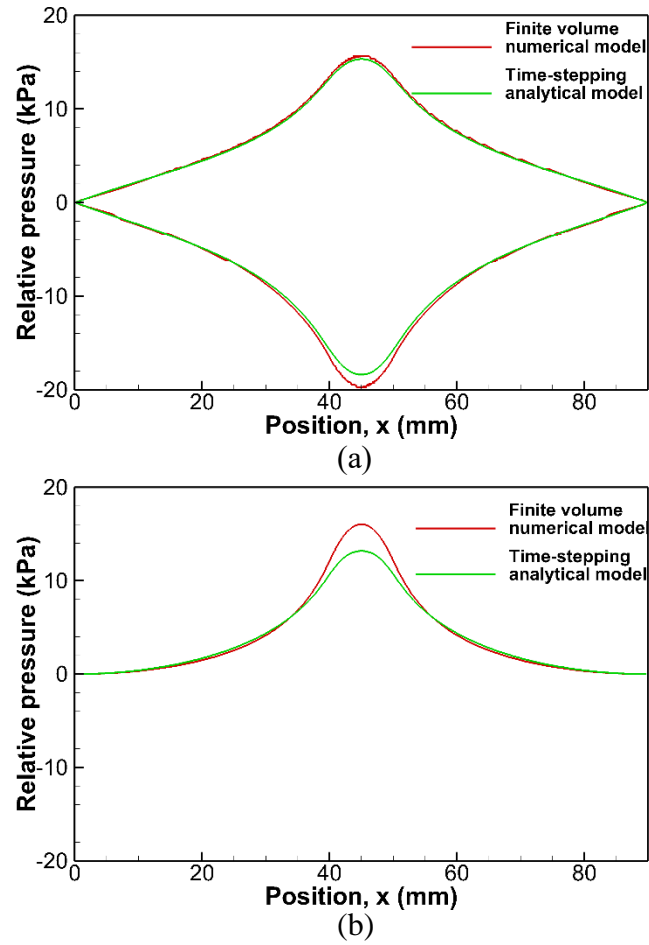


Figure 6.4. Comparison of pressure results from the vapor chamber simulations using the time-stepping analytical model and the finite-volume numerical model for Case #1. The relative pressure variation in the (a) wick and (b) vapor core are shown for the cross-sectional plane $y = 27.5$ mm at $t = 44.5$ s.

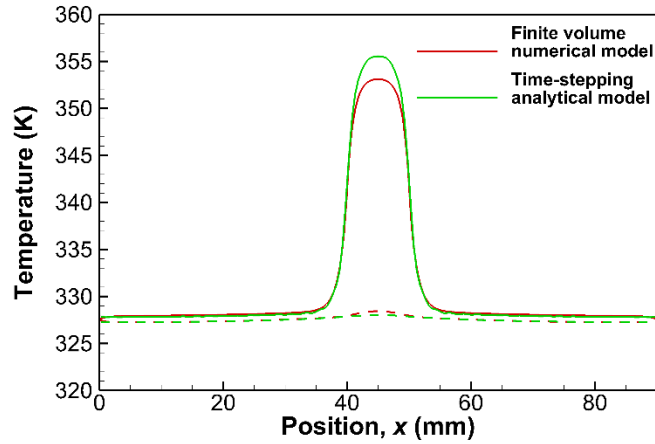


Figure 6.5. Comparison of the temperature profile along the evaporator-side outer surface (solid lines; $z = 0$ mm, $y = 27.5$ mm) and the condenser-side outer surface (dashed lines; $z = 1$ mm, $y = 27.5$ mm), at steady-state is shown, from vapor chamber simulations using the time-stepping analytical model and the finite-volume numerical model for Case #2.

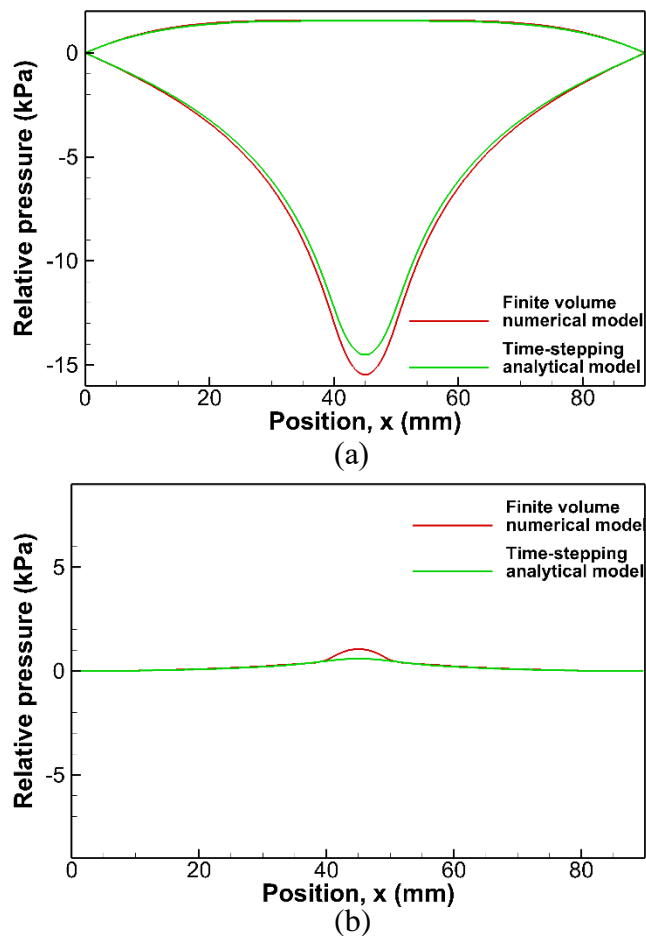


Figure 6.6. Comparison of pressure results from the vapor chamber simulations using the time-stepping analytical model and the finite-volume numerical model for Case #2. The relative pressure variation in the (a) wick and (b) vapor core are shown for the cross-sectional plane $y = 27.5$ mm at steady state.

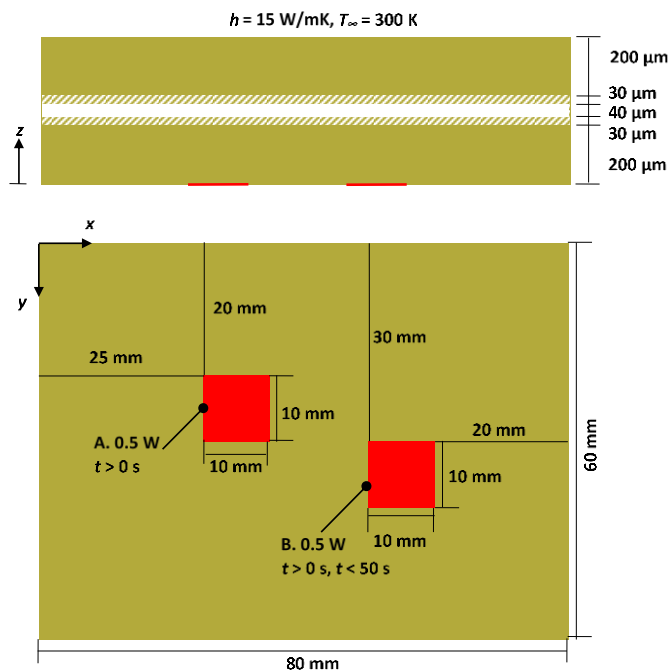


Figure 6.7. Schematic diagram of the geometry and boundary conditions used to simulate multiple time-varying inputs with the time-stepping analytical vapor chamber model (thickness scaled $45\times$).

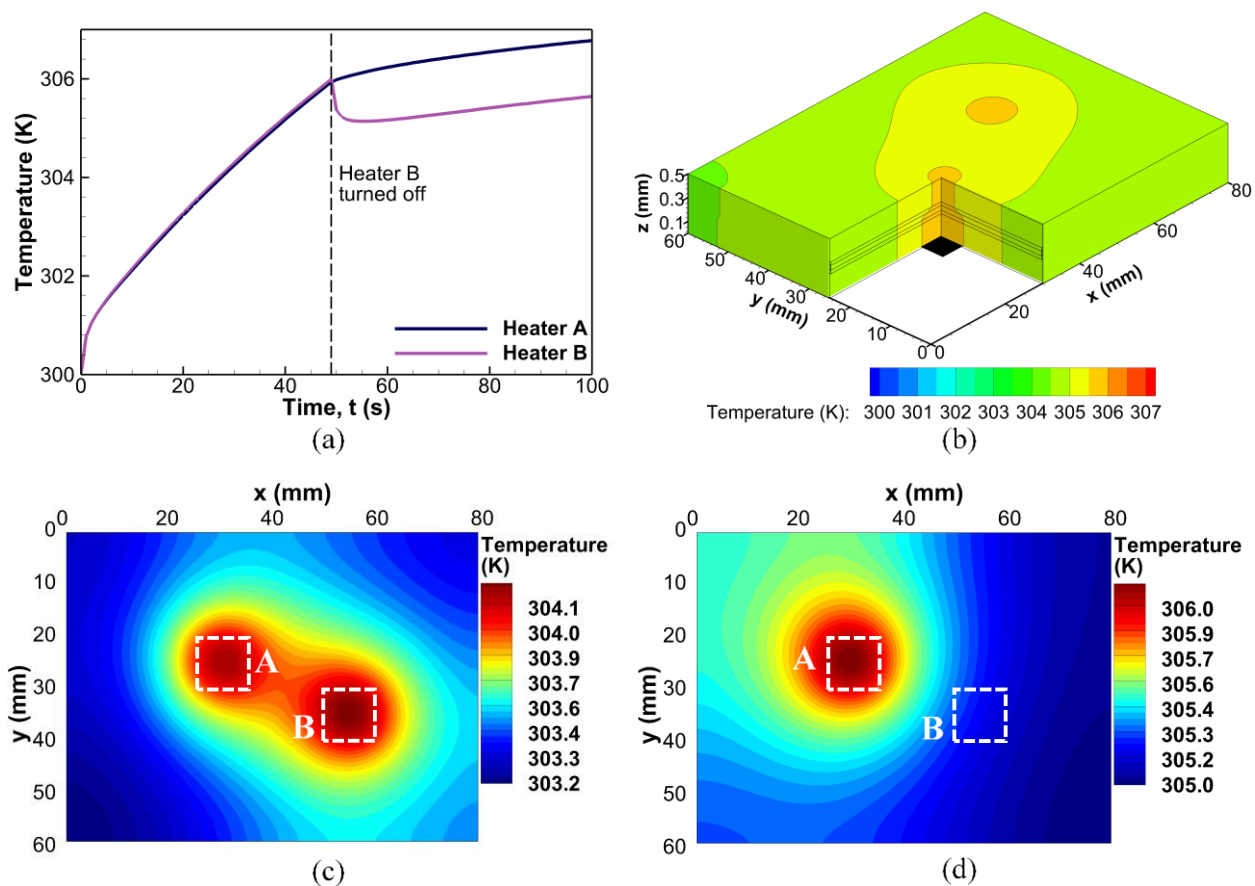


Figure 6.8. Time-stepping analytical solution of the (a) maximum temperature at the centers of the two heaters with time; (b) snapshot at $t = 47$ s showing the 3D contours of temperature in the vapor chamber, with z -direction scaled $20\times$ (video in Supplementary Materials of the publication [50]) played at $5\times$ real-time speed) and temperature contours on the condenser-side outer surface ($z = 0.5$ mm) at (c) $t = 33$ s and (d) $t = 66$ s.

7. ON THE TRANSIENT THERMAL RESPONSE OF THIN VAPOR CHAMBER HEAT SPREADERS: GOVERNING MECHANISMS AND PERFORMANCE RELATIVE TO METAL SPREADERS

In this chapter, the time-stepping analytical model for vapor chamber transport developed in Chapter 6 is used to simulate the transient behavior of a vapor chamber and a solid copper heat spreader. Comparison of the temporal temperature fields in the two devices is used to identify and understand the key mechanisms that govern the transient behavior and performance of vapor chambers. Experiments are conducted with a commercial vapor chamber and compared to predictions from the model to demonstrate the key governing mechanisms identified. Lastly, the transient performance of a vapor chamber relative to a copper heat spreader of the same external dimensions is explored as a function of two key parameters, namely the heat spreader thickness and input power. Thresholds are identified beyond which the vapor chamber offers improved performance relative to the copper heat spreader. The relationship between the key governing mechanisms and the transient performance thresholds is established. The material in this chapter has been submitted to a journal and is in review [54].

7.1 Mechanisms Governing Vapor Chamber Transient Behavior

7.1.1 Numerical Simulation Case Details

A vapor chamber and a copper spreader of identical external geometry are simulated to observe their transient response to a step heat input. A comparison of these two cases is used to obtain insight into the mechanisms governing the behavior of the vapor chamber.

Heat spreading in a vapor chamber can occur through vapor spreading in the vapor core, heat diffusion in the wick, and heat diffusion in the solid walls. The heat diffusion in the wick is negligible compared to the other processes and hence is neglected in the model. In this demonstration, the vapor chamber has walls of negligible thickness. Taking a case where the wall thickness is negligible allows heat spreading in the vapor core, the mechanism specific to vapor chambers, to be isolated. This creates a stark contrast between the vapor chamber and the copper spreader behavior, which helps in distinguishing the unique mechanisms governing the transient

response of the vapor chamber from the commonly understood mechanism of thermal diffusion in solids.

The geometry and boundary conditions of the simulated vapor chamber and copper spreader are shown in Figure 7.1. The heat spreaders have a rectangular footprint with a length of 80 mm and a width of 60 mm; the total thickness is 100 μm . In the vapor chamber, the vapor core has a thickness of 40 μm , and the two wicks (evaporator-side and condenser-side) have thicknesses of 30 μm each, and span the entire footprint area. The vapor chamber has a sintered copper wick. Water is used as the working fluid. The properties of water are obtained from the commercial fluid database software REFPROP [48]. The relevant properties of the wick and copper are in Table 7.1.

The heat spreader (vapor chamber or copper) is subjected to a heat input Q of 4 W, over a 10 mm \times 10 mm square at the center of the evaporator-side face, starting at $t = 0$ s. The rest of this evaporator-side face is insulated. The opposite condenser-side face has a convective boundary condition with a convection coefficient h of 30 W/m²K and an ambient temperature T_∞ of 300 K. The heat spreader is initially ($t = 0$ s) at a temperature of 300 K. A time step of 0.2 s is used for the time-marching.

7.1.2 Analysis of The Transient Thermal Response

Figure 7.2a shows the temperature response at the center of the evaporator face relative to the ambient, for the vapor chamber and the copper spreader. This peak temperature θ_p in the domain characterizes the effective overall transient thermal resistance of the heat spreader. For the copper spreader, the peak temperature starts at $\theta_p = 0$ K at $t = 0$ s and increases gradually toward a steady state ($\theta_p = 54.2$ K at $t = 50$ s). For the vapor chamber, the temperature increases more sharply from $\theta_p = 0$ K, reaches a peak at $t = 1.8$ s, and gradually reduces toward a steady state ($\theta_p = 39.7$ K at $t = 50$ s). To understand the mechanisms underlying this non-intuitive behavior of the vapor chamber, the peak temperature response can be decomposed into the mean (volume-averaged) temperature θ_m , and the difference between the peak and mean temperatures, $\Delta\theta_{p-m} = \theta_p - \theta_m$ (*i.e.*, peak-to-mean difference).

The mean temperatures θ_m of the vapor chamber and the copper spreader, plotted in Figure 7.2b, both gradually increase from $\theta_m = 0$ K at $t = 0$ s toward a steady state. Note that at steady state, given that an equal amount of power is rejected from the condenser to the ambient in the

case of both heat spreaders via identical convective coefficients, the area-averaged condenser-surface temperature is the same for both. Also, due to the minimal temperature variation across the thickness, the mean temperature θ_m of both heat spreaders becomes nearly equal at steady state. The rate of increase of this mean temperature θ_m is governed by the mechanism identified as the *total thermal capacity* of the heat spreader; the vapor chamber temperature increases faster and reaches a steady state sooner than for the copper spreader. This reflects the lower total thermal capacity of the vapor chamber compared to the copper spreader. The total thermal capacity of the vapor chamber is a volume-weighted sum of the thermal capacities of the wick and vapor core. The volumetric thermal capacity of the wick is similar to that of pure copper ($4.17 \times 10^6 \text{ J/m}^3\text{K}$ for water and $3.42 \times 10^6 \text{ J/m}^3\text{K}$ for copper) while the thermal capacity of the vapor is negligibly small. Hence, the volume occupied by the vapor core reduces the total thermal capacity of the vapor chamber compared to a copper spreader, and the volume-averaged mean temperature θ_m of the vapor chamber increases faster than that of the copper spreader.

The peak-to-mean temperature difference ($\Delta\theta_{p-m}$) is plotted as a function of time in Figure 7.2c for both heat spreaders. For the copper spreader, this temperature difference increases up to a constant value of $\Delta\theta_{p-m} = 27 \text{ K}$ within a short time period of $t < 4.4 \text{ s}$, relative to the time to steady state for the evaporator peak temperature of $\sim 50 \text{ s}$ (Figure 7.2a). During the initial period before $t = 4.4 \text{ s}$, the spatial temperature distribution within the copper spreader is developing via heat diffusion from the heater location in the outward direction. This can be observed in Figure 7.3a, which shows the profile of the local temperature difference from the mean ($\theta - \theta_m$) along a line on the evaporator-side surface of the copper spreader (dashed line in Figure 7.1) at different times. At $t = 0.4 \text{ s}$, the initial rise in the temperature is limited to a region near the evaporator and the profile is flat (near the initial temperature) outside this region. At a later time of $t = 3.2 \text{ s}$, the temperature over the entire length of the surface changes from the initial value. After $t = 3.2 \text{ s}$, the temperature profile $\theta - \theta_m$ is invariant in time. The time required for $\theta - \theta_m$ to develop to this steady profile is governed by the mechanism identified as the *effective in-plane diffusivity* in the copper spreader, while the constant value of $\Delta\theta_{p-m} = 27 \text{ K}$ (Figure 7.2c) after the initial period is governed by its *effective in-plane conductance*. For the copper spreader, the effective in-plane diffusivity is simply the thermal diffusivity of copper and the effective in-plane conductance is proportional to the thermal conductivity of copper and the thickness of the spreader.

The peak-to-mean temperature difference $\Delta\theta_{p-m}$ of the vapor chamber (Figure 7.2c) also goes through an initial period ($t < 1.8$ s) where it rapidly increases. After this period, unlike for the copper spreader, $\Delta\theta_{p-m}$ gradually reduces with time for the vapor chamber, reaching a steady-state value at a time similar to that for the volume-averaged temperature (Figure 7.2b). Investigating the profile of the temperature $\theta - \theta_m$ on the evaporator-side of the vapor chamber in Figure 7.3b, at time $t = 0.4$ s within the initial period, the rise in the temperature is limited to a region near the evaporator and the profile is flat (near the initial temperature) outside this region, as in the case of the copper spreader. At time $t = 3.2$ s, the temperature over the entire evaporator length has changed from the initial value. The time required for $\theta - \theta_m$ to develop to such a profile is governed by the effective in-plane diffusivity of the vapor chamber. In the case of the vapor chamber, this effective-in plane diffusivity is like the ratio of the effective in-plane thermal conductivity of the vapor core and the volumetric capacity of the wick. The similarity in time taken for the development of the $\theta - \theta_m$ profile for the copper spreader and the vapor chamber indicates that they have a similar effective in-plane diffusivity for this case. However, at later times after $t = 3.2$ s, the $\theta - \theta_m$ profile (Figure 7.3b) flattens with increasing time, indicating that the effective in-plane conductance increases with time for the vapor chamber, unlike the constant value for the copper spreader. For the vapor chamber, the effective in-plane thermal conductance goes as the product of the effective in-plane thermal conductivity and the thickness of the vapor core. The effective in-plane conductivity of the vapor core is governed by the saturation pressure gradient in the vapor core due to vapor flow; the temperature dependence of the fluid properties causes the saturation pressure/temperature gradient to decrease as the mean temperature θ_m increases with time.

In summary, the above inspection of the transient temperature profiles reveals three key mechanisms governing the transient thermal behavior of a vapor chamber:

- 1) the *total thermal capacity* of the vapor chamber governs the rate of increase of the volume-averaged mean temperature, θ_m ;
- 2) the *effective in-plane diffusivity* governs the time required for the spatial temperature profile, $\theta - \theta_m$, to initially develop;
- 3) the *effective in-plane conductance* of the vapor core governs the magnitude of the spatial variation of temperature $\Delta\theta_{p-m}$, and by extension, the steady-state performance.

7.2 Experimental Demonstration and Comparison with The Model

7.2.1 Experimental Facility and Procedure

A transient heat spreading experiment is conducted with a thin, commercial vapor chamber. The transient temperature field is characterized in response to a step heat input to demonstrate and confirm the key mechanisms identified in Section 7.1.2. A photograph of the 150 mm-long, 8.5 mm-wide, and 1.8 mm-thick vapor chamber (Novark Technologies) is shown in Figure 7.4a.

Figure 7.4c illustrates the experimental test setup, which is designed to isolate the vapor chamber from any object having a significant thermal capacity that would affect the transient heat transport behavior. This approach enables a direct comparison against the model without the confounding effects of external thermal masses.

The vapor chamber is suspended from posts using thin (0.2 mm diameter) steel wires looped around each end. The posts are spaced 130 mm apart in the direction along the heat spreader length and 95 mm apart in the transverse direction. The vapor chamber is suspended 130 mm above an optical breadboard. A central 8.5 mm length of the vapor chamber is wrapped tightly with a sheathed nichrome wire (90% Ni, 10% Cr; 5 ohm); thermal grease (Tgrease880, Laird Technologies) is applied between the heat spreader surface and the heater wire. A 30 V, 3 A power supply (GPS-2303, Gw Instek) is attached to the nichrome heater using lead wires. The vapor chamber rejects heat to the ambient via natural convection. The setup is isolated from ambient air currents using a 300 mm-long, 200 mm-wide, and 320 mm-tall rectangular enclosure which is open at the top.

Temperatures on the surface of the vapor chamber are measured using T-type thermocouples. The locations of these temperature measurements are shown in Figure 7.4b. Location *A* is in the center of the heated region, locations *B1* and *B2* are 15 mm from the ends of the heated region, and *C1* and *C2* are 40 mm from the ends of the heated region. The temperature at the heater (location *A*) is measured by inserting the thermocouple bead between the wrapped nichrome wire and the heat spreader. All other temperatures are measured by pressing the thermocouple beads into contact with the surface using a small piece of copper foil adhesive tape, taking care to avoid any stress on the wire. The thermocouples are wired to a reference junction maintained at 0 °C (CL122, Omega). The ambient temperature and the reference temperature are measured using RTDs. The current through the nichrome heater is measured using a shunt resistance (0.01 ohm) placed in series; the potential difference across the heater is measured directly. Data are collected

and recorded via National Instruments (NI) LabVIEW software at a rate of 3 Hz using a data acquisition chassis (NI cDAQ-9178) outfitted with modules for thermocouple (NI 9214), voltage (NI 9219), and RTD (NI 9217) measurement inputs.

The thermocouples are all simultaneously calibrated over a temperature range of 30 °C to 100 °C in steps of 10 °C using a dry block calibrator (Jupiter 4852, Isotech). The calibration temperature is measured using an RTD. A linear offset from the NIST ITS-90 standard is fitted to the calibration data for each thermocouple. The thermocouple temperature measurements have an uncertainty of $\pm 0.3\text{K}$ after this calibration procedure (Section 3.1.1).

Initially, the vapor chamber temperature (at all 5 thermocouple locations) is at the ambient value. At $t = 0$, a heat input of 3 W is imposed by turning on the power supply through the control panel. The temperature measurements are recorded till the temperature at location *A* reaches a steady state.

7.2.2 Replication of the Experimental Conditions in The Model

A comparison between the experiment and the time-stepping analytical model is established by simulating a vapor chamber of the same length and width as the sample tested in the experiments (150 mm length and 8.5 mm width). The vapor chamber wall has a thickness of 200 μm to match that of the sample tested. The layout of the wick in the vapor chamber tested does not match with that in the model, *i.e.* the wick in the vapor chamber tested does not line the inner surface of the wall. Also, the fluid charge volume in the vapor chamber is unknown. Hence, the thicknesses of the wicks and the vapor core are estimated inputs to the model to create an equivalent case as the tested sample. The wick, which lines the inner surface of the top and bottom walls of the simulated case, has thickness set to 250 μm each, such that the volume of the wick matches that in the physical sample. The wick primarily contributes to the total thermal capacity of the vapor chamber, which drives this method for setting the wick thicknesses. The vapor core thickness is set to 150 μm to match the experimental and simulated maximum transient value of the difference between the temperatures at locations *B* and *C*. This assumption is justified because the vapor core thickness primarily governs the in-plane temperature variations in the vapor chamber. The wall material is copper. A sintered copper wick is used with an assumed value of 0.6 for the porosity. Water is used as the working fluid as in the vapor chamber sample. Step heat inputs of 1.5 W each are applied at the center of the top and bottom faces of the heat spreaders,

totaling to a 3 W input, over a square heated region of 8.5 mm \times 8.5 mm. The remaining areas of the two faces reject heat to the ambient using a natural convection condition. The convection coefficient is computed based on the local wall temperature using empirical correlations [55]. The empirical correlations are defined for heated plates exposed only on one side. Hence the computed convection coefficient is multiplied by a constant factor to account for the different boundary conditions in the experiment. The factor is calibrated such that the average surface temperature (T_{avg}), at steady state, matches between the experiment and the simulation. The average surface temperature (T_{avg}) is computed by fitting lines between neighboring thermocouple location temperature measurements ($C1-B1$, $B1-A$, $A-B2$, $B2-C2$) and taking a constant value from the C locations to the length-wise ends of the heat spreader, equal to the corresponding C location temperature measurement. The ambient temperature is an input to the model from the experiments, and the heat spreader is initialized at a uniform temperature equal to the ambient temperature.

7.2.3 Comparison of Experiments and Simulations

The step input power supply in the experiment is turned on at $t = 0$ s; the power increases from 0 to 3.0 W in 1.33 s. The transient temperatures θ , measured at the thermocouple locations, are plotted in Figure 7.5 for the vapor chamber. The ambient temperature is 24.3 °C. The temperatures gradually increase from the ambient temperature to steady-state values.

Figure 7.6 and Figure 7.7 compare the results from the experiment with results from the simulation. The data presented in these figures follow the layouts of Figure 7.2 and Figure 7.3, respectively, and are used to confirm the governing mechanisms identified in Section 7.1.2.

Figure 7.6a plots the transient variation of the temperature at location A relative to the ambient (θ_A), indicative of the evaporator temperature. There is a good match between the experiment and simulation for this common metric of vapor chamber performance. Figure 7.6b plots the transient variation of the average surface temperature of the vapor chamber (defined in Section 7.2.2) relative to the ambient temperature ($\theta_{avg} = T_{avg} - T_{\infty}$). The match between the experiment and simulation indicates that the simulation accurately models the *total thermal capacity* of the vapor chamber, which governs the transient variation of θ_{avg} as discussed in Section 7.1.2. Figure 7.6c plots the transient variation of the length-wise temperature variation in the vapor chamber. The length-wise temperature variation is represented by the average difference between the temperatures at locations B and C ($\Delta\theta_{B-C} = [\theta_{B1} - \theta_{C1} + \theta_{B2} - \theta_{C2}]/2$). As was identified for the

transient spatial temperature variation in Figure 7.2c, the value of $\Delta\theta_{B-C}$ in Figure 7.6c increases sharply, and then gradually reduces towards a steady state, for both the experiment and the simulation. The time required for the value of $\Delta\theta_{B-C}$ to peak, governed by the *effective in-plane diffusivity* of the vapor chamber, is on the same order between the experiment and the simulation. Also, the transient profile of θ_{B-C} after the peak, governed by the *effective in-plane conductance* of the vapor core, matches well between the experiment and the simulation, all the way till a steady state is attained. Note that the peak value of this transient profile is used to calibrate the vapor-core thickness in the simulation, as discussed in Section 7.2.2.

Figure 7.7a and b show, for the experiment and the simulation respectively, the temperature difference from the surface average ($\theta - \theta_{avg}$) at the 5 thermocouple locations at different times. Similar to the trends in the transient temperature profile observed in Figure 7.3b, the temperature first increases in the near-heater region, followed by the outer region, for an initial period of time ($t = 1-4$ s in Figure 7.7). At later times ($t = 4-30$ s in Figure 7.7), the profile of $\theta - \theta_{avg}$ gradually flattens with time. A video showing the transient variation of $\theta - \theta_{avg}$ at the 5 thermocouple locations in the experiment, plotted along with the simulated profile of $\theta - \theta_m$ along the length of the vapor chamber, is included in the supplementary material of the publication [54]. The match of these trends between the experiment and simulation further verifies that the *effective in-plane diffusivity* and *effective in-plane conductance* govern the development of the spatial temperature profile.

7.3 Transient Vapor Chamber Performance Relative to a Copper Spreader

7.3.1 Dependence of Relative Transient Performance on Time Scale

In this section, the performance of a vapor chamber is benchmarked against a copper spreader of the same external geometry. The performance is strongly dependent on time scale, with multiple crossovers in the peak temperature between the two spreaders for the chosen case. The reasons for this complex comparative behavior are discussed based on the relative magnitudes of the governing mechanisms underlying the transient thermal behavior. This discussion serves as a basis for description to follow of the effects of parameters on the relative performance between the two spreaders (to be discussed in Section 7.3.2).

The case details for these simulations are the same as considered in Section 7.1.1, and have a zero wall thickness, with the only difference being that the vapor core thickness is increased from 40 μm to 200 μm . Time step sizes of 0.02 s and 0.1 s are used respectively for $t < 2$ s and $t > 2$ s.

Figure 7.8a shows the peak temperature θ_p as a function of time for the vapor chamber and the copper spreader. The plot indicates multiple crossovers between the temperatures. Figure 7.8b shows the corresponding mean temperature θ_m , and Figure 7.8c the peak-to-mean temperature difference $\Delta\theta_{p-m}$. In Figure 7.8b the mean temperature θ_m is seen to increase faster for the vapor chamber than the copper spreader, owing to its lower total thermal capacity. Figure 7.8c indicates that for time $t > 0.16$ s, $\Delta\theta_{p-m}$ is much lower for the vapor chamber than the copper spreader, reflecting a higher effective in-plane conductance for the vapor chamber. The higher effective in-plane conductance and lower total thermal capacity implies that the vapor chamber has a higher effective in-plane diffusivity. As a result, $\Delta\theta_{p-m}$ increases faster in the vapor chamber in its initial diffusion period ($t < 0.1$ s), as seen in Figure 7.8c. The lower effective in-plane conductance of the copper spreader, on the other hand, results in $\Delta\theta_{p-m}$ increasing to a higher value after its initial diffusion period. This causes a crossover in $\Delta\theta_{p-m}$ at $t = 0.2$ s, and a corresponding crossover in the θ_p profile as well. Because the vapor chamber θ_m increases faster than that of the copper spreader, another crossover in θ_p occurs at 4.9 s. At steady state (not seen in Figure 7.8), the value of θ_m eventually becomes almost the same for both spreaders and hence the value of θ_p is governed only by $\Delta\theta_{p-m}$. Given the higher value of $\Delta\theta_{p-m}$ at steady state for the copper spreader, its θ_p value also is higher than the vapor chamber. This behavior leads to the third crossover at $t = 29.4$ s.

The existence of these crossovers between the copper spreader and vapor chamber peak evaporator temperature θ_p indicates that the choice of heat spreaders is highly dependent on the time scale of interest. The existence of the multiple crossovers, versus the single crossover in Figure 7.2, merits the parametric study that follows.

7.3.2 Effects of Key Parameters on the Transient Performance

This section investigates the dependence of vapor chamber performance, relative to a copper spreader of equal external dimensions, on the vapor core thickness and input power. The governing mechanisms are sensitive to these two key parameters.

Generally, the total thermal capacity of the vapor chamber is lower than the copper spreader, due to the very low thermal capacity of the vapor core; this contrast increases with increasing vapor

core thickness. The effective in-plane conductance of the vapor core increases polynomially with thickness, as has been identified in Chapter 5 versus a linear increase with thickness for the copper spreader. These trends imply that the effective in-plane diffusivity of the vapor chamber (which can be understood as the ratio of the effective in-plane conductivity of the vapor core and the volumetric capacity of the wick as identified in Section 7.1.2) relative to the copper spreader also increases with vapor-core thickness. The vapor core effective in-plane conductance also increases with increasing mean temperature due to the temperature-dependence of the vapor properties; hence, as the mean temperature increases with time, so does the effective in-plane conductance. Note that the mean temperature of the vapor chamber in the transient regime is always higher due to its lower total thermal capacity compared to the copper spreader.

Figure 7.9a (with details at short time-scales shown in Figure 7.9b) maps the relative transient performance for a range of vapor-core thicknesses as a function of time. The case details for these simulations are the same as described in Section 7.1.1, except for the vapor core thickness. The evaporator is subjected to a heat input of 4 W. A time step of 0.1 s is used for the time marching.

The relative performance is presented using a metric defined as

$$M_{VC-Cu} = \ln \left(\frac{\theta_{p,Cu}}{\theta_{p,VC}} \right) \quad (7.1)$$

where $\theta_{p,VC}$ and $\theta_{p,Cu}$ correspond to the peak evaporator temperatures of the vapor chamber and the copper spreader, respectively. A value of zero for M_{VC-Cu} corresponds to equal performance for both heat spreaders; this performance threshold is shown in white on the contour scale in Figure 7.9a and Figure 7.9b. A positive value, shown in blue, indicates the vapor chamber performs better while a negative value, shown in red, indicates the copper spreader performs better.

Regions on the contour maps in Figure 7.9a and Figure 7.9b are identified by numbers 1 to 6 and the governing mechanisms responsible for relative performance in these regions are explained here. In region 1 the vapor-core thickness is small enough that its effective in-plane conductance at all times through steady-state is less than that of the copper spreader, causing a high $\Delta\theta_{p-m}$. Given that the vapor chamber also always has a higher θ_m than the copper spreader, the vapor chamber performs worse in this region. This trend was previously identified in the steady-state analysis conducted by Yadavalli *et al.* [56]. Region 2 also exists due to this lower effective in-plane conductance. However, it extends to higher thicknesses, because at shorter times, low temperatures

lead to lower values of effective in-plane conductance for the vapor chamber. Region 3 corresponds to the initial diffusion period; the vapor chamber performs worse because the higher effective in-plane diffusivity of the vapor chamber leads to a faster effective in-plane diffusion process and hence a faster initial increase in temperature. The vapor chamber performs better than the copper spreader in region 4 due to its high effective in-plane conductance due to the vapor core. At these early times, the mean temperatures of the vapor chamber and copper spreader have not yet risen much above ambient, and the differences in performance are instead attributed to the peak-to-mean temperature difference $\Delta\theta_{p-m}$, which is governed by the vapor core effective in-plane conductance. In region 5, the vapor chamber mean temperature θ_m increases faster than that of the copper spreader due to its relatively low total thermal capacity, causing worse relative performance. With increasing vapor core thickness, the total thermal capacity of the copper spreader increases, which heats up slower, and the right-side border of region 5 extends to a higher time. At the later times in region 6 (extending to steady state), the values of θ_m are similar for both spreaders. However, the vapor chamber has a higher effective in-plane conductance than the copper spreader, leading to a lower $\Delta\theta_{p-m}$ and hence better performance.

Contour maps of the performance of the vapor chamber relative to the copper spreader are plotted in Appendix C for two more conditions; the first accounts for the effects of including the vapor chamber walls, and the second accounts for a high heat input of 100 W. Adding a wall primarily dampens the contrast between the performance of the vapor chamber and the copper spreader. In the second case, region 4 disappears.

In Figure 7.9c and Figure 7.9d, the effects of input power on the relative transient performance are explored for a range of vapor core thicknesses; the contour shading is omitted from the maps and instead the threshold lines ($M_{VC-Cu} = 0$) are drawn as solid lines for each power level. Increasing the input power increases the entire temporal profile of the mean temperature θ_m , and hence the vapor core effective in-plane conductance. This is the primary cause behind the changes in the relative performance thresholds with increasing power, which generally expand the size of the operating regions in which the vapor chamber performance is better than copper.

Identification of these mechanistic performance thresholds is critical for understanding the use conditions under which vapor chambers are favorable relative to copper spreaders. For steady-state design, there is a single threshold value at some vapor-core thickness at which this distinction is possible, as had been previously identified from steady-state analysis [56]. In the transient

regime, however, it is revealed that the time scale of operation is critical in determining the non-trivial and unintuitive trends in relative performance. For example, for the case investigated in Figure 7.9a and Figure 7.9b, for vapor core thicknesses in the range of 50-100 μm , the use of a vapor chamber is favorable only for time-scales that are much longer than 5 s. For vapor-core thicknesses in the range of 200-300 μm use of vapor chambers is favorable for time scales less than 2-4 s or greater than 30-50 s, but not in between. These results demonstrate that the existing design norms regarding the relative advantage of vapor chambers over metal spreaders, developed on the premise of steady operation and associated analyses, are insufficient. A more complex set of design criteria emerges from these transient thresholds that must be considered in the implementation of vapor chamber heat spreaders for thermal management in applications having transient power variations.

7.4 Conclusions

The mechanisms governing the transient thermal response of a vapor chamber are identified using a low-cost, 3D, and transient vapor chamber transport model. Conclusions from this analysis are corroborated with experiments conducted using a commercial vapor chamber. The vapor chamber transport model is used to compare the transient thermal response of a vapor chamber with that of a solid copper spreader. The performance of both heat spreader types is analyzed based on the peak evaporator temperature. The decomposition of this temperature into its key components, namely the volume-averaged mean temperature and the peak-to-mean temperature difference, leads to the identification of three key mechanisms that govern the transient thermal response of vapor chambers: (1) the total thermal capacity of the vapor chamber governs the rate of increase of the volume-averaged mean temperature θ_m , (2) the effective in-plane diffusivity governs the time required for the initial development of the spatial temperature profile $\theta - \theta_m$, and (3) the effective in-plane conductance of the vapor core governs the magnitude of the spatial variation of temperature $\Delta\theta_{p-m}$, and by extension, its steady-state performance.

The vapor chamber transport model is also used to benchmark the transient performance of a vapor chamber against a solid copper spreader for a range of vapor-core thicknesses and input powers. The relative performance of a vapor chamber strongly depends on the operating parameters and the time scale of operation. Relative performance is mapped over the parameter-time space and regions are identified in which the vapor chamber performs better (or worse) than

the copper spreader; reasons for the existence of these regions are explained based on the governing mechanisms.

This work serves as a foundation in understanding the benefits and limitations of using vapor chambers for thermal management under transient conditions and for designing vapor chambers for improved transient performance.

Nomenclature

$A, B1, B2,$ $C1, C2$	temperature measurement locations
C_p	specific heat capacity [$\text{J kg}^{-1} \text{K}^{-1}$]
h	convection coefficient [$\text{W m}^{-2} \text{K}^{-1}$]
h_{fg}	specific enthalpy of vaporization [J kg^{-1}]
K	permeability [m^2]
k	thermal conductivity [$\text{W m}^{-1} \text{K}^{-1}$]
M_{VC-Cu}	transient performance of a vapor chamber relative to a copper spreader
\dot{m}''	mass flux rate [$\text{kg m}^{-2} \text{s}^{-1}$]
P	pressure [Pa]
Q	input power [W]
R	specific gas constant [$\text{J kg}^{-1} \text{K}^{-1}$]
T	temperature [K]
T_{sat}	saturation temperature [K]
T_∞	ambient temperature [K]
t	time [s]
u	x -component of velocity [m s^{-1}]
\vec{V}	velocity vector [m s^{-1}]
v	y -component of velocity [m s^{-1}]
w	z -component of velocity [m s^{-1}]
x	x -coordinate (length) direction [m]
y	y -coordinate (width) direction [m]
z	z -coordinate (thickness) direction [m]

Greek

δ_{vap}	vapor-core thickness [m]
θ	temperature relative to the ambient ($T-T_\infty$) [K]
μ	viscosity [Pa s]
ρ	density [kg m^{-3}]
σ	accommodation coefficient [-]
ϕ	porosity [-]

Subscript

<i>A</i>	thermocouple location <i>A</i>
<i>B-C</i>	difference in values between thermocouple locations <i>B</i> and <i>C</i>
<i>Cu</i>	copper spreader
<i>avg</i>	average surface based on the 5 thermocouple location measurements
<i>eff</i>	effective wick property
<i>int</i>	wick–vapor interface
<i>l</i>	liquid phase
<i>m</i>	volume-averaged
<i>p</i>	evaporator maximum
<i>p-m</i>	difference in value between evaporator maximum and volume-averaged
<i>VC</i>	vapor chamber
<i>vap</i>	vapor core

Table 7.1. Copper and wick properties.

Property	Value
Wick effective thermal conductivity (k_{eff})	40 W/mK
Copper volumetric thermal capacity (ρC_p) _s	3.42×10 ⁶ J/m ³ K
Wick porosity (ϕ)	0.6
Copper thermal conductivity (k)	387.6 W/mK

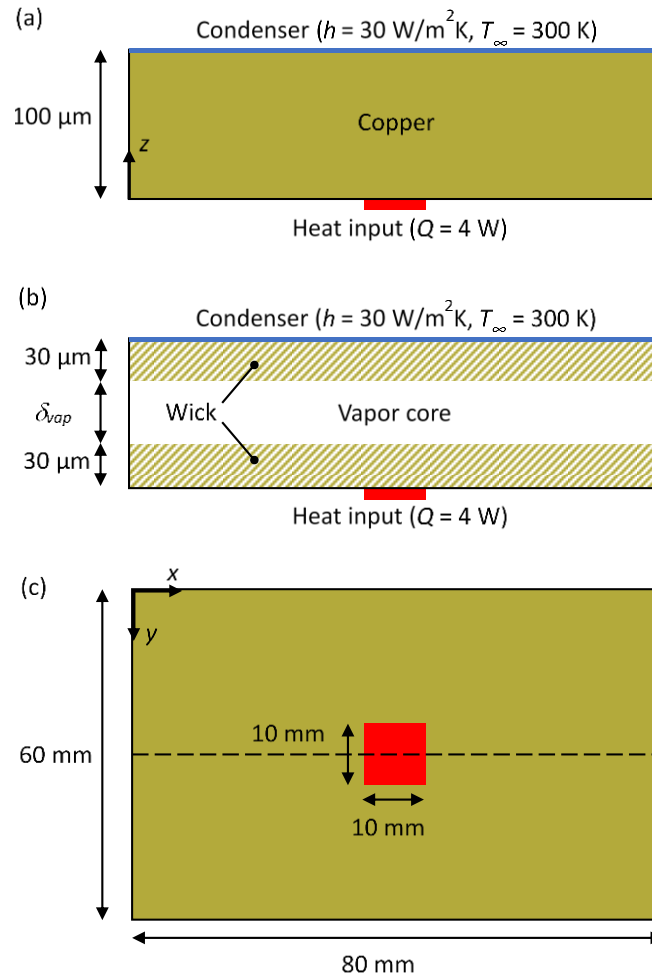


Figure 7.1. Geometry (not to scale) and boundary conditions for the transient heat spreading simulations showing (a) a section view for the copper spreader case, (b) a section view for the vapor chamber case, and (c) a bottom view of the evaporator-side that is common to both cases.

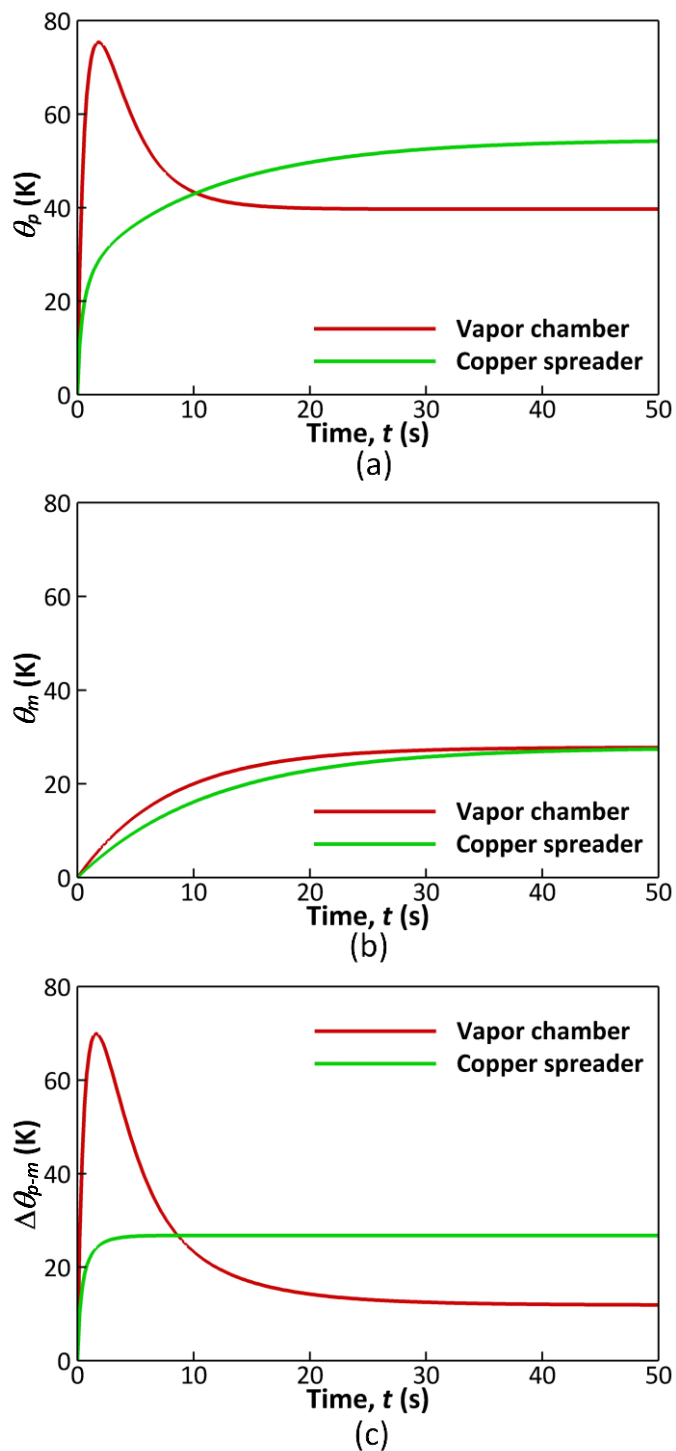
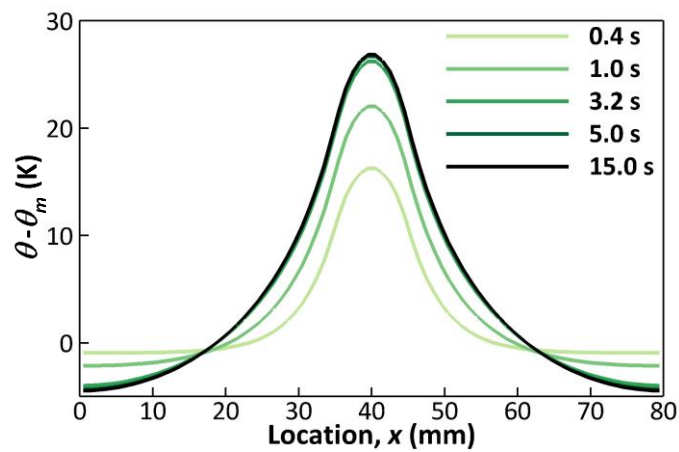
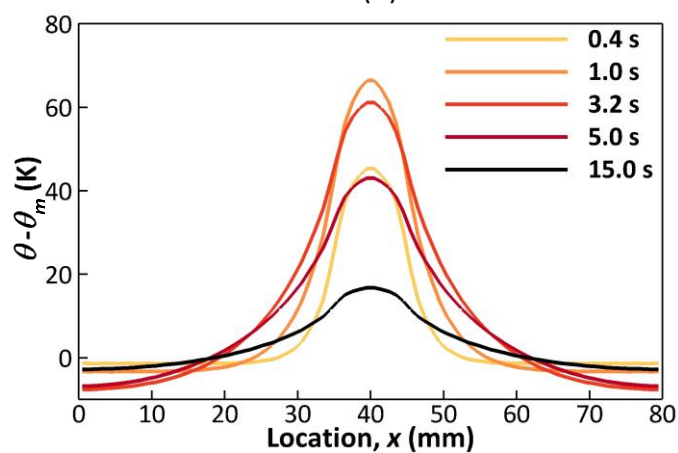


Figure 7.2. Comparison between the vapor chamber and the copper spreader simulation results ($\delta_{vap} = 40 \mu\text{m}$) showing the temporal variation of the (a) peak temperature θ_p , (b) volume-averaged mean temperature θ_m , and (c) difference between the peak and mean temperatures $\Delta\theta_{p-m} = \theta_p - \theta_m$.



(a)



(b)

Figure 7.3. The profile of local temperature difference from the mean ($\theta - \theta_m$) along a line on the evaporator-side surface of the heat spreader (dashed line in Figure 7.1c) at different times, for (a) the copper spreader and (b) the vapor chamber. Note the different scales of the vertical axis for (a) and (b).

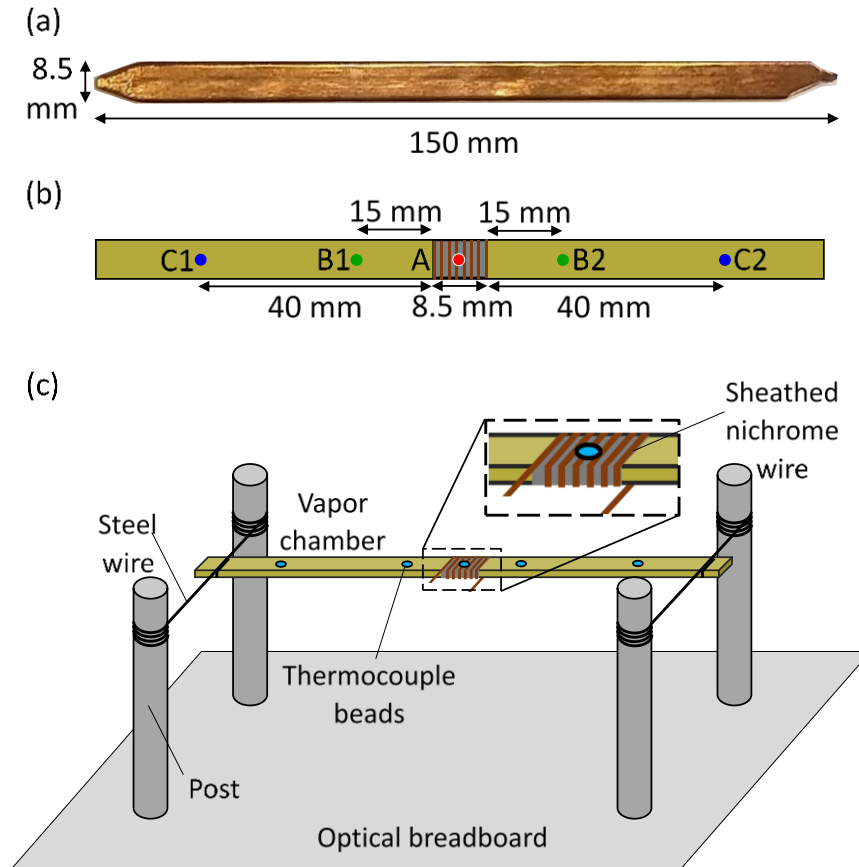


Figure 7.4. (a) Photograph of the vapor chamber sample in top view, (b) diagram of the locations of the thermocouple beads and heated length, and (c) illustration of the experimental test setup.

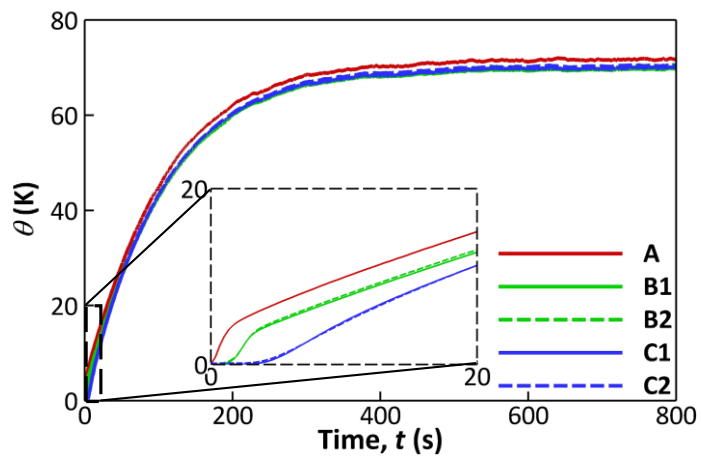


Figure 7.5. Experimental measurements of the temperature θ at the five thermocouple locations as a function of time.

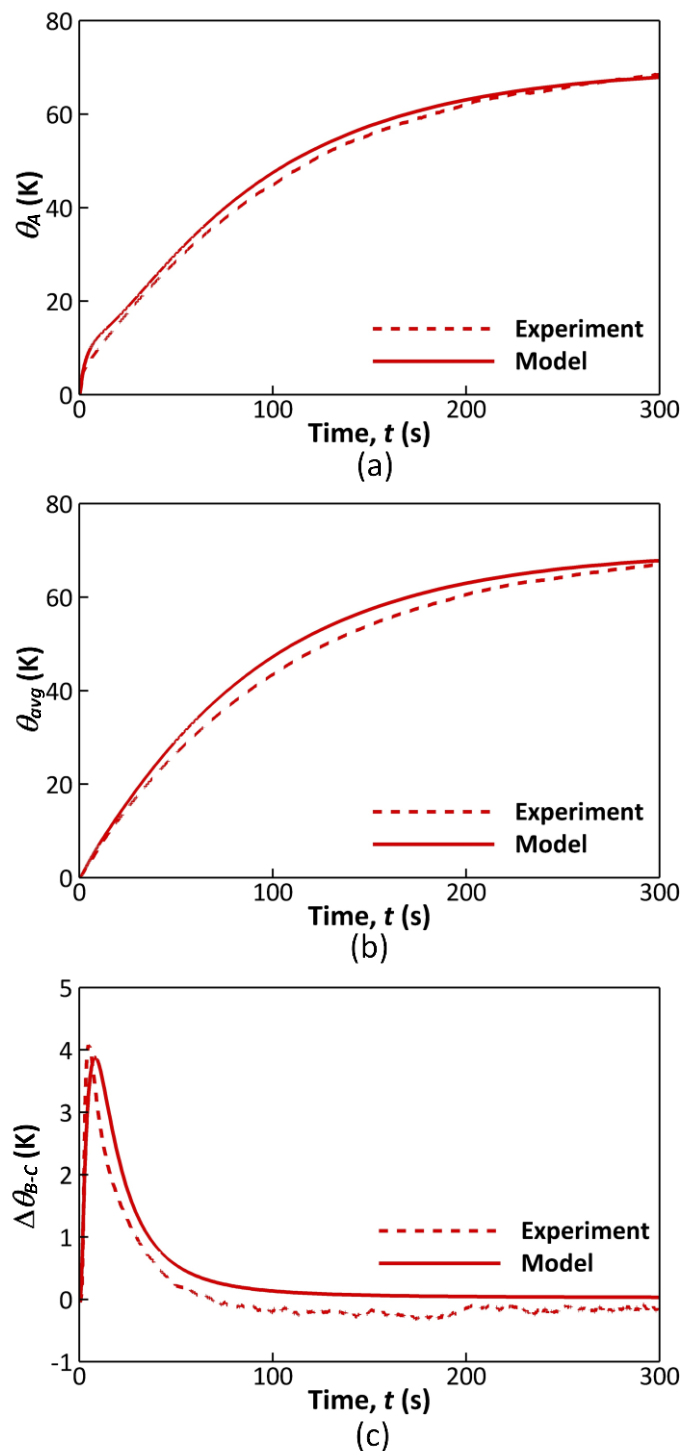


Figure 7.6. Comparison of the experiment and simulation: (a) temperature at thermocouple location A (θ_A), (b) average surface temperature relative to the ambient temperature (θ_{avg}), and (c) the average difference between the temperatures at B and C ($\Delta\theta_{B-C}$).

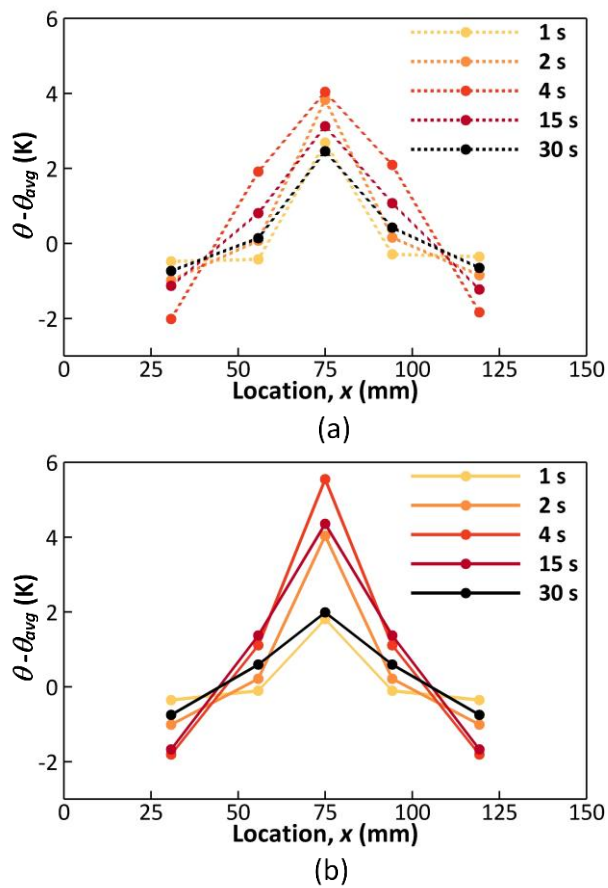


Figure 7.7. Vapor chamber local surface temperatures difference from the average surface temperature ($\theta - \theta_{avg}$) at the thermocouple locations at different times from (a) the experiment and (b) the simulation.

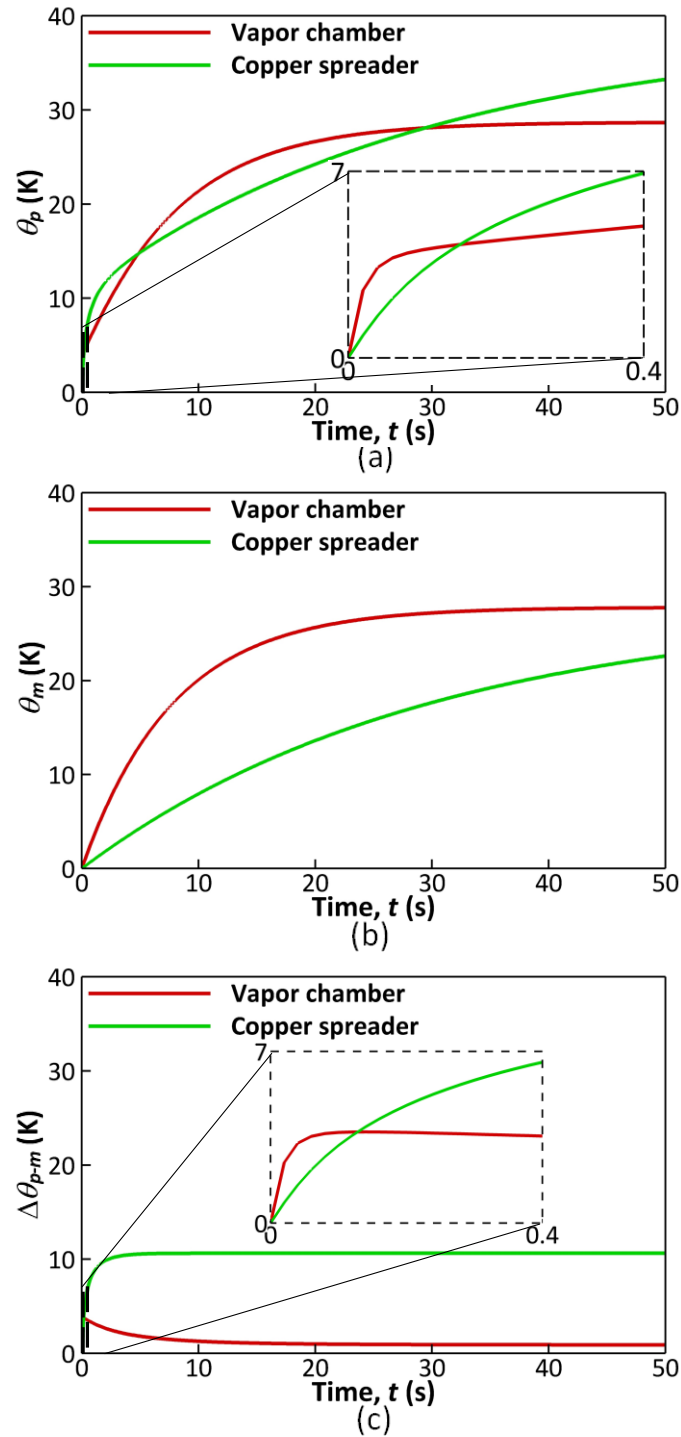


Figure 7.8. Comparison between the vapor chamber and the copper spreader simulation results ($\delta_{vap} = 200 \mu\text{m}$) showing the temporal evolution of (a) peak temperature θ_p , (b) volume-averaged mean temperature θ_m , and (c) difference between the peak and mean temperatures $\Delta\theta_{p-m} = \theta_p - \theta_m$.

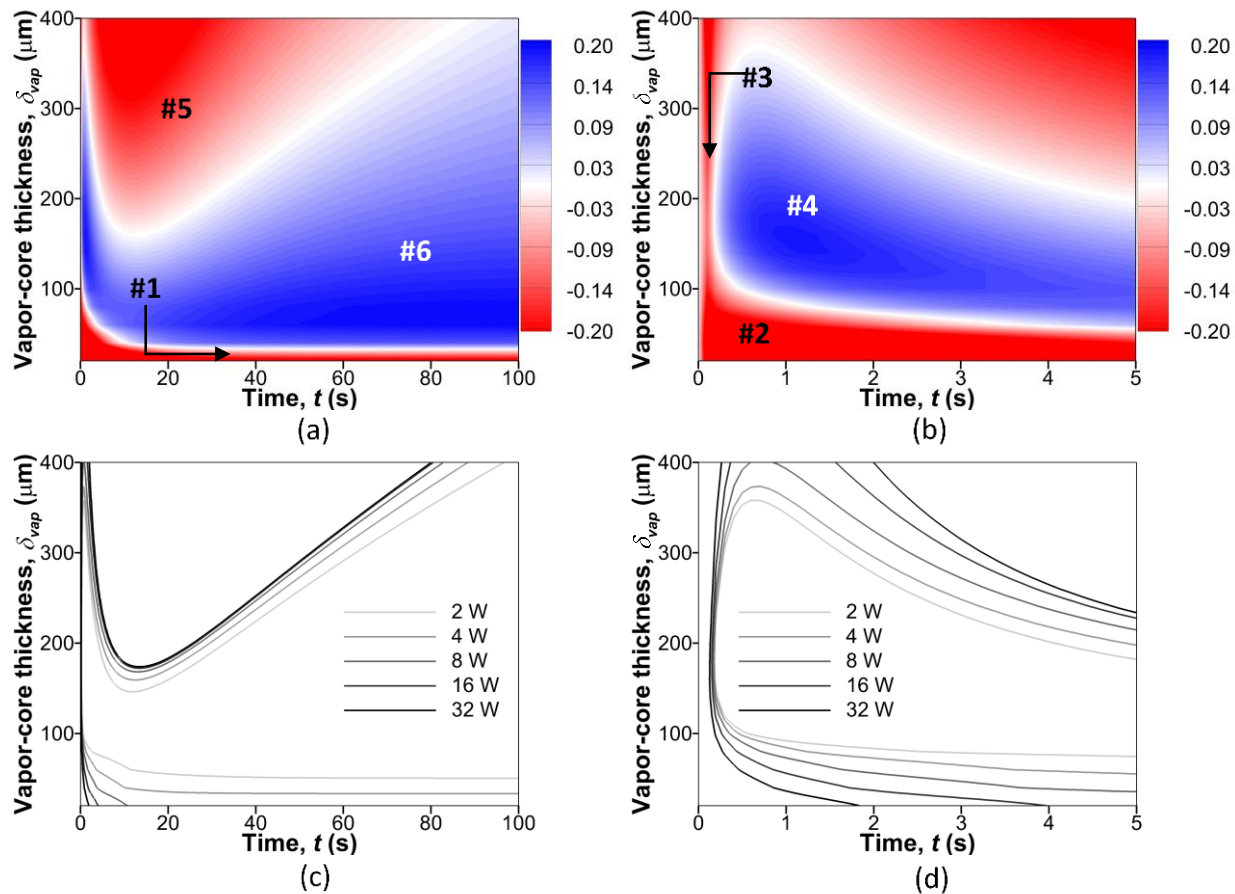


Figure 7.9. Contour plot of the metric for the thermal performance of a vapor chamber relative to a copper spreader (M_{VC-Cu}), for a range of vapor core thicknesses, and as a function of time for (a) $t < 100$ s and (b) a zoomed-in view for $t < 5$ s. Threshold lines ($M_{VC-Cu} = 0$) for the thermal performance of a vapor chamber relative to that of a copper spreader as a function of time for a range of vapor core thicknesses at different input powers in the range (c) $t < 100$ s and (d) a zoomed-in view for $t < 5$ s.

8. ON THE TRANSIENT THERMAL RESPONSE OF THIN VAPOR CHAMBER HEAT SPREADERS: OPTIMIZED DESIGN AND FLUID SELECTION

In this chapter, the knowledge of the key mechanism governing the transient thermal behavior of vapor chambers is utilized to develop notional practices for the design of vapor chambers under transient heat loading. Two key aspect of the vapor chamber design are considered: (1) optimization of the thicknesses of the vapor chamber wall, wick, and vapor core, with a given total available thickness; and (2) selection of the working fluid. Simulations performed with the time-stepping analytical model are used to identify and demonstrate a procedure for designing the vapor chamber. The material in this chapter has been submitted to a journal and is in review [57].

8.1 Simulation Case Details

The details of the vapor chamber simulations used for the demonstration of the procedure for the design of vapor chambers is described here. The geometry and boundary conditions for the simulations are shown in Figure 8.1. The rectangular vapor chamber has a length of 80 mm, a width of 60 mm, and a thickness of 300 μm . The vapor chamber wall is copper, the wick is sintered copper. The temperature-dependent properties of the working fluid are obtained from the commercial fluid database software REFPROP [48]. The relevant properties of the wick and copper are in Table 7.1.

The vapor chamber is subjected to a heat input of 4 W starting at time $t = 0$ over an area of 10 mm \times 10 mm at the center of the evaporator-side face. The rest of the evaporator-side face is insulated. The opposite face has a convective boundary condition, with heat transfer coefficient $h = 30 \text{ W/m}^2\text{K}$ and ambient temperature $T_\infty = 300 \text{ K}$. At time $t = 0$, the vapor chamber is initially at a temperature of 300 K. For the time marching in the model evaluation, two time-step sizes are used, 0.05 s for $t < 10 \text{ s}$ and 1 s for $t > 10 \text{ s}$.

8.2 Optimization of the Wall and Vapor-Core Thicknesses

As discussed in Chapter 7, the total thermal capacity of the vapor chamber is effectively the sum of the thermal capacities of the wall and the wick, and hence will increase with the increase

in wall or wick thickness, while the effective in-plane vapor-core conductance increases with an increase in the vapor-core thickness. The wick has a minimum thickness requirement to satisfy the capillary limit; any smaller, and the increase in the flow velocity will increase the pressure drop in the wick above the capillary pressure. Given a fixed thickness, and setting the wick to a minimum thickness, an increase in the thickness of vapor-core thickness will increase the effective in-plane conductance of the vapor core, but reduce the wall thickness, and hence the total thermal capacity. Hence an optimization of the vapor-core and wall thicknesses is needed; for a fixed external geometry and set of boundary conditions, vapor chambers with a range of wall and vapor-core thickness are simulated to identify the optimum allotment of these two thicknesses. The factors governing these optimum values are compared under transient versus steady-state conditions.

Water is selected as the working fluid for the simulations. The value for the accommodation coefficient σ (equation 4) is set to 0.03 [44]. The thicknesses of the wick layers on either side are set to 10 μm each. The thickness of the wall on either side is varied from 0 μm to 140 μm ; hence, within the total available thickness, the vapor-core thickness correspondingly varies from 280 μm to 0 μm . Note that a minimum wall thickness is needed to support the pressure difference between the internal vapor and external atmosphere; evaluation of this mechanical limit is out of the scope of this study.

Figure 8.2a shows the temporal profile of the temperature at the center of the heat input relative to the ambient temperature, θ_p , for three values of vapor-core thickness. The value of θ_p for each of the three cases increases from 0, at $t = 0$, toward a steady-state value. At steady state ($t = 200$ s), the peak temperature θ_p is highest for the lowest value of vapor-core thickness, and the value monotonically decreases when the vapor-core thickness is increased from 20 μm to 100 μm to 260 μm . The temperature at the evaporator is closest to the temperature of the electronic component, and hence is used for characterizing the vapor chamber performance. Under transient conditions, given that this temperature is time varying, multiple methods can be used to characterize the performance, such as time till θ_p reaches a set maximum limit, or the value of θ_p at a particular time, or an average value of θ_p over a range of time. In this study, the transient performance of the vapor chamber is characterized by the peak temperature θ_p at time $t = 50$ s (marked by the vertical dashed line in Figure 8.2a). At time $t = 50$ s, the value of θ_p reduces from 31 K to 26.1 K when the vapor-core thickness is increased from 20 μm to 100 μm but then increases to 28.6 K when the vapor-core thickness is further increased to 260 μm . Thus, it is observed that the relation between

the vapor-core thickness (and by extension the wall thickness) and the transient performance is nonmonotonic, unlike the monotonic relationship for steady state performance.

To understand this relation between the transient performance and the vapor-core thickness, the peak temperature θ_p is decomposed into two components, the mean (volume-averaged) temperature θ_m , shown in Figure 8.2b, and the difference between the peak and mean temperatures, $\Delta\theta_{p-m} = \theta_p - \theta_m$ (*i.e.*, the peak-to-mean difference), shown in Figure 8.2c. As identified in Chapter 7, three mechanisms govern the transient thermal behavior of vapor chambers: 1) the *total thermal capacity* of the vapor chamber governs the rate of increase of the volume-averaged mean temperature, θ_m ; 2) the *effective in-plane conductance* of the vapor core governs the magnitude of the peak-to-mean temperature difference $\Delta\theta_{p-m}$; 3) the *effective in-plane diffusivity* governs the time required for the initial rise in the peak-to-mean temperature difference $\Delta\theta_{p-m}$. The third mechanism is only relevant for a brief initial period ($t < 10$ s, as seen in Figure 8.2c), and thus, is not relevant for this specific investigation of performance at 50 s. Given the fixed wick thickness, with increasing vapor-core thickness, and hence reducing wall thickness, the total thermal capacity of the vapor chamber reduces. Thus, in Figure 8.2b, the vapor chamber heats up faster with increasing vapor-core thickness and the value of θ_m at time $t = 50$ s monotonically increases. As discussed in Chapter 7, the effective in-plane conductance of the vapor core increases polynomially with increasing vapor-core thickness. As seen in Figure 8.2c, the peak-to-mean temperature difference $\Delta\theta_{p-m}$ is smaller at all times when the vapor-core thickness is increased. Thus, the two mechanisms governing the transient vapor chamber performance (at $t = 50$ s) have opposite trends with vapor-core thickness, leading to the net nonmonotonic relation observed in Figure 8.2a. Note that at steady state, the total thermal capacity of the vapor chamber is irrelevant, and the performance is only governed by the effective in-plane conductance of the vapor core, which explains the monotonic improvement in the vapor chamber performance at steady state (at $t = 200$ s) with increasing vapor-core thickness.

Figure 8.3a and Figure 8.3b respectively show the vapor chamber transient (at $t = 50$ s) and steady-state (at $t = 200$ s) evaporator temperature θ_p as a function of the vapor-core thickness. At steady state (Figure 8.3b), the performance monotonically improves (*i.e.*, the temperature decreases) with increasing vapor core thickness. To design a vapor chamber for improved steady-state performance, the vapor-core thickness should generally be maximized, as proposed in Chapter 4. However, under transient conditions, due to the nonmonotonic relation of the

performance with the vapor-core thickness, an optimum value of the vapor-core thickness exists that minimizes θ_p , at 90 μm in this case. Thus, when designing a vapor chamber for improved transient performance, the optimal ratio between the vapor core thickness and wall thickness must be evaluated for the specific case and operating time of interest. The notional vapor chamber design practices that have been developed based on the steady-state performance metrics cannot be directly adopted for design under transient conditions.

8.3 Selection of Working Fluid

8.3.1 Selection Procedure

The performance of a vapor chamber is sensitive to the thermophysical properties of both the liquid and vapor phases of the working fluid. Therefore, selecting a working fluid is critical to the design of a vapor chamber. In Chapter 5, the relation between the properties of the working fluid and the steady-state performance of a vapor chamber was identified, and a procedure was developed that allowed selection of the working fluid that would provide the best steady-state performance among all available options. Two fluid property groups govern the performance of a vapor chamber at steady state, the liquid-phase figure of merit M_l and the vapor-phase figure of merit M_v , defined as

$$M_l = \frac{\gamma \rho_l h_{fg}}{\mu_l} \quad \text{and} \quad M_v = \frac{P_v \rho_v h_{fg}^2}{\mu_v R T_v^2}. \quad (8.1)$$

The liquid figure of merit M_l has been commonly used for the selection of working fluids that maximize the capillary limit in conventional vapor chambers having a relatively thick vapor core [6]. At the capillary limit, the pressure drop in the liquid matches the capillary pressure provided by the porous wick; any increase in the liquid pressure drop would result in dryout of the wick near the evaporator. The properties included in the liquid-phase figure of merit thereby govern the required wick thickness to avoid the capillary limit, at a given operating power. The vapor figure of merit, introduced by Yadavalli *et al.* [56], governs the effective in-plane conductance of the vapor core.

A procedure for the selection of the working fluids to minimize the evaporator peak temperature at steady state is defined in Chapter 5. As discussed in Section 8.2, the steady-state performance of a vapor chamber is maximized by maximizing the vapor-core thickness. Thus, for

a fixed total thickness of the vapor chamber, minimizing the wick and wall thicknesses will maximize the vapor-core thickness. The minimum required thickness of the wick to avoid the capillary limit is computed as a function of M_l ($\delta_{wick} \propto M_l^{-0.5}$). The maximized vapor-core thickness and M_v determine the effective in-plane conductance of the vapor core. The fluid that yields the highest effective in-plane conductance of the vapor core, is selected as the working fluid.

The performance of a vapor chamber under transient conditions is governed by both the total thermal capacity of the vapor chamber, including the thermal capacities of the wick and the wall, and the effective in-plane conductance of the vapor core. The thermal capacities of the wall and wick are governed by their thicknesses and material specific heat capacities; in the case of the wick, the heat capacity is directly related to the volumetric capacity of the liquid phase of the working fluid, C_{vol} . The effective in-plane conductance of the vapor core is governed by the vapor-core thickness and M_v . The following procedure is proposed for selection of the working fluid that maximizes performance under transient conditions (*i.e.*, minimizes the evaporator temperature at a given time) for a given case. For each candidate working fluid: 1) minimize the thickness of the wick to satisfy the capillary limit based on the M_l value for the fluid; 2) optimize the thicknesses of the wall and vapor core as was discussed in Section 8.2; this fluid-specific optimization is governed by tradeoff between the increasing the total thermal capacity of the wall and decreasing the effective in-plane conductivity of the vapor core. This process can be repeated for all fluids of interest to identify the one that yields the best performance. Note that both the wick and the wall provide thermal capacity for the vapor chamber. Despite this, it is always favorable to minimize the wick thickness. This is because both the wall and wick have similar values of volumetric capacity (3420.6 kJ/m³/K for copper and 4166.3 kJ/m³/K for liquid water), but copper walls will have a much higher conductivity than porous wicks. Thus, the walls can contribute nearly equally as the wick in terms of added capacity, but contribute more toward the effective in-plane conductance of the vapor chamber, justifying minimizing the thickness of the wick.

8.3.2 Demonstration of the Procedure

The procedure for the selection of working fluid is demonstrated in this section for the case described in Section 8.1. This demonstration is conducted to choose between two working fluids, water and methanol. The thermophysical properties of the fluids are obtained from the commercial fluid database software REFPROP [48] and the values of the relevant property groups are shown

in Table 8.2, computed at a temperature of 300 K. The value for the accommodation coefficient σ (equation 4) is set to 0.03 for water [44] and 0.056 for methanol [58].

The first step of the working fluid selection procedure is minimizing the wick thickness for the given operating power. The minimum wick thickness is found to be 10 μm for water and 23 μm for methanol, which follows the inverse proportionality with the square root of M_l , as noted in Section 8.3.1. The second step is to optimize between the wall and the vapor-core thicknesses. For water, the thickness of the wall is varied from 0 μm to 140 μm . The vapor-core thickness correspondingly varies from 280 μm to 0 μm . For methanol, the thickness of the wall is varied from 0 μm to 127 μm . The vapor-core thickness correspondingly varies from 254 μm to 0 μm .

Figure 8.4 shows the value for the evaporator temperature θ_p as a function of vapor-core thickness, for the two fluids. The plot shows that the optimum vapor-core thickness for the two fluids is different, 90 μm (95 μm wall thickness) for water compared to 52 μm (101 μm wall thickness) for methanol. More importantly, at these optimum dimensions, the value of θ_p methanol (24.1 K) is lower than for water (26.1 K). This can be attributed to the improved total thermal capacity and effective in-plane conductance for the optimal design with methanol as the working fluid. The wall and wick thickness are both larger for the case with methanol, leading to a higher total thermal capacity, despite the lower volumetric capacity of methanol compared to water. This is indicated by the lower value of θ_m (23.3 K) as compared to that for the case with water (24.1 K). The effective in-plane conductance is governed by the vapor-core thickness and M_v . For the case with methanol, despite a much smaller vapor-core thickness, the significantly higher value of M_v leads to a smaller value of $\Delta\theta_{p-m}$ (0.8 K) than that for the case of water (2.0 K).

Despite the complex and nonintuitive relations between the design parameters and the vapor chamber performance, a procedural approach is developed for the design of vapor chambers under transient conditions. Though the demonstration here is limited to specific cases, the procedure can generally be applied for a broad range of operating conditions, including different geometries, boundary conditions and transient metrics, due to the fact that the procedure is developed using the understanding of the mechanisms governing the transient thermal behavior of vapor chambers.

8.4 Conclusions

In this work, practices are developed for the design of vapor chambers to improve performance under transient conditions, which includes the optimization of the thicknesses of the wall, the wick and the vapor core, and the selection of a working fluid. Procedures are defined for the design of these two design parameters, followed by demonstration using numerical simulations of example cases. The procedures are informed by the key mechanisms governing the transient thermal behavior of vapor chambers. It was concluded that the notional practices for the optimization of the vapor chamber wall, wick and vapor core thicknesses, under steady-state conditions, cannot be directly used under transient conditions. Due to the existence of multiple governing mechanisms, and the possibility of them having a competing relation with the design parameter, the design of a vapor chambers under transient conditions must be evaluated for the specific case and operating time of interest. Due to the nonintuitive relations between the design parameters and the vapor chamber performance a procedural approach is developed for the design of vapor chambers that accounts for the multiple governing mechanisms.

Nomenclature

C_p	specific heat capacity [$\text{J kg}^{-1} \text{K}^{-1}$]
C_{vol}	volumetric heat capacity of the liquid phase [$\text{J m}^{-3} \text{K}^{-1}$]
h	convection coefficient [$\text{W m}^{-2} \text{K}^{-1}$]
h_{fg}	specific enthalpy of vaporization [J kg^{-1}]
K	permeability [m^2]
k	thermal conductivity [$\text{W m}^{-1} \text{K}^{-1}$]
M_l	liquid-phase fluid figure of merit
M_v	vapor-phase fluid figure of merit
\dot{m}''	mass flux rate [$\text{kg m}^{-2} \text{s}^{-1}$]
P	pressure [Pa]
Q	input power [W]
R	specific gas constant [$\text{J kg}^{-1} \text{K}^{-1}$]
T	temperature [K]
T_{sat}	saturation temperature [K]
T_∞	ambient temperature [K]
t	time [s]
u	x -component of velocity [m s^{-1}]
\vec{V}	velocity vector [m s^{-1}]
v	y -component of velocity [m s^{-1}]
w	z -component of velocity [m s^{-1}]
x	x -coordinate (length) direction [m]
y	y -coordinate (width) direction [m]
z	z -coordinate (thickness) direction [m]

Greek

δ_{vap}	vapor-core thickness [m]
δ_{wick}	wick thickness [m]
δ_{wall}	wall thickness [m]
θ	temperature relative to the ambient ($T - T_\infty$) [K]
μ	viscosity [Pa s]
ρ	density [kg m^{-3}]

σ	accommodation coefficient [-]
ϕ	porosity [-]

Subscript

<i>eff</i>	effective wick property
<i>int</i>	wick–vapor interface
<i>l</i>	liquid phase
<i>m</i>	volume-averaged
<i>p</i>	evaporator maximum
<i>p-m</i>	difference in value between evaporator maximum and volume-averaged
<i>v</i>	vapor phase

Table 8.1. Copper and wick properties.

Property	Value
Wick effective thermal conductivity (k_{eff})	40 W/mK
Copper volumetric thermal capacity (ρC_p) _s	3.42×10 ⁶ J/m ³ K
Wick porosity (ϕ)	0.6
Copper thermal conductivity (k)	387.6 W/mK

Table 8.2. Fluid property groups for water and methanol.

Property	Water	Methanol
$M_l (/10^{10}) \text{ (W/m}^2\text{)}$	20.4	3.8
$M_v (/10^{12}) \text{ (W/m}^3\text{K)}$	1.3	27.7
$C_{vol} (/10^6) \text{ (J/m}^3\text{K)}$	4.2	2.0

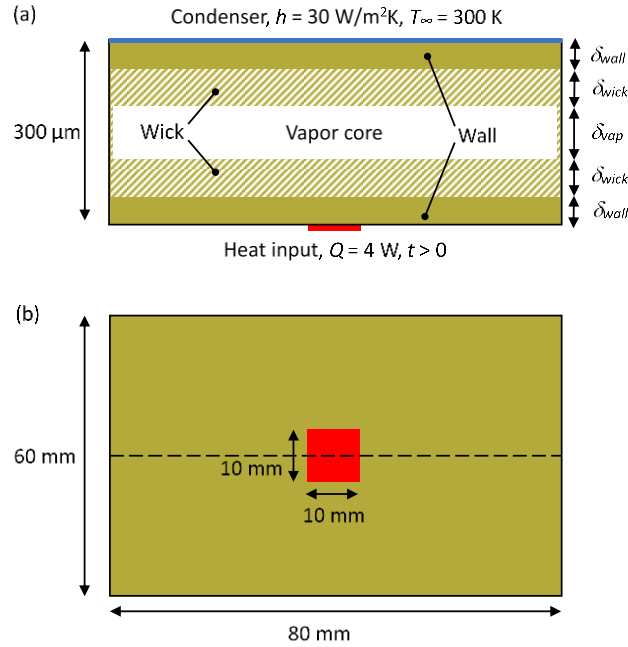


Figure 8.1. Geometry (not to scale) and boundary conditions for the transient vapor chamber simulations showing (a) a section view and (b) a bottom view of the evaporator side.

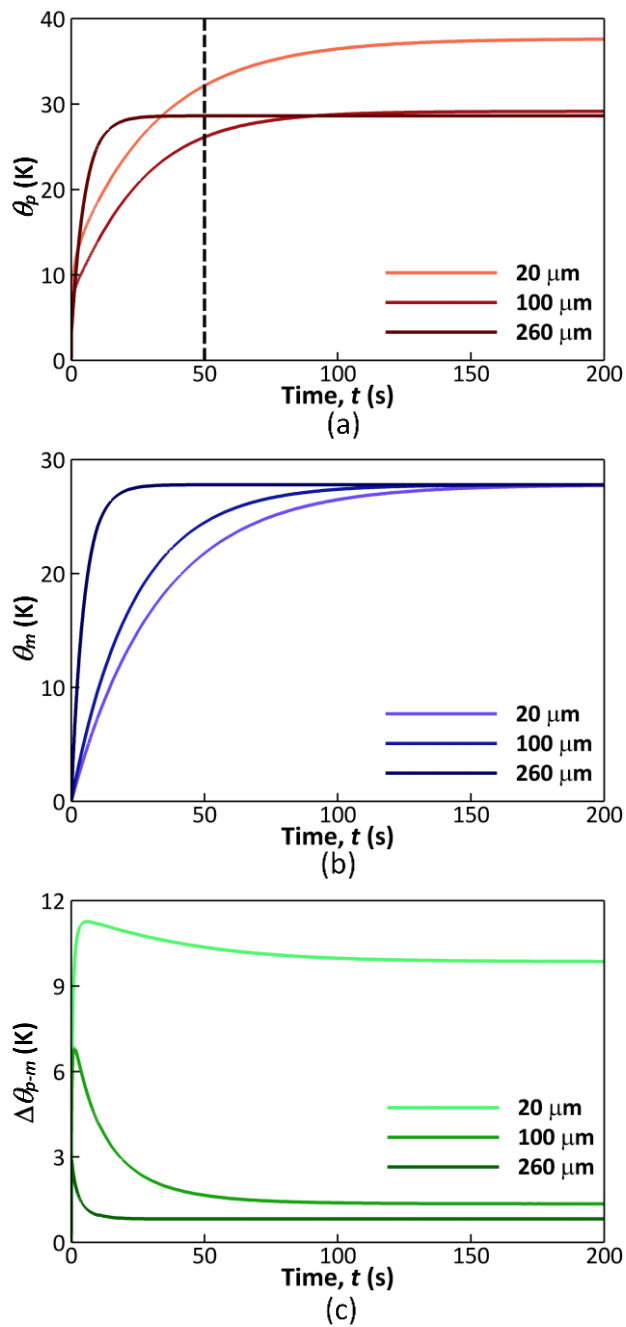


Figure 8.2. Simulated transient response of a vapor chamber for multiple values of vapor-core thickness, showing the temporal variation of the (a) peak temperature θ_p , (b) volume-averaged mean temperature θ_m , and (c) difference between the peak and mean temperatures $\Delta\theta_{p-m} = \theta_p - \theta_m$.

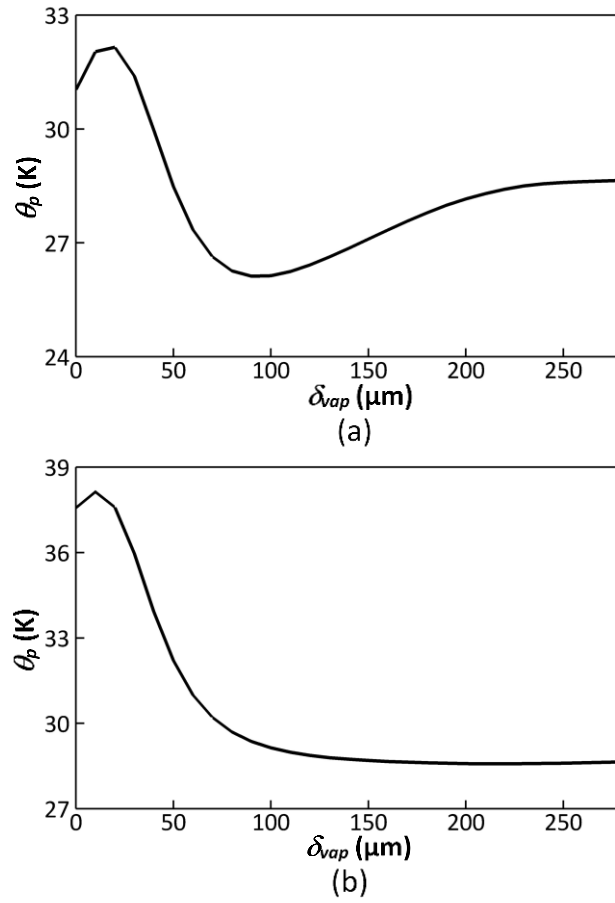


Figure 8.3. Simulated vapor chamber peak temperature θ_p as a function of vapor core thickness δ_{vap} (a) at $t = 50$ s and (b) at steady state ($t = 200$ s).

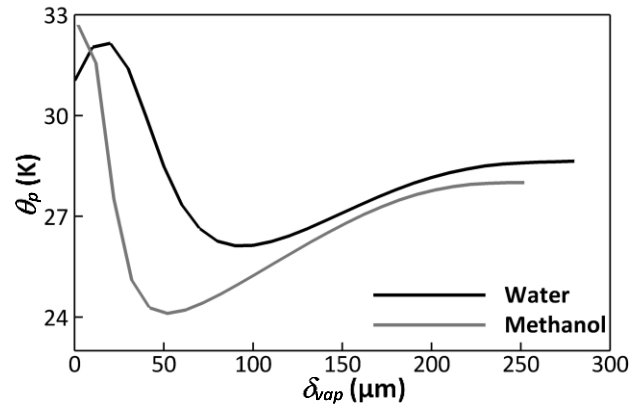


Figure 8.4. Selection of the working fluid between water and methanol using the simulated vapor chamber peak temperature θ_p as a function of vapor core thickness δ_{vap} (a) at $t = 50$ s and (b) at steady state ($t = 200$ s).

9. SUMMARY AND OUTLOOK

This study has built a strong foundation for the utilization of the vapor chamber technology for applications with extreme space constraints and transient heat generation, such as thermal management of mobile electronic devices. The time-stepping analytical model for vapor chambers developed in this study achieved a low computational cost without significant loss of accuracy or generality of boundary conditions. The model enabled understanding the key mechanisms governing the transient thermal behavior of vapor chambers, which was utilized for developing design practices under both steady-state and transient conditions. Additionally, the experimental technique developed in this work can characterize vapor chambers for the application of mobile thermal management.

There are two potential next steps from this study.

1. Transient heat loads are present in many electronic applications, where vapor chambers can provide effective heat spreading. The practices developed for the design of vapor chambers under transient conditions can be expanded to other applications, with different space constraints, power levels and time scales than those of considered in this study.
2. Development of specific designs for vapor chambers and conducting their fabrication and experimental characterization to demonstrate feasibility for thermal management under extreme space constraints and transient heat loads. The design practices and modeling capabilities developed in this study can be utilized for the developing and preliminary testing of new vapor chamber designs, before its fabrication and experimental characterization.

REFERENCES

- [1] R. Hopkins, A. Faghri, and D. Khrustalev, "Flat Miniature Heat Pipes with Micro Capillary Grooves," *Journal of Heat Transfer*, vol. 121, no. 1, pp. 102–109, 1999.
- [2] A. R. Moritz and F. C. Henriques Jr, "Studies of Thermal Injury: II. The Relative Importance of Time and Surface Temperature in the Causation of Cutaneous Burns," *The American Journal of Pathology*, vol. 23, no. 5, p. 695, 1947.
- [3] M. K. Berhe, "Ergonomic Temperature Limits for Handheld Electronic Devices," in *ASME 2007 InterPACK Conference*, Vancouver, British Columbia, Canada, vol. 2, pp. 1041–1047, 2007.
- [4] J. A. Weibel and S. V. Garimella, "Recent Advances in Vapor Chamber Transport Characterization for High-Heat-Flux Applications," in *Advances in Heat Transfer*, vol. 45, pp. 209–301, 2013.
- [5] Y. Yadavalli, J. A. Weibel, and S. V. Garimella, "Performance-Governing Transport Mechanisms for Heat Pipes at Ultrathin Form Factors," *IEEE Transactions on Components, Packaging and Manufacturing Technology*, vol. 5, no. 11, pp. 1618–1627, 2015.
- [6] P. D. Dunn and D. A. Reay, "The Heat Pipe," *Physics in Technology*, vol. 4, no. 3, p. 187, 1973.
- [7] C. Wang, Z. Liu, G. Zhang, and M. Zhang, "Experimental Investigations of Flat Plate Heat Pipes with Interlaced Narrow Grooves or Channels as Capillary Structure," *Experimental Thermal and Fluid Science*, vol. 48, pp. 222–229, 2013.
- [8] S.-C. Wong, K.-C. Hsieh, J.-D. Wu, and W.-L. Han, "A Novel Vapor Chamber and its Performance," *International Journal of Heat and Mass Transfer*, vol. 53, no. 11–12, pp. 2377–2384, 2010.
- [9] Y. Xuan, Y. Hong, and Q. Li, "Investigation on Transient Behaviors of Flat Plate Heat Pipes," *Experimental Thermal and Fluid Science*, vol. 28, no. 2–3, pp. 249–255, 2004.
- [10] Y.-T. Chen, S.-W. Kang, Y.-H. Hung, C.-H. Huang, and K.-C. Chien, "Feasibility Study of an Aluminum Vapor Chamber with Radial Grooved and Sintered Powders Wick Structures," *Applied Thermal Engineering*, vol. 51, no. 1–2, pp. 864–870, 2013.
- [11] M. Mochizuki, Y. Saito, F. Kiyooka, T. Nguyen, T. Nguyen, and V. Wuttijumnong, "Advanced Micro-Channel Vapor Chamber for Cooling High Power Processors," in *ASME 2007 InterPACK Conference collocated with the ASME/JSME 2007 Thermal Engineering Heat Transfer Summer Conference*, Vancouver, British Columbia, Canada, vol. 1, pp. 695–702, 2007.

- [12] G. S. Hwang, Y. Nam, E. Fleming, P. Dussinger, Y. S. Ju, and M. Kaviany, "Multi-Artery Heat Pipe Spreader: Experiment," *International Journal of Heat and Mass Transfer*, vol. 53, no. 13–14, pp. 2662–2669, 2010.
- [13] Y. Koito, H. Imura, M. Mochizuki, Y. Saito, and S. Torii, "Numerical Analysis and Experimental Verification on Thermal Fluid Phenomena in a Vapor Chamber," *Applied Thermal Engineering*, vol. 26, no. 14–15, pp. 1669–1676, 2006.
- [14] Q. Cai and Y.-C. Chen, "Investigations of Biporous Wick Structure Dryout," *Journal of Heat Transfer*, vol. 134, no. 2, pp. 021503–021503, 2011.
- [15] J. A. Weibel and S. V. Garimella, "Visualization of Vapor Formation Regimes during Capillary-Fed Boiling in Sintered-Powder Heat Pipe Wicks," *International Journal of Heat and Mass Transfer*, vol. 55, no. 13–14, pp. 3498–3510, 2012.
- [16] T. Semenic and I. Catton, "Experimental Study of Biporous Wicks for High Heat Flux Applications," *International Journal of Heat and Mass Transfer*, vol. 52, no. 21–22, pp. 5113–5121, 2009.
- [17] R. Ranjan, S. V. Garimella, J. Y. Murthy, and K. Yazawa, "Assessment of Nanostructured Capillary Wicks for Passive Two-Phase Heat Transport," *Nanoscale and Microscale Thermophysical Engineering*, vol. 15, no. 3, pp. 179–194, 2011.
- [18] J. A. Weibel, S. V. Garimella, J. Y. Murthy, and D. H. Altman, "Design of Integrated Nanostructured Wicks for High-Performance Vapor Chambers," *IEEE Transactions on Components, Packaging and Manufacturing Technology*, vol. 1, no. 6, pp. 859–867, 2011.
- [19] Y. S. Ju, M. Kaviany, Y. Nam, S. Sharratt, G. S. Hwang, I. Catton, E. Fleming, and P. Dussinger, "Planar Vapor Chamber with Hybrid Evaporator Wicks for the Thermal Management of High-Heat-Flux and High-Power Optoelectronic Devices," *International Journal of Heat and Mass Transfer*, vol. 60, pp. 163–169, 2013.
- [20] H. Aoki, N. Shioya, M. Ikeda, and Y. Kimura, "Development of Ultra Thin Plate-Type Heat Pipe with Less than 1 mm Thickness," in *26th Annual IEEE Semiconductor Thermal Measurement and Management Symposium*, Santa Clara, CA USA, pp. 217–222, 2010.
- [21] C. Ding, G. Soni, P. Bozorgi, B. D. Piorek, C. D. Meinhart, and N. C. MacDonald, "A Flat Heat Pipe Architecture Based on Nanostructured Titania," *Journal of Microelectromechanical Systems*, vol. 19, no. 4, pp. 878–884, 2010.
- [22] C. Oshman, B. Shi, C. Li, R. Yang, Y. C. Lee, G. P. Peterson, and V. M. Bright, "The Development of Polymer-Based Flat Heat Pipes," *Journal of Microelectromechanical Systems*, vol. 20, no. 2, pp. 410–417, 2011.
- [23] R. Lewis, S. Xu, L. Liew, C. Coolidge, R. Yang, and Y. Lee, "Thin Flexible Thermal Ground Planes: Fabrication and Scaling Characterization," *Journal of Microelectromechanical Systems*, vol. 24, no. 6, pp. 2040–2048, 2015.

- [24] U. Vadakkan, S. V. Garimella, and J. Y. Murthy, "Transport in Flat Heat Pipes at High Heat Fluxes from Multiple Discrete Sources," *Journal of Heat Transfer*, vol. 126, no. 3, pp. 347–354, 2004.
- [25] R. Ranjan, J. Y. Murthy, S. V. Garimella, and U. Vadakkan, "A Numerical Model for Transport in Flat Heat Pipes Considering Wick Microstructure Effects," *International Journal of Heat and Mass Transfer*, vol. 54, no. 1–3, pp. 153–168, 2010.
- [26] R. Ranjan, J. Y. Murthy, S. V. Garimella, D. H. Altman, and M. T. North, "Modeling and Design Optimization of Ultrathin Vapor Chambers for High Heat Flux Applications," *IEEE Transactions on Components, Packaging and Manufacturing Technology*, vol. 2, no. 9, pp. 1465–1479, 2012.
- [27] M. Famouri, M. M. Abdollahzadeh, A. Abdulshaheed, G. Huang, G. Carbajal, and C. Li, "Transient Analysis of a Cylindrical Heat Pipe Considering Different Wick Structures," in *ASME 2016 Heat Transfer Summer Conference*, p. V002T08A023, 2016.
- [28] S. Harmand, R. Sonan, M. Fakès, and H. Hassan, "Transient Cooling of Electronic Components by Flat Heat Pipes," *Applied Thermal Engineering*, vol. 31, no. 11–12, pp. 1877–1885, 2011.
- [29] R. S. Prasher, "A Simplified Conduction Based Modeling Scheme for Design Sensitivity Study of Thermal Solution Utilizing Heat Pipe and Vapor Chamber Technology," *Journal of Electronic Packaging*, vol. 125, no. 3, pp. 378–385, 2003.
- [30] M. Aghvami and A. Faghri, "Analysis of Flat Heat Pipes with Various Heating and Cooling Configurations," *Applied Thermal Engineering*, vol. 31, no. 14–15, pp. 2645–2655, 2011.
- [31] F. Lefèvre and M. Lallemand, "Coupled Thermal and Hydrodynamic Models of Flat Micro Heat Pipes for the Cooling of Multiple Electronic Components," *International Journal of Heat and Mass Transfer*, vol. 49, no. 7–8, pp. 1375–1383, 2006.
- [32] N. Zhu and K. Vafai, "Analytical Modeling of the Startup Characteristics of Asymmetrical Flat-Plate and Disk-Shaped Heat Pipes," *International Journal of Heat and Mass Transfer*, vol. 41, no. 17, pp. 2619–2637, 1998.
- [33] M. S. El-Genk and H. Lianmin, "An Experimental Investigation of the Transient Response of a Water Heat Pipe," *International Journal of Heat and Mass Transfer*, vol. 36, no. 15, pp. 3823–3830, 1993.
- [34] J.-M. Tournier and M. S. El-Genk, "A Heat Pipe Transient Analysis Model," *International Journal of Heat and Mass Transfer*, vol. 37, no. 5, pp. 753–762, 1994.
- [35] S. Murer, P. Lybaert, L. Gleton, and A. Sturbois, "Experimental and Numerical Analysis of the Transient Response of a Miniature Heat Pipe," *Applied Thermal Engineering*, vol. 25, no. 16, pp. 2566–2577, 2005.

- [36] R. Sonan, S. Harmand, J. Pellé, D. Leger, and M. Fakès, “Transient Thermal and Hydrodynamic Model of Flat Heat Pipe for the Cooling of Electronics Components,” *International Journal of Heat and Mass Transfer*, vol. 51, no. 25–26, pp. 6006–6017, 2008.
- [37] G. Patankar, S. Mancin, J. A. Weibel, S. V. Garimella, and M. A. MacDonald, “A Method for Thermal Performance Characterization of Ultra-Thin Vapor Chambers Cooled by Natural Convection,” in *ASME 2015 International Technical Conference and Exhibition on Packaging and Integration of Electronic and Photonic Microsystems*, San Francisco, California, USA., vol. 3, p. V003T04A018, 2015.
- [38] G. Patankar, S. Mancin, J. A. Weibel, S. V. Garimella, and M. A. MacDonald, “A Method for Thermal Performance Characterization of Ultrathin Vapor Chambers Cooled by Natural Convection,” *Journal of Electronic Packaging*, vol. 138, no. 1, p. 010903, 2016.
- [39] NASA JPL, “NASA Master Paints,” NASA Jet Propulsion Laboratory, California Institute of Technology, Pasadena, CA, <http://masterweb.jpl.nasa.gov/reference/paints.htm>, 2012.
- [40] Fluent, “ANSYS FLUENT 14.0 User’s Guide.” ANSYS Fluent, Canonsburg, PA, 2011.
- [41] G. Patankar, J. A. Weibel, and S. V. Garimella, “Patterning the Condenser-Side Wick in Ultra-Thin Vapor Chamber Heat Spreaders to Improve Skin Temperature Uniformity of Mobile Devices,” *International Journal of Heat and Mass Transfer*, vol. 101, pp. 927–936, 2016.
- [42] “R. Ranjan, J. Y. Murthy, S. V. Garimella, D. H. Altman, and M. T. North, ‘Modeling and Design Optimization of Ultra-Thin Vapor Chambers for High Heat Flux Applications,’ *IEEE Transactions on Components, Packaging and Manufacturing Technology*, Vol 2, No. 9, Pp. 1465-1479, 2012.”
- [43] R. W. Schrage, “A Theoretical Study of Interphase Mass Transfer,” Columbia University Press, New York, 1953.
- [44] R. Marek and J. Straub, “Analysis of the Evaporation Coefficient and the Condensation Coefficient of Water,” *International Journal of Heat and Mass Transfer*, vol. 44, no. 1, pp. 39–53, 2001.
- [45] G. Patankar, S. Mancin, J. A. Weibel, S. V. Garimella, and M. A. MacDonald, “A Method for Thermal Performance Characterization of Ultra-Thin Vapor Chambers Cooled by Natural Convection,” *Journal of Electronic Packaging*, in press.
- [46] G. Patankar, J. A. Weibel, and S. V. Garimella, “Working-Fluid Selection for Minimized Thermal Resistance in Ultra-Thin Vapor Chambers,” *International Journal of Heat and Mass Transfer*, vol. 106, pp. 648–654, 2017.
- [47] B. Xiao and A. Faghri, “A Three-Dimensional Thermal-Fluid Analysis of Flat Heat Pipes,” *International Journal of Heat and Mass Transfer*, vol. 51, no. 11–12, pp. 3113–3126, 2008.

- [48] E. W. Lemmon, M. L. Huber, and M. O. McLinden, *NIST Standard Reference Database 23: Reference Fluid Thermodynamic and Transport Properties-REFPROP*. Gaithersburg: National Institute of Standards and Technology, Standard Reference Data Program, 2013.
- [49] *MATLAB Release 2017a*. Natick, Massachusetts, United States: The MathWorks, Inc.
- [50] G. Patankar, J. A. Weibel, and S. V. Garimella, “A Validated Time-Stepping Analytical Model for 3D Transient Vapor Chamber Transport,” *International Journal of Heat and Mass Transfer*, vol. 119, pp. 867–879, 2018.
- [51] G. Patankar, J. A. Weibel, and S. V. Garimella, “A Time-Stepping Analytical Model for 3D Transient Vapor Chamber Transport,” in *Sixteenth Intersociety Conference on Thermal and Thermomechanical Phenomena in Electronic Systems*, Orlando, Florida, USA, 2017.
- [52] V. P. Carey, *Liquid-Vapor Phase-Change Phenomena*. Washington (D.C.), USA: Hemisphere Pub. Corp, 1992.
- [53] R. Ranjan, J. Y. Murthy, S. V. Garimella, D. H. Altman, and M. T. North, “Modeling and Design Optimization of Ultrathin Vapor Chambers for High Heat Flux Applications,” 2012.
- [54] G. Patankar, J. A. Weibel, and S. V. Garimella, “On the Transient Thermal Response of Thin Vapor Chamber Heat Spreaders: Governing Mechanisms and Performance Relative to Metal Spreaders,” *In Review*.
- [55] F. P. Incropera, D. P. Dewitt, T. L. Bergman, and A. S. Lavine, *Fundamentals of Heat and Mass Transfer*. Hoboken, NJ, USA: John Wiley & Sons, 2007.
- [56] Y. Yadavalli, J. A. Weibel, and S. V. Garimella, “Performance-Governing Transport Mechanisms for Heat Pipes at Ultrathin Form Factors,” *IEEE Transactions on Components, Packaging and Manufacturing Technology*, vol. 5, no. 11, pp. 1618–1627, 2015.
- [57] G. Patankar, J. A. Weibel, and S. V. Garimella, “On the Transient Thermal Response of Thin Vapor Chamber Heat Spreaders: Optimized Design and Fluid Selection,” *In Review*.
- [58] J. T. Jayne, S. X. Duan, P. Davidovits, D. R. Worsnop, M. S. Zahniser, and C. E. Kolb, “Uptake of Gas-Phase Alcohol and Organic Acid Molecules by Water Surfaces,” *The Journal of Physical Chemistry*, vol. 95, no. 16, pp. 6329–6336, 1991.
- [59] A. Faghri, *Heat Pipe Science and Technology*. Washington DC: Taylor & Francis, 1995.

APPENDIX A. EFFECTIVE PERMEABILITY FORMULATION

In the condenser-side wick, liquid flows radially outward. The biporous wick design has alternating grooves and sintered copper strips in the azimuthal direction. Liquid flows in parallel through these regions. The governing momentum equations for fluid flow through porous media are shown in equations (A.1-A.3). The last two terms on the right hand side represent additional viscous and inertial pressure drop due to the porous medium. The liquid velocities are sufficient low in the current study such that the inertial pressure drop is negligible and the additional viscous pressure drop is given by

$$\frac{dP}{dx} = \frac{\mu}{K_1} u_1 = \frac{\mu}{K_2} u_2 \quad (\text{A.1})$$

where 1 and 2 refer to the permeability of sintered copper powder strips and rectangular grooves, respectively. The permeabilities are computed using empirical correlations found in Ref. [59]. An effective liquid velocity can be defined as follows.

$$u_1 A_1 + u_2 A_2 = u_{eff} (A_1 + A_2) \quad (\text{A.2})$$

Combining equations (A.1) and (A.2) yields the following relation,

$$\begin{aligned} \frac{dP}{dx} &= \frac{\mu}{K_1 A_1 + K_2 A_2} u_{eff} (A_1 + A_2) = \frac{\mu}{K_{eff}} u_{eff} \\ K_{eff} &= \frac{K_1 A_1 + K_2 A_2}{A_1 + A_2} \end{aligned} \quad (\text{A.3})$$

which defines the effective permeability of the wick as the area-weighted average of the individual permeabilities. Note that the areas are normal to the radially outward flow direction. The validity of this effective permeability formulation was confirmed by simulating (FLUENT [40]) flow through a representative periodic unit cell geometry containing one sintered powder strip and one adjacent groove, with a pressure drop imposed across the radial ends of the geometry. An effective permeability was computed based on the pressure drop, total flow rate, and viscosity of the fluid. This computed permeability was compared to the area-weighted average of the individual permeabilities (Equation (A.3)). The error in the area-averaged effective permeability was less than 5%.

APPENDIX B. ESTIMATING THE ACCURACY OF THE TIME-STEPPING ANALYTICAL MODEL

Development of the time-stepping analytical model required multiple simplifications to the governing equations; these simplifications are summarized in Chapter 6 in Eqs. (6.14)-(6.21), (6.31)-(6.32), and (6.38)-(6.39). The accuracy of the model depends on the validity of the assumptions underlying each simplification. This section estimates the errors in the temperature and pressure fields computed by the time-stepping analytical model as a result of the simplifying assumptions for a range of vapor chamber thicknesses and heat input powers. The time-stepping analytical model is solved using the commercial software MATLAB [49]; the temperature-dependent properties of the water vapor are obtained using the commercial software REFPROP [48]. Each infinite-series summation is truncated to 40 terms.

The case details used to estimate the model errors are illustrated in Figure B.1. The vapor chamber has copper walls with a uniform layer of sintered copper wick on the inner surface of the walls. The length and width of the vapor chamber are $L_x = 90$ mm and $L_y = 55$ mm, respectively. The thickness of the walls are $h_{wall,1} = h_{wall,2} = 0.2$ mm. Three values of the working thickness ($h_{wick,1} + h_{wick,2} + h_{vap}$) were simulated, namely 0.1 mm, 0.3 mm, and 0.6 mm. Water is used as the working fluid. The properties of the working fluid, copper, and porous wick materials are shown in Table 6.2. The vapor chamber is initially at a uniform temperature of 300 K. Starting at $t = 0$ s, the vapor chamber receives a heat input power Q applied over a square area of 1 cm^2 at the center of the evaporator side; the rest of the evaporator-side face is insulated. The opposing condenser side experiences a convective boundary condition with a heat transfer coefficient proportional to the input power, $(30 \text{ W/m}^2\text{K}) \times Q / (4 \text{ W})$, and an ambient temperature of 300 K. A convection coefficient proportional to the power is used so that the steady-state volume-averaged temperature in the vapor core is similar across the simulated cases, thus maintaining similar vapor-phase properties across the cases. The sides of the vapor chamber are insulated.

Simulations were conducted for increasing heat input power at each value of the working thickness. For each combination of working thickness and heat input power, the minimum possible wick thickness was used so that the total pressure drop in the wick plus the vapor core is equal to the capillary pressure of the wick; this approach minimizes the temperature drop across the vapor chamber for any given case, as is discussed in Chapter 4. For each of the working thicknesses,

there is an upper limit of power input above which there is no viable wick thickness (*i.e.*, the wick would need to fill the entire working thickness to avoid a capillary limit). Simulations are performed up to these maximum power inputs of 10 W, 70 W, and 240 W for working thicknesses of 0.1 mm, 0.3 mm, and 0.6 mm, respectively.

The assumptions used for simplifying the governing equations can be stated in the general form of $CN \ll 1$, where CN is termed a condition number that must satisfy the inequality. The condition numbers are calculated for each assumption using the steady-state results of all simulation cases described in the previous paragraph (full range of working thicknesses and powers). The analysis hereafter only considers the assumptions that were found to have the most prominent effects on the temperature and pressure fields. All other assumptions had condition numbers less than 0.01 (unitless) across all the simulated cases, and hence were deemed negligible in comparison. The following three assumptions were found to cause the largest errors in the temperature and pressure fields across the simulated cases: The first is assuming a negligible temperature difference across the thickness of the wall and the wick on the evaporator side (Eq.(6.31)). The condition number for this assumption is

$$CN_T = \frac{\Delta T_{thickness}}{T_{max} - T_{min}}; \Delta T_{thickness} = q_{in}'' \left(\frac{h_{wall,1}}{k_{wall,1}} + \frac{h_{wick,1}}{k_{eff,wick,1}} \right). \quad (B1)$$

This condition number is the ratio of the neglected temperature difference across the wall and the wick on the evaporator side at the maximum temperature difference in the vapor chamber. Thus, the condition number directly indicates the relative error in the temperature,

$$\varepsilon_T = CN_T. \quad (B2)$$

The second assumption is linearizing the Clausius-Clapeyron equation (Eq. (6.38)). The condition number for this assumption is

$$CN_{CC} = \frac{\left(\frac{P_{vap}}{T_{sat}^2} - \frac{P_O}{(T_{sat}^2)_{mean}} \right)_{max}}{\frac{P_O}{(T_{sat}^2)_{mean}}}, \quad (B3)$$

where *max* indicates the maximum value of the quantity within the vapor core. This assumes a linear relation between the vapor pressure and the saturation temperature and will lead to a less

accurate computation of pressure in the vapor core. Upon integrating the original Clausius-Clapeyron equation (6.5),

$$P_{vap,actual} = P_O \exp\left(\frac{h_{fg}}{R} \left(\frac{1}{T_{vap,mean}} - \frac{1}{T_{sat}}\right)\right), \quad (B4)$$

which is the proper non-linear relation between the vapor pressure and the saturation temperature. The relative error in the total pressure drop in the vapor chamber due to the linearization of the Clausius-Clapeyron equation is

$$\varepsilon_{P,CC} = \frac{(P_{vap,actual} - P_{vap})_{max}}{(P_{vap,max} - P_{vap,min}) + (P_{wick,max} - P_{wick,min})} \quad (B5)$$

The third assumption is neglecting convection in the momentum equation in the vapor core (Eq.(6.17)). The condition number for this assumption is

$$CN_{conv} = \max\left(\text{Re}_{x,vap} \frac{h_{vap}^2}{L_x^2}, \text{Re}_{y,vap} \frac{h_{vap}^2}{L_y^2}\right) \quad (B6)$$

The condition number CN_{conv} is the ratio of the scale of convection with diffusion in the z -direction in the momentum equation, and thus is an indicator of error in the pressure drop in the vapor core. The relative error in the total pressure drop in the vapor chamber due to this assumption is

$$\varepsilon_{P,conv} = \frac{CN_{conv} (P_{vap,max} - P_{vap,min})}{(P_{vap,max} - P_{vap,min}) + (P_{wick,max} - P_{wick,min})} \quad (B7)$$

The relative errors in the maximum temperature drop in the vapor chamber are plotted in Figure B.2. This relative error is negligible for the case with 0.1 mm working thickness. The thermal resistance across the wick in this case is relatively small compared to the high thermal resistance imposed by the thin vapor core. The relative error increases with increasing working thickness and power. With increasing working thickness, at a constant power, the wick thickness does not change much and the vapor core gets thicker. Hence the thermal resistance across the wick relative to the thermal resistance imposed by the thicker vapor core increases, and the relative error in the maximum temperature drop increases. At a given working thickness, with increasing power, the required wick thickness increases to maintain the constraint that total pressure drop is equal to the

capillary pressure. Hence the resistance across the wick increases, and so do the relative errors in the maximum temperature drop. At the most extreme working thickness and operating power, the relative error in the maximum temperature drop is only 30%; for most of the simulated cases, the error is under 10%. Thus the model has excellent accuracy in computing the maximum temperature drop in a vapor chamber over a wide range of thicknesses and powers, except in extreme cases where the operating power requires a thick wick structure that occupies most of the available working thickness.

The relative errors in the maximum pressure drop in the vapor chamber due to linearization of the Clausius-Clapeyron equation are plotted in Figure B.3a. Non-negligible relative errors in the total pressure drop in the vapor chamber are observed only at the highest powers for each of the three working thicknesses. This is because the evaporated mass flux is the highest and the vapor core thickness is lowest (due to a need for a thicker wick at higher powers). This leads to much higher vapor velocities and hence pressure variations in the vapor core, leading to a high error in using a linearized Clausius-Clapeyron equation, according to Eq. (B3). The relative errors in the maximum pressure drop in the vapor chamber due to neglecting the convection term in the momentum equation in the vapor core are plotted in Figure B.3b. The relative error in the total pressure drop in the vapor chamber increases with increasing power and working thickness. According to Eq. (B6), the error due to neglecting the convection term should increase with vapor core velocity, and also as the square of vapor core thickness. Increasing the working thickness increases the vapor-core thickness, and thereby also increases the relative error. Increasing the power leads to higher evaporated mass fluxes and hence higher vapor velocities, but simultaneously lower vapor core thickness; this trade-off leads to an increasing error with increase in power for the case with a working thickness of 0.6 mm. The total pressure drop in the vapor chamber is generally predicted with good accuracy (relative error lower than 0.1, except again for the extreme case with 600 μm working thickness and 240 W of heat input).

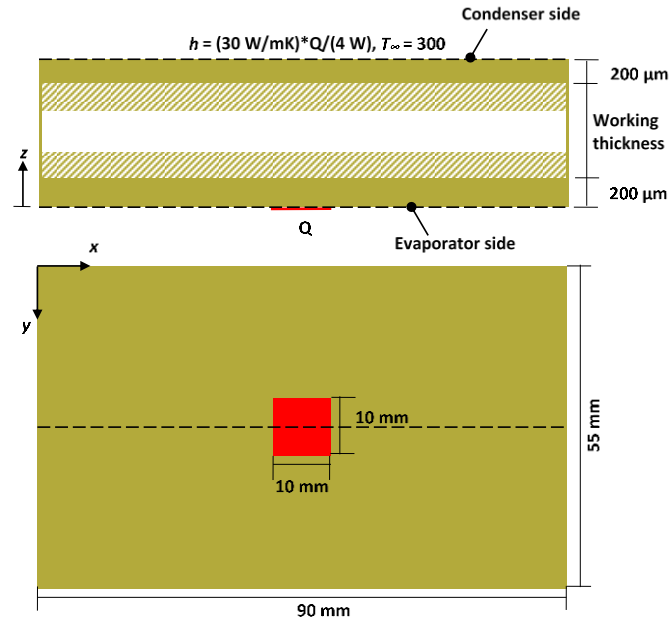


Figure B.1. Schematic diagram of the simulated geometry and boundary conditions used estimate the error in the predictions of the time-stepping analytical vapor chamber model.

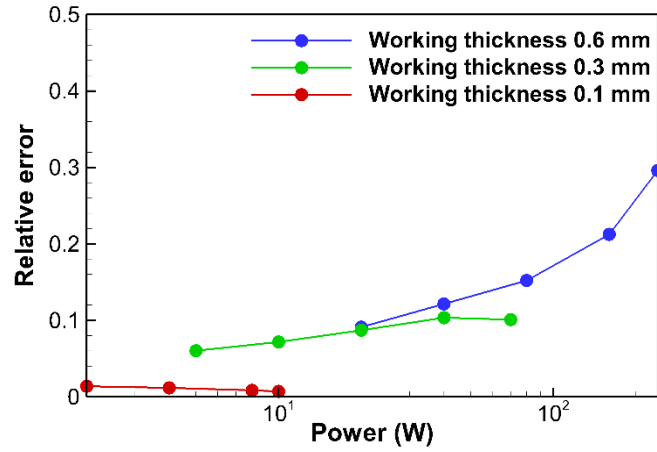
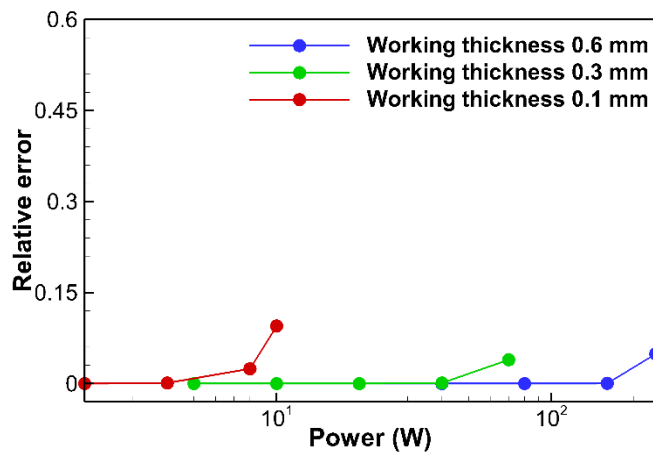
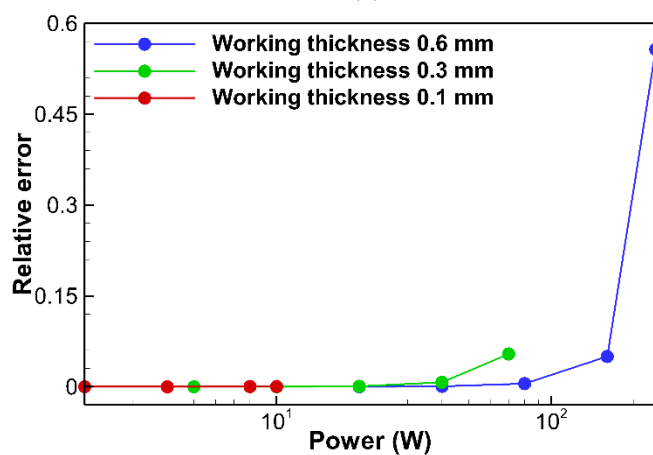


Figure B.2 Estimated relative error in the difference between the maximum and minimum temperature in the vapor chamber due to the assumption of negligible temperature difference across the thickness of the wall and the wick on the evaporator side, as a function of power (plotted on a log scale) over a range of working thicknesses.



(a)



(b)

Figure B.3. Estimated relative error in the total pressure drop in the vapor chamber as a function of power (plotted on a log scale) over a range of working thickness due to (a) linearizing the Clausius-Clapeyron equation, and (b) neglecting the convection term in the momentum equation for the vapor core.

APPENDIX C. BENCHMARKING THE VAPOR CHAMBER PERFORMANCE RELATIVE TO A COPPER SPREADER

The case details for the figures below are the same as described in Section 7.1.1, except for the following:

Case A: the wall thickness is $100\ \mu\text{m}$ on each side.

Case B: the wall and wick thickness is $100\ \mu\text{m}$ on each side, heat input is $100\ \text{W}$, and the heat transfer coefficient at the condenser is $750\ \text{W}/\text{m}^2\text{K}$.

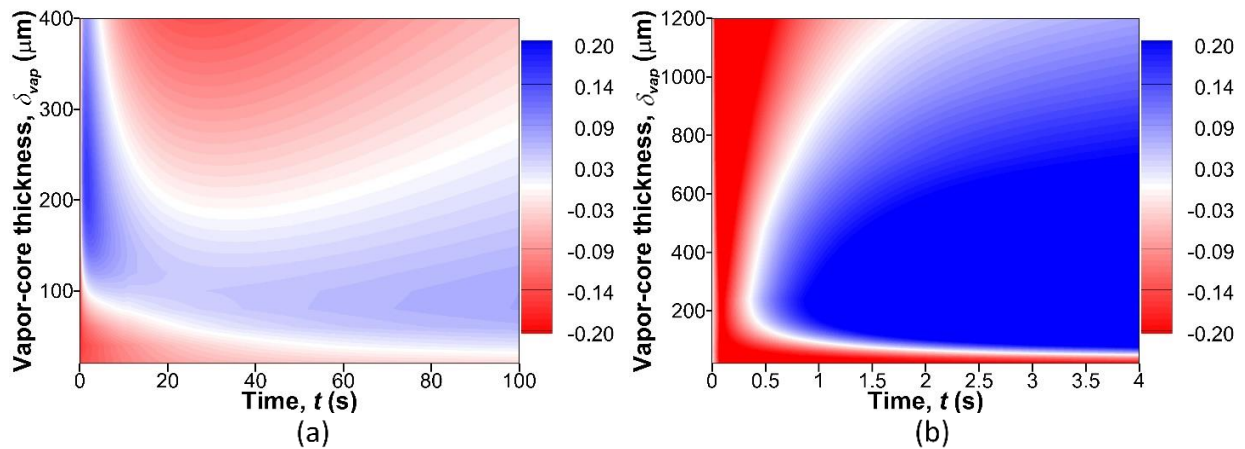


Figure C.1. Contour plot of the metric for the thermal performance of a vapor chamber relative to a copper spreader (M_{VC-Cu}), for a range of vapor core thicknesses, and as a function of time for (a) Case A and (b) Case B.

VITA

Gaurav Patankar was born in Pune, India in 1992. He received his Bachelor of Technology in Mechanical Engineering from Indian Institute of Technology Hyderabad in 2013 and his Ph.D. in Mechanical Engineering at Purdue University, under the advisement of Dr. Suresh V. Garimella and Dr. Justin A. Weibel in May 2019. His research at Purdue included experimental characterization, modeling and design of ultra-thin vapor chambers for mobile electronic device application. He is the recipient of the Outstanding Paper Award for “A method for thermal performance characterization of ultra-thin vapor chambers cooled by natural convection,” by G. Patankar, S. Mancin, J. A. Weibel, M. A. MacDonald, and S. V. Garimella, at the ASME 2015 International Technical Conference and Exhibition on Packaging and Integration of Electronic and Photonic Microsystems.

PUBLICATIONS

G. Patankar, S. Mancin, J. A. Weibel, S. V. Garimella, and M. A. MacDonald, “A Method for Thermal Performance Characterization of Ultra-Thin Vapor Chambers Cooled by Natural Convection,” presented at the *ASME 2015 International Technical Conference and Exhibition on Packaging and Integration of Electronic and Photonic Microsystems*, San Francisco, California, USA., vol. 3, p. V003T04A018, 2015.

G. Patankar, S. Mancin, J. A. Weibel, S. V. Garimella, and M. A. MacDonald, “A Method for Thermal Performance Characterization of Ultrathin Vapor Chambers Cooled by Natural Convection,” *Journal of Electronic Packaging*, vol. 138, no. 1, pp. 010903, 2016.

G. Patankar, J. A. Weibel, and S. V. Garimella, “Patterning the Condenser-Side Wick in Ultra-Thin Vapor Chamber Heat Spreaders to Improve Skin Temperature Uniformity of Mobile Devices,” *International Journal of Heat and Mass Transfer*, vol. 101, pp. 927–936, 2016.

G. Patankar, J. A. Weibel, and S. V. Garimella, “Working-Fluid Selection for Minimized Thermal Resistance in Ultra-Thin Vapor Chambers,” *International Journal of Heat and Mass Transfer*, vol. 106, pp. 648–654, 2017.

G. Patankar, J. A. Weibel, and S. V. Garimella, “A Time-Stepping Analytical Model for 3D Transient Vapor Chamber Transport,” presented at the *Sixteenth Intersociety Conference on Thermal and Thermomechanical Phenomena in Electronic Systems*, Orlando, Florida, USA, 2017.

G. Patankar, J. A. Weibel, and S. V. Garimella, “A Validated Time-Stepping Analytical Model for 3D Transient Vapor Chamber Transport,” *International Journal of Heat and Mass Transfer*, vol. 119, pp. 867–879, 2018.

G. Patankar, J. A. Weibel, and S. V. Garimella, “On the Transient Thermal Response of Thin Vapor Chamber Heat Spreaders: Governing Mechanisms and Performance Relative to Metal Spreaders,” *in review*.

G. Patankar, J. A. Weibel, and S. V. Garimella, “On the Transient Thermal Response of Thin Vapor Chamber Heat Spreaders: Optimized Design and Fluid Selection,” *in review*.